MASSACHUSETTS INSTITUTE OF TECHNOLOGY

The RESEARCH LABORATORY *of* ELECTRONICS

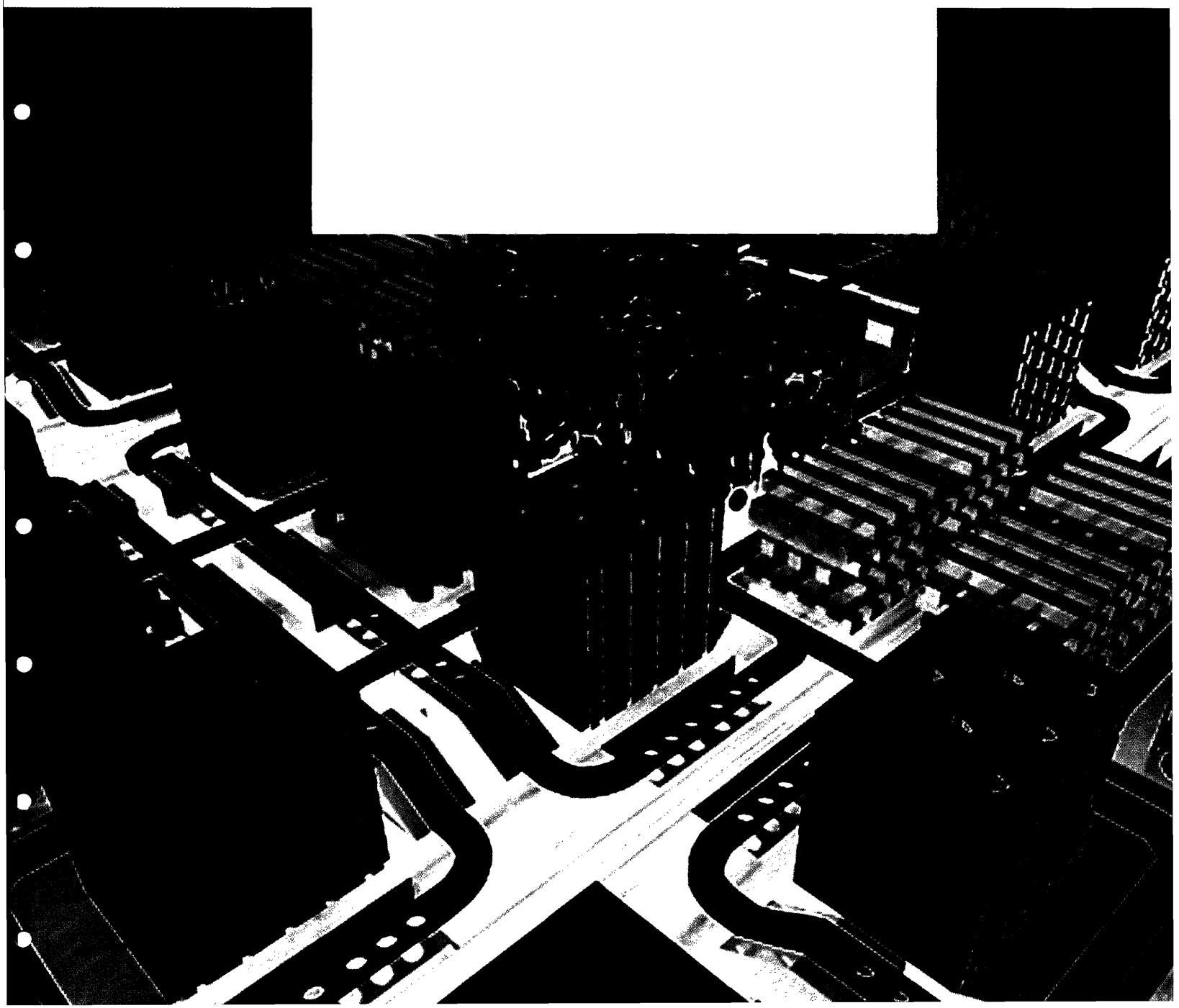

Searches for and Follow-Up Studies of Southern Radio Pulsars

By: Fronefield Crawfird III

RLE Technical Report No. 643

September 2000

Searches for and Follow-Up Studies of Southern Radio Pulsars

By: Fronefield Crawfird III

RLE Technical Report No. 643

September 2000

Searches for and Follow-up Studies of Southern Radio Pulsars

by

Fronefield Crawford III

B.A. Astrophysics, Williams College (1994)

Submitted to the Department of Physics
in partial fulfillment of the requirements for the degree of

Doctor of Philosophy

at the

MASSACHUSETTS INSTITUTE OF TECHNOLOGY

September 2000

Author ..... Fronefield Crawford III .....
Department of Physics
July 6, 2000

Certified by ..... Victoria M. Kaspi .....
Victoria M. Kaspi
Assistant Professor
Thesis Supervisor

Accepted by ..... Thomas J. Greytak .....
Thomas J. Greytak
Professor, Associate Department Head for Education

Searches for and Follow-up Studies of Southern Radio Pulsars

by

Fronefield Crawford III

Submitted to the Department of Physics
on July 6, 2000, in partial fulfillment of the
requirements for the degree of
Doctor of Philosophy

Abstract

The Parkes Multibeam Pulsar Survey (PM Survey) is a new high-frequency survey for radio pulsars in the southern Galactic plane. With about 80% of the survey completed, 569 new pulsars have been discovered, of which 187 have complete timing solutions. A number of interesting pulsars have been discovered, including PSR J1119−6127, a young radio pulsar with a very large magnetic field.

We report the results of a companion survey for radio pulsars in the Small Magellanic Cloud (SMC). Two new pulsars have been discovered in this survey, one of which is located within the SMC. The number of pulsars found is consistent with the expected number derived using several methods. The age distribution of luminous Magellanic Cloud pulsars supports the conjecture that pulsars younger than about 5 Myr are preferentially more luminous than older pulsars.

Thirty-nine pulsars discovered in the PM Survey were timed. We have estimated physical parameters for these pulsars, and these parameters will be used in a larger population synthesis modeling effort when the PM Survey is completed. The timing results reveal interesting properties for several pulsars in the sample. Using pulsar-gated radio imaging, we have established accurate positions for several young pulsars from the PM Survey, which in some cases were required to obtain timing solutions.

We have discovered a previously unknown shell radio supernova remnant (SNR), G292.2−0.5, coincident with the young pulsar PSR J1119−6127. The shell morphology, size, and spectral index are all consistent with other young shell SNRs and indicate that G292.2−0.5 is associated with PSR J1119−6127. We have set upper limits on the surface brightness of a pulsar wind nebula (PWN) powered by PSR J1119−6127. These limits are consistent with a model prediction of the surface brightness of a PWN around a young high-magnetic-field pulsar. These results suggest a possible explanation for the lack of central activity in many young shell SNRs.

Thesis Supervisor: Victoria M. Kaspi
Title: Assistant Professor

Acknowledgements

I would first like to thank my advisor, Vicky Kaspi. Three years after I arrived at MIT, she was willing to take me on as a student and give me the opportunity to get involved in the exciting world of pulsar research. I owe her a debt of gratitude for allowing me to work on such an interesting and exciting subject. Vicky has also provided guidance whenever I needed it, and she has encouraged me to become a better scientist through her example. She has also always provided the necessary resources for research travel, and this has given me some wonderful opportunities to use world-class telescope facilities. I feel fortunate to have had so many good opportunities as a graduate student.

I would also like to thank the other members of my thesis committee, Jackie Hewitt and Paul Joss, for their valuable comments on my thesis.

I am pleased to have had the chance to work closely with Dick Manchester, and I have benefited greatly from his insight. Dick and Andrew Lyne allowed me to participate in the PM Survey, which, in my opinion, is the most exciting astronomy research project in the world right now. The chance to work with two of the most distinguished pulsar researchers in the world has been a valuable experience.

Bryan Gaensler has been particularly helpful in assisting me with a number of research problems. He has always been extremely patient with my questions regarding interferometry and has helped me with some of the more difficult aspects of radio imaging. His optimism and good spirits always serve as an example to others.

I must also thank a number of people who have been good friends and colleagues during my time at MIT.

Mike Pivovaroff and Pete Csatorday entered graduate school at the same time I did, and over the course of six years they have remained good friends of mine. We've had our share of good times both in and out of school.

The fellow graduate students on the sixth floor of the CSR also deserve thanks. Derek Fox in particular has been a source of inexhaustible knowledge about all things computer-related and has been a good friend as well. Jon Miller, Dave Pooley, Patrick Wojdowski, and Bob Guerriero also have been welcome friends in the lab.

I benefited from the knowledge and friendship of a number of people in the radio group at MIT. Ian Avruch was and still is a good friend and a never-ending source of humor. Charlie Katz's direct approach and extensive knowledge were always appreciated. Andre Fletcher has always been helpful and has never shied away from lending a hand if needed. Josh Winn and Aaron Cohen were also helpful and fun to hang out with. Bernie Burke deserves thanks for providing me with funding for my first three years at MIT.

My family has always been supportive of my endeavors. I particularly wish to thank my mothers and my fathers for their support, valuable insights, and advice on all kinds of things.

Finally, and most importantly, I thank my wife Jill. She has been the one most affected by the sacrifices I have had to make in order to complete this thesis. My long trips to Australia and long hours at work left her alone and at times without a

husband. She was usually the one who had to deal with me when things were not going as I intended. In a sense, the journey through graduate school can be characterized as a spiritual one, and she has been there for the epiphanies, the apostasies, and everything in between. Through it all she has stayed loyal, understanding, and patient, and has constantly provided me with the proper perspective on all things. This thesis is dedicated to her.

Contents

1 Introduction **15**

1.1 Discovery of Pulsars and Identification as Neutron Stars 15

1.2 The Origin of Neutron Stars 16

1.3 Pulsar Properties 17

1.3.1 Mass, Radius, and Density 17

1.3.2 Gravitational Field 18

1.3.3 Spin and Angular Momentum 18

1.3.4 Magnetic Field 18

1.3.5 Internal Properties 20

1.3.6 The Induced External Electric Field 20

1.3.7 Magnetospheric Radiation 21

1.3.8 Magnetic Dipole Braking 22

1.3.9 Characteristic Age 23

1.3.10 Surface Magnetic Field Strength and Spin-Down Luminosity . 24

1.4 Scientific Motivation for Pulsar Surveys and Follow-up Studies 24

1.5 Thesis Outline 28

2 The Parkes Multibeam Pulsar Survey **31**

2.1 Introduction 31

2.2 Searching for Pulsars 32

2.2.1 General Search Technique 32

2.2.2 Interstellar Propagation Effects 32

2.3 Survey Motivation 35

2.3.1 High Radio Observing Frequency 35
2.3.2 The Multibeam Receiver 36
2.4 Comparison with Previous High-Frequency Pulsar Surveys 39
2.5 Survey Description 39
2.5.1 The Parkes 64-m Telescope 39
2.5.2 Data Acquisition 41
2.5.3 Interference Rejection 42
2.5.4 Data Processing and Analysis 42
2.5.5 Survey Area 43
2.6 Sensitivity Calibration 44
2.6.1 Background 44
2.6.2 Calculation of Survey Sensitivity 45
2.6.3 Check of Survey Sensitivity Calculation 54
2.7 Results to Date 56
2.7.1 New Pulsar Discoveries 56
2.7.2 Young Pulsars 57
2.7.3 PSR J1119−6127: a Young High-Magnetic-Field Pulsar 57

3 Pulsars in the Magellanic Clouds **65**
3.1 Introduction 66
3.2 Previous Magellanic Cloud Pulsar Survey Work 67
3.3 Observations and Data Reduction 68
3.3.1 Survey Observations and Data Reduction 68
3.3.2 Timing Observations and Data Reduction 70
3.4 Results 72
3.4.1 PSR J0045−7319 74
3.4.2 PSR J0057−7201 74
3.4.3 PSR J0113−7220 78
3.4.4 PSR J0535−6935 78
3.4.5 PSR J0537−6910 80

3.4.6 PSR J0540−6919 80
3.4.7 PSR J0455−6951, PSR J0502−6617, and PSR J0529−6652 . . 80
3.5 Discussion 82
3.5.1 Expected Number of Detectable Pulsars in the Magellanic Clouds 82
3.5.2 The Magellanic Cloud Pulsar Luminosity Distribution on the P-$\dot{P}$ Diagram 86
3.5.3 Tests of Pulsar Luminosity Laws 87
3.5.4 OB Associations and Supernova Remnants in the SMC 90
3.5.5 Distribution of Dispersion Measures 91
3.6 Conclusions 93

4 Timing of New PM Survey Pulsars **97**
4.1 Introduction 97
4.2 Timing Procedure 98
4.3 Observations 100
4.4 Results and Discussion 101
4.4.1 PSRs J1301−6305 and J1420−6048: Two Young Pulsars with Timing Noise 107
4.4.2 PSR J1420−6048: A Gamma-ray Pulsar? 107
4.4.3 PSR J1307−6318: A Pulsar with a 4.9 s Period 108
4.4.4 PSR J1413−6141: A Glitching Pulsar 111

5 Pulsar-Gated Radio Imaging of Young PM Survey Pulsars **113**
5.1 Introduction 113
5.1.1 Motivation for Pulsar-Gated Imaging 113
5.1.2 Radio Interferometry 114
5.1.3 The Australia Telescope Compact Array 115
5.1.4 Pulsar Gating 117
5.2 Observations and Data Reduction 117
5.3 Position and Flux Density Results 120

6 G292.2−0.5: A New SNR Associated with PSR J1119−6127 125

6.1 Introduction 125

6.2 Observations 128

6.3 Data Reduction and Results 130

6.3.1 Total Intensity Maps 130

6.3.2 Spatial Filtering and Tomography 131

6.3.3 Shell Polarimetry 134

6.3.4 Search for a Radio PWN in Off-pulse Maps 136

6.4 G292.2−0.5: a New Shell Supernova Remnant 137

6.4.1 Shell Spectral Index 137

6.4.2 Infrared Emission 139

6.5 Evidence for Association with PSR J1119−6127 142

6.5.1 Shell Morphology and Pulsar Location 142

6.5.2 Shell Size and Inferred Expansion Velocity 142

6.5.3 Summary 144

6.6 Implications of the Absence of an Observable PWN 144

6.6.1 The Crab Paradigm 144

6.6.2 Observed Upper Limits and Known Radio PWNe 145

6.6.3 An Evolutionary Model of PWNe 146

6.6.4 Model Prediction for PSR J1119−6127 149

6.6.5 Comparison with Observations 151

6.7 Conclusions 151

A A Search for Sub-millisecond Pulsations from Unidentified FIRST and NVSS Radio Sources 155

A.1 Introduction 155

A.2 Target Choice and Observations 157

A.3 Data Reduction 161

A.4 Discussion 163

A.4.1 Source Brightness 163

A.4.2 Dispersion Smearing and Scattering 164
A.4.3 Wide Beaming 164
A.4.4 Scintillation 164
A.4.5 Binary Orbital Motion 166
A.4.6 Likelihood of Serendipitous Detection 167
A.5 Conclusions 167

B Polarization Properties of Nine Southern Radio Pulsars 169
B.1 Introduction 170
B.2 Observations and Data Reduction 173
B.3 Results and Discussion 173
B.3.1 PSR J0045−7319 178
B.3.2 PSR J1105−6107 178
B.3.3 PSR J1316−6232 179
B.3.4 PSR J1341−6220 180
B.3.5 PSR J1513−5908 180
B.3.6 PSR J1627−4845 182
B.3.7 PSR J1646−4346 182
B.3.8 PSR J1730−3350 182
B.3.9 PSR J1801−2306 183
B.3.10 Linear Polarization vs. Spin-down Luminosity 184
B.4 Conclusions 186

List of Figures

1-1 P-$\dot{P}$ diagram for the radio pulsar population. 19

2-1 A picture of the multibeam receiver. 37

2-2 Sky positions of beams from four interleaved multibeam pointings. . . 38

2-3 A schematic diagram of the Parkes 64-m telescope. 41

2-4 PM Survey sensitivity curves. 55

2-5 P-$\dot{P}$ diagram for new PM Survey pulsars with complete timing solutions. 58

2-6 Radio pulse profile for PSR J1119−6127. 59

3-1 Multibeam survey coverage of the SMC. 69

3-2 Sensitivity to SMC pulsars for our survey and a previous survey. . . . 71

3-3 Radio pulse profiles for three newly discovered pulsars. 73

3-4 Histogram of DM $\sin|b|$ for Galactic and Magellanic Cloud pulsars. . 76

3-5 DM vs. $|b|$ for Galactic and Magellanic Cloud pulsars. 77

3-6 The 30 Doradus region of the LMC. 81

3-7 P-$\dot{P}$ diagram for Galactic and Magellanic Cloud pulsars. 88

3-8 Locations of O and B stars and 15 known SNRs in the SMC. 92

4-1 Radio pulse profiles for a subset of PM Survey pulsars. 105

4-2 Radio pulse profiles for a subset of PM Survey pulsars (continued). . 106

4-3 X-ray image of the region containing PSR J1420−6048. 109

4-4 Radio pulse profiles for PSR J1307−6318. 110

5-1 1.4-GHz on and off-pulse maps for PSR J1119−6127. 118

6-1 843-MHz image of the PSR J1119−6127 region. 129
6-2 1.4-GHz ATCA total intensity map of the shell G292.2−0.5. 132
6-3 2.5-GHz ATCA total intensity map of the shell G292.2−0.5. 133
6-4 Tomographic spectral index maps for G292.2−0.5. 135
6-5 PWN surface brightness upper limits for PSR J1119−6127. 138
6-6 IRAS 60-μm map of G292.2−0.5. 141
6-7 Galactic spiral arm locations and the line of sight to PSR J1119−6127. 143

A-1 FIRST/NVSS survey sensitivity curves. 162

B-1 Polarization profiles for PSRs J0045−7319 and J1105−6107. 174
B-2 Polarization profiles for PSRs J1341−6220 and J1646−4346. 175
B-3 Polarization profiles for PSR J1513−5908. 176
B-4 Polarization profiles for PSRs J1730−3350 and J1801−2306. 177
B-5 Polarization as a function of log $\dot{E}$ for six young pulsars. 185

List of Tables

2-1 Survey Parameters for Three High-frequency Pulsar Surveys 40

2-2 Tree Dedispersion Resampling Times and DM Ranges 53

2-3 Signal Enhancements from Harmonic Summing 53

2-4 Parameters for PM Survey Sensitivity Calculation 59

2-5 Comparison of Flux Densities for Seven Pulsars 60

2-6 187 New PM Survey Pulsars 61

2-7 Physical Parameters of New PM Survey Pulsars with $\tau_c < 100$ kyr . . 62

3-1 Currently Known Magellanic Cloud Pulsars 75

3-2 Astrometric and Spin Parameters for Newly Discovered Pulsars . . . 79

3-3 Refined Astrometric and Spin Parameters for Three Previously Known Pulsars 83

3-4 Predicted Number of Non-recycled SMC Pulsars 83

3-5 Luminosity Estimates for Magellanic Cloud Pulsars 89

3-6 Predictions from Two Luminosity Models 95

4-1 Observing and Astrometric Parameters for 39 PM Survey Pulsars . . 102

4-2 Spin Parameters for 39 PM Survey Pulsars 103

4-3 Physical Parameters for 39 PM Survey Pulsars 104

4-4 Measured Second Frequency Derivatives for Two Pulsars 110

4-5 Glitch Parameters for PSR J1413−6141 112

5-1 ATCA Observing Parameters for Seven Pulsars 119

5-2 ATCA Position Estimates for Seven Pulsars 122

5-3 ATCA Flux Density Estimates for Seven Pulsars 123

6-1 SNR Associations for Pulsars with $\tau_c < 10$ kyr 127
6-2 Parameters of Young Shell SNRs from Type II SNe 140
6-3 Sizes and Surface Brightnesses of Known PWNe 150
6-4 PWN Brightness Scaling Parameters 153

A-1 Positions of Observed FIRST/NVSS Sources 159
A-2 Parameters of Observed FIRST/NVSS Sources 160
A-3 Observed Test Pulsars 168

B-1 Physical Characteristics of the Pulsar Sample 187
B-2 Observing Parameters 188
B-3 Measured Polarization Parameters 189
B-4 Measured Pulse Widths and Rotation Measures 190
B-5 Astrometric and Spin Parameters for PSR J1316−6232 191

Chapter 1

Introduction

1.1 Discovery of Pulsars and Identification as Neutron Stars

Pulsars were first discovered accidentally in 1967 by a Cambridge University group conducting an experiment to study interplanetary scintillation. Jocelyn Bell and Anthony Hewish had constructed a transit antenna sensitive to low radio frequencies (81 MHz) and noticed strong fluctuations which appeared daily. These fluctuations were first attributed to terrestrial interference, but after further investigation it was found that the signals appeared four minutes earlier each day. This clearly indicated an extraterrestrial origin for the signals since they exactly tracked the sidereal rate of the sky. Further observations in November 1967 which were sensitive to fluctuations on shorter time-scales revealed that the signal was periodic with a period of $P = 1.337$ s. The discovery of this source, called CP1919 due to its right ascension ($\alpha = 19^{\rm h}\ 19^{\rm m}$) was published soon afterward (Hewish et al. 1968). It was hypothesized that pulsars could be rapidly spinning magnetized neutron stars, which were first predicted many years before (Baade & Zwicky 1934). In fact, Pacini (1967) suggested prior to the discovery of pulsars that such an object could be powering the Crab nebula. This hypothesis was confirmed in 1968 when pulsars were discovered in the Vela (Large, Vaughan, & Mills 1968) and Crab (Staelin & Reifenstein 1968) supernova remnants

(SNRs).

Other competing hypotheses for pulsars were soon ruled out. A white dwarf could not be responsible, since the fluctuation time-scale predicted for such an object could not be reconciled with the 33 ms period observed for the Crab pulsar. The observed secular increase in the period of the Crab pulsar (Richards & Comella 1969) ruled out a rapidly orbiting binary system. Such a system would be expected to have a decreasing period with time as the system lost energy. The energy output of the Crab nebula was also shown to be consistent with the predicted energy loss of a rotating magnetized neutron star with the Crab pulsar's period and period derivative, lending more support for this model (Gold 1969).

1.2 The Origin of Neutron Stars

For most of its life, a star maintains hydrostatic equilibrium by counterbalancing the effect of self-gravitation with thermal pressure, which is provided by the energy released in elemental fusion in the interior of the star. Light elements are fused into heavier elements, and when the abundance of a given element is depleted, the star begins to contract and heat up until the pressure and temperature become high enough to fuse the next heavier element.

If the star is massive enough ($M \sim$ 5-20 $M_{\odot}$), this "fusion ladder" can continue until iron is produced in the core from the fusion of silicon. Once iron is produced, the star can no longer produce heat and pressure in this manner, since fusion of iron is an endothermic process. The iron core grows from the continued fusion of silicon in a shell surrounding the core until degenerate electron pressure can no longer support the core against collapse. As the core exceeds the critical mass (equal to the Chandrasekhar mass) and collapses, the pressure at the center grows large enough that the electrons fuse with the protons in the iron nuclei:

$$p + e \rightarrow n + \nu. \tag{1.1}$$

This process, known as inverse β-decay, produces neutron-rich nuclei and the emission

of neutrinos.

If a sufficient number of protons in a nucleus are converted to neutrons in this manner, then the nucleus becomes unstable. Bound neutrons in this case would occupy the same quantum state, forbidden by the Pauli Exclusion Principle. Thus, the nuclei dissolve into free baryons. As the star begins to contract gravitationally, more iron nuclei become unstable, and a fluid of free neutrons and protons is produced in the core. The star's collapse continues until it is halted by repulsive forces between neutrons.

At this point, the outer layers of the star collapsing inward rebound off the neutron core, and, with the help of the pressure of the released neutrinos, are driven outward in a massive supernova (SN). This explosion can be visible at a number of wavelengths due to the conversion of a large amount of energy into radiation. Typically $\sim 10^{51}$ erg is released in the form of radiation and kinetic energy in a typical massive SN, though this is only $\sim 1\%$ of the energy contained in the neutrino emission.

The SN can leave behind a neutron star core, consisting chiefly of a fluid of free neutrons. Near the edge of this stellar remnant, the pressure is not high enough to cause the nuclei to dissolve, and a rigid crystalline crust of nuclei remains once the surface temperature drops sufficiently.

1.3 Pulsar Properties

1.3.1 Mass, Radius, and Density

A neutron star created in a SN has a radius of $R \sim 10$ km and has a mass $M \sim 1.4 M_{\odot}$, comparable to the Chandrasekhar mass of the core in the massive progenitor star. Neutron star densities can range from less than 10^4 g cm^{-3} for the crystalline solid at the surface to more than 10^{15} g cm^{-3} in the core. Above the surface of the star, the atmospheric density drops very sharply: the atmospheric scale height of the star is ~ 1 cm due to the large gravitational field.

1.3.2 Gravitational Field

The very strong gravitational field of a neutron star is easily demonstrated by considering its mass and radius. Assuming $M \sim 1.4 M_{\odot}$ and $R \sim 10$ km, the gravitational acceleration a is

$$a \sim \frac{GM}{R^2} \sim 10^{14} \text{ cm s}^{-2} \tag{1.2}$$

at the surface. This is eleven orders of magnitude larger than Earth's gravitational field. It is interesting to note that despite these large gravitational fields, the magnetic field completely dominates the dynamic behavior of charged particles external to the star.

1.3.3 Spin and Angular Momentum

Owing to the conservation of angular momentum during the star's collapse, the resulting neutron star can be spinning very fast, with a typical initial spin period thought to be $P_0 \sim$ 1-10 ms. Observed periods in the pulsar population range from 1.56 ms to 8.5 s, with the fastest members of the population believed to have been recycled and spun up to millisecond periods through accretion from binary companions over many years. This sub-population of recycled pulsars is known as the millisecond pulsar population. Typical spin periods for non-recycled pulsars are $P \sim 1$ s. The rotation of a pulsar is also very regular, with a rotational braking slowdown from energy losses corresponding to a typical period derivative of $\dot{P} \sim 10^{-15}$ s/s. Figure 1-1 shows the distribution of periods and period derivatives for the known pulsar population.

1.3.4 Magnetic Field

Magnetic flux through the star's surface is conserved during the star's collapse owing to the high electrical conductivity within the star. Since the surface area of the star decreases by a factor $\sim 10^{10}$ during its collapse to a neutron star, the magnetic field can increase by that same factor, giving surface field strengths of order $B \sim 10^{12}$ G in

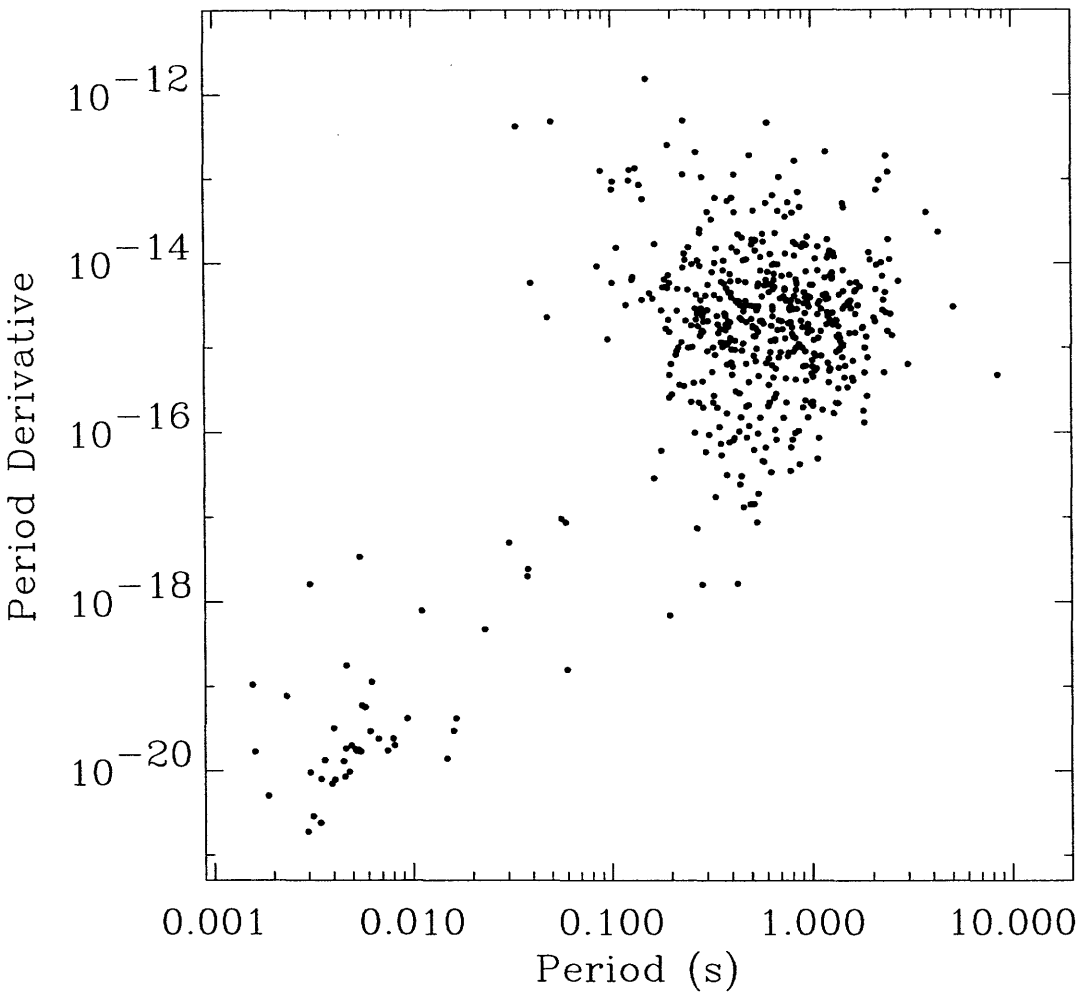

Figure 1-1 P-$\dot{P}$ diagram for the known pulsar population for which both P and $\dot{P}$ are cataloged. The majority of the population is clustered in the upper-right part of the diagram near $P \sim 1$ s and $\dot{P} \sim 10^{-15}$ s/s. The recycled millisecond pulsar population is located in the lower-left corner of the diagram.

typical pulsars. Also, any initial misalignment of the magnetic field with the rotation axis remains. As a simplifying assumption, the magnetic field can be modeled as a dipole. Deviations from the dipolar field can be tested with precise measurements of the timing behavior and polarization properties of pulsars.

1.3.5 Internal Properties

Many of the characteristics of the internal structure of pulsars are unclear, since any observational evidence of the internal makeup is indirectly obtained through pulsar observations. In addition, the equation of state of matter in the core of a neutron star, where the densities become extremely high, is not well known. However, a basic structural model has been proposed which fits observational results.

Near the surface, the matter is believed to be a rigid crust of iron nuclei in a sea of electrons. It is the high conductivity of the crust which is believed to be responsible for the persistence of the strong magnetic field. At a density of $\sim 4 \times 10^{11}$ g cm^{-3}, called the neutron drip point, the nuclei begin to dissolve into a superfluid of protons and neutrons. At higher densities, the matter consists chiefly of a neutron superfluid. Near the core of the star, the density may exceed 10^{15} g cm^{-3}, and the characteristics of the matter remain a mystery. At densities above $\sim 6 \times 10^{15}$ g cm^{-3}, the matter becomes relativistic, and the neutron star becomes unstable to collapse into a black hole.

1.3.6 The Induced External Electric Field

The free electrons surrounding the iron nuclei in the crust make the crust a very good conductor. Therefore, the pulsar can be modeled as a rotating conducting sphere in the presence of a strong magnetic field (Goldreich & Julian 1969). As the star rotates, every charged particle on the surface feels a Lorentz force from the magnetic field. This force causes a charge displacement which, in turn, induces a electric field. An equilibrium configuration is reached when the force on the charged particles from the induced electric field exactly cancels the Lorentz force. The induced electric field $\vec{E}$

is

$$\vec{E} = -\left(\frac{\vec{\Omega} \times \vec{r}}{c}\right) \times \vec{B}, \tag{1.3}$$

where $\vec{\Omega}$ is the spin angular frequency of the pulsar, $\vec{r}$ is the distance from the center of the star to the charge location, and $\vec{B}$ is the magnetic field strength at the charge location. It is notable that the gravitational field plays no role in the charged particle dynamics external to the star since the electromagnetic force is completely dominant. Thus the gravitational field can be safely ignored for these purposes.

1.3.7 Magnetospheric Radiation

The induced electric field accelerates the charged particles from the surface into a corotating region above the magnetic poles (the magnetosphere) in which the magnetic field is dominant. As the magnetic field lines begin to curve, the velocity of the particle is no longer parallel to the field lines, and the charge feels another Lorentz force, which is centripetal around the field lines. The particle begins to orbit the magnetic field line as it moves outward. However, since the magnetic field is so strong, the radius of orbit is very small, and it effectively travels along the magnetic field lines.

As the magnetic field line curves, the tightly bound particle curves also. This acceleration perpendicular to the field lines is known as curvature acceleration, and causes the particle to emit radiation in its instantaneous direction of motion. Curvature radiation dominates the synchrotron radiation from the tightly orbiting charges, so only the former mechanism needs to be considered in the general picture. As the magnetic poles and field lines rotate with the star, the accelerated charged particles radiate in a sweeping beam. This beam is coincident with the region of open field lines (which do not reconnect at the surface of the star), and this beam of radiation is seen as a train of radio pulses if the beam happens to sweep across our line of sight during the star's rotation. Although the general picture of this radiation mechanism is generally agreed upon, the details remain unclear, and no proposed model has

successfully accounted for all observations.

1.3.8 Magnetic Dipole Braking

To determine the energy loss of a pulsar from radiation, we can with good accuracy model the pulsar as a rotating magnetic dipole with higher order magnetic multipoles suppressed. Let the dipole moment of the pulsar be $\vec{m}$, inclined to the axis of rotation $\hat{z}$ by an angle α. $\vec{m}$ has a component along the axis of rotation, $\vec{m}_z$, and a component rotating in the xy-plane, $\vec{m}_{xy}$, perpendicular to the axis of rotation. We can split the rotating component into linear components along the $\hat{x}$ and $\hat{y}$ axes which are oscillating with the pulsar's angular rotation frequency Ω, but out of phase by $\pi/2$.

$$\begin{aligned} \vec{m}_z &= m\cos\alpha\hat{z} \\ \vec{m}_x &= m\sin\alpha\cos(\Omega t)\hat{x} \\ \vec{m}_y &= m\sin\alpha\sin(\Omega t)\hat{y}. \end{aligned} \tag{1.4}$$

Here m is the magnitude of the magnetic dipole. Note that $\vec{m}_z$ is time-independent.

The total amount of power radiated by an oscillating dipole in all directions is (e.g., Jackson 1962)

$$\dot{E} = \frac{2}{3c^3}\ddot{\vec{m}}^2, \tag{1.5}$$

where $\dot{E}$ is the time derivative of the oscillation energy. We take the double time derivative of $\vec{m}$ and assume the value of m at the surface of the star (along the magnetic axis) to be (Manchester & Taylor 1977)

$$m = BR^3, \tag{1.6}$$

where R is the neutron star radius and B is the surface magnetic field strength. We can rewrite the energy loss as

$$\dot{E} = -\frac{2B^2R^6\Omega^4}{3c^3}\sin^2\alpha. \tag{1.7}$$

This equation describes the change of the star's rotational kinetic energy with time and is equal to the time derivative of the kinetic energy:

$$\dot{E} = I\Omega\dot{\Omega}. \tag{1.8}$$

Setting Equations 1.7 and 1.8 equal and solving for $\dot{\Omega}$ yields

$$\dot{\Omega} = -\frac{2B^2R^6\Omega^3}{3Ic^3}\sin^2\alpha, \tag{1.9}$$

which is a measure of the slowdown of the pulsar from magnetic dipole braking.

1.3.9 Characteristic Age

From Equation 1.9, the rotational braking is described by a power law

$$\dot{\Omega} \sim -\Omega^n. \tag{1.10}$$

This expression can be integrated to obtain the time-scale τ for the loss of rotational energy for the pulsar (Manchester & Taylor 1977),

$$\tau = -\frac{\Omega}{(n-1)\dot{\Omega}}\left[1 - \left(\frac{\Omega}{\Omega_0}\right)^{n-1}\right], \tag{1.11}$$

where Ω_0 is the initial angular rotation frequency of the pulsar. By assuming that the pulsar was born with a spin frequency much higher than the one currently observed ($\Omega_0 \gg \Omega$) and assuming $n = 3$ for the dipole field approximation, we obtain a characteristic age for the pulsar, defined as

$$\tau_c \equiv -\frac{\Omega}{2\dot{\Omega}} = \frac{P}{2\dot{P}}, \tag{1.12}$$

where $P = 2\pi/\Omega$ is the spin period of the pulsar. We can therefore estimate the pulsar's age through the measurement of its period P and period derivative $\dot{P}$. For

the observed population, τ_c ranges from $\sim$ 1 kyr for the youngest known pulsars to $\sim$ 1 Gyr for some millisecond pulsars which have been recycled through spin up from an accreting companion over many years. However, typical lifetimes of pulsars are thought to be $\sim$ 10 Myr in the absence of recycling (Lyne, Manchester, & Taylor 1985).

1.3.10 Surface Magnetic Field Strength and Spin-Down Luminosity

By making the assumption that all of the energy loss is converted into magnetic dipole radiation, Equations 1.8 and 1.9 can be used to estimate the surface magnetic field strength B and spin down luminosity $\dot{E}$. Rewriting these parameters in terms of the spin period P and period derivative $\dot{P}$ yields

$$B = \left(\frac{3Ic^3}{8\pi^2 \sin^2 \alpha R^6}\right)^{1/2} (P\dot{P})^{1/2} \tag{1.13}$$

and

$$\dot{E} = -4\pi^2 I \left(\frac{\dot{P}}{P^3}\right). \tag{1.14}$$

These can be more conveniently written if we assume the canonical values of $R = 10^6$ cm, $I = 10^{45}$ g cm^2, and $\sin\alpha = 1$ for the pulsar. These expressions then become $B = 3.2 \times 10^{19}(P\dot{P})^{1/2}$ G and $\dot{E} = -3.94 \times 10^{46}(\dot{P}/P^3)$ erg s^{-1}.

1.4 Scientific Motivation for Pulsar Surveys and Follow-up Studies

Large-scale pulsar surveys provide the raw material with which studies of interesting pulsar systems are conducted. Chapters 2, 3, and Appendix A of this thesis describe three surveys for radio pulsars and the results of these surveys. Follow-up studies of the discoveries from pulsar surveys provide the scientific results. Chapters 3, 4, 5, 6,

and Appendix B of this thesis present various follow-up studies of pulsars and the scientific implications of this work.

There is a wide variety of issues that pulsar studies can address, and there are many ways one can conduct these studies. Some of the scientific goals of studying pulsars are outlined below.

The nature of physics in extreme conditions

Pulsars provide one of the few ways in which physics in extreme conditions can be studied in detail. Pulsars typically have large magnetic fields, large gravitational fields, and very high matter densities. None of these conditions can be reproduced in a terrestrial lab, so studies of pulsars are the only method by which we can gain information of physical behavior in such conditions. Such conditions also allow probes of fundamental physics in some cases. The details of the mechanism by which a pulsar radiates is not well understood, and in some cases new discoveries can be used to constrain or rule our emission models. Also, by studying pulse profile morphology and the polarization characteristics of the radio emission, the emission geometry of pulsars can be constrained and emission models can be tested (see Appendix B).

The pulsar population as a whole

One of the problems with any survey for pulsars is the serious selection effects at work which prevent a complete census of the population. In particular, selection effects against finding fast pulsars preferentially select against young pulsars (which are often rapidly spinning) and can bias models of the pulsar population and pulsar evolution. Understanding and modeling these selection effects is therefore important for any survey (see Chapter 2). By increasing the number of known pulsars and measuring the distribution of pulsars in the Galaxy, we can attempt to understand the underlying distribution of pulsars in the Galaxy. This has important implications for how and where pulsars are born, how often they are born, and the total number of pulsars in the Galaxy. In addition, a complete sample of pulsars allows us to understand the characteristics of the pulsar population and make statistical statements about

the population. The evolution of important physical parameters of pulsars, such as magnetic field strength, radio luminosity, and the emission beam shape, can also be addressed with a complete sample. Finding and studying pulsars in the Magellanic Clouds can also be used for these purposes (see Chapter 3).

Spin evolution of young pulsars

Young pulsars, on which this thesis concentrates, are often interesting to study individually (see Chapters 2, 4, 5, and Appendix B). They often exhibit timing noise, poorly understood timing irregularities. Timing noise is unmodeled behavior in pulsar rotation, and some pulsars show deviations from the standard spin-down model which vary on long time scales (months) relative to the spin period of the pulsar. Timing noise has been shown to be more prevalent among young pulsars (Arzoumanian et al. 1994), making timing solutions for young pulsars sometimes difficult to obtain. Timing studies of young pulsars can help address the question of what the mechanism causing timing noise is. Glitches, sudden spin-ups in the rotation of the pulsar, are also occasionally seen in young pulsars (see Chapter 4), and pulsar timing can accurately constrain glitch characteristics and help us understand the interior structure of neutron stars.

Timing parameters of young pulsars can be used to test models of the radio emission mechanism. In several cases a second frequency derivative $\ddot{f}$ can be measured, which allows a measurement of the braking index, n. Accurate measurements of n can be compared to the theoretical value of $n = 3$ for radiation from a purely dipolar rotating magnetic field, and models of the radiation emission mechanism can be tested (e.g., Melatos 1997) (see Appendix B).

Young pulsars and associated SNRs

Young pulsars are sometimes associated with SNRs (see Chapter 6). These associations allow important fundamental issues to be addressed involving the birth and evolution of pulsars and SNRs. Questions regarding the formation of pulsars, such as what fraction of SNe produce neutron stars (vs. black holes) and what fraction of

pulsar are formed in SNe (vs., e.g., accretion induced collapse) can be addressed with these studies. From studies of pulsar-powered nebulae, environmental parameters can also be constrained, such as the nature of the pulsar wind and the ambient density and pressure of the medium.

Finding and establishing associations between pulsars and SNRs is an important means by which we can understand the birth and evolutionary properties of both kinds of objects. Pulsars are believed to be born in SNe from massive progenitor stars (see Section 1.2), but confirmation of this scenario requires that young pulsars and SNRs be associated. Only a handful ($\sim$ 12) of the more than 220 cataloged Galactic SNRs (Green 1998)[1] have firmly established associations with young pulsars (Kaspi 1998). The question of why there are so few associations remains unanswered. Establishing new associations can help determine what selection effects are at work.

Pulsar and SNR associations also help us understand the properties of pulsars at birth. Physical parameters such as birth period, surface magnetic field strength, and radio luminosity can be constrained with a large enough sample of young pulsars, and estimates of the beaming fraction and total number of pulsars in the Galaxy have implications for the observability of pulsars and observational selection effects, as well as the spatial distribution of pulsars in the Galaxy. Thus, finding and studying pulsar and SNR associations is relevant for modeling and understanding the entire pulsar population.

Associations between pulsars and SNRs are typically established through a consistency in independently estimated ages and distances, and a spatial coincidence between the two objects. This provides a means for constraining these parameters for both objects and understanding their evolutionary properties. Distances to pulsars are usually determined from the Taylor & Cordes (1993) model of the distribution of free electrons in the Galaxy, which relates dispersion measure (DM) to distance. Distance estimates determined in this way suffer from significant uncertainties, and an independent distance estimate obtained from an associated SNR can reduce the distance uncertainty. Ages of pulsars in most cases are estimated from the characteristic

[1] http://www.mrao.cam.ac.uk/surveys/snrs/.

age of the pulsar, in which pure magnetic dipole energy losses are assumed as well as an initial spin period which is much smaller than the observed period. Independent age estimates of SNRs allow the initial spin period and spin-down behavior of pulsars to be constrained through a test of the assumptions going into the estimate of the characteristic age. The evolutionary history of a SNR can also be constrained by establishing its expansion velocity from a distance and age estimate from an associated pulsar (see Chapter 6). Associations reveal information about both types of systems which would otherwise not be obtainable from observing the systems separately.

Young pulsars can also interact with their environment through a pulsar wind. This plasma wind interacts with the ambient medium and in some cases the interaction can be seen in the form of reprocessed emission from a pulsar wind nebula (PWN), which is sometimes referred to as a plerion. The study of PWNe can help us understand and characterize the environment surrounding pulsars, such as the ambient density in which the pulsar resides and the speed and direction of motion of the pulsar. Models of pulsar and PWN evolution can also be tested, and observations of PWNe can act as a diagnostic for the poorly understood pulsar wind itself.

The Galactic environment

Pulsars provide a direct means of investigating the Galactic environment. Radio wave propagation effects reveal information about the environment between the observer and a pulsar (see Chapter 3). By studying the distribution of dispersive and scattering effects for the pulsar population, models of the Galactic plasma can be constructed and tested (Taylor & Cordes 1993). Rotation measures from polarization observations of pulsars can be used to investigate the structure of the ambient magnetic field in the Galaxy (see Appendix B).

1.5 Thesis Outline

This thesis describes several searches for new radio pulsars, the results of these searches, and a number of follow-up studies of newly discovered pulsars. Some of

the work presented here has also been submitted for publication elsewhere.

Chapter 2 describes the Parkes Multibeam Pulsar Survey (PM Survey), a major survey which is currently underway to find new pulsars in the plane of the Galaxy. A description of the survey and a detailed calculation of the survey sensitivity calibration is presented. The results of the survey to date, including the discovery of a new young radio pulsar with a very high magnetic field, are also presented.

Chapter 3 presents the results of a survey for pulsars in the Small Magellanic Cloud (SMC) using the same observing system as used for the PM Survey. The results of this survey, including the follow-up pulsar timing work on the new discoveries from the survey, and the scientific implications of these results are discussed.

Chapter 4 presents pulsar timing work conducted on a subset of the new pulsars discovered in the PM Survey. We estimate physical parameters for these pulsars from our timing results, and we discuss several of the interesting pulsars in the sample. These timing results will be part of a larger population synthesis modeling effort which will be conducted when the PM Survey has been completed.

Chapter 5 describes radio imaging of fields containing several young pulsars found in the PM Survey. Using pulsar gating, these observations are used to establish accurate positions and flux densities for the pulsars. The positions determined here facilitated timing solutions for the pulsars and, in some cases, were necessary to obtain a timing solution. The flux densities estimated here are used to check the PM Survey sensitivity calibration, which is presented in Chapter 2.

Chapter 6 describes more extensive radio imaging work on the field containing one of the young high-magnetic-field pulsar systems discovered in the PM Survey (described in Chapter 2). The radio imaging of this system has led to the discovery of a new shell radio SNR associated with this young pulsar. A model of the luminosity evolution of PWNe powered by young high-magnetic-field pulsars is also shown to be consistent with our imaging results.

Appendix A presents a targeted search of unidentified radio sources for radio pulsations. No radio pulsations are detected from any of these sources, and we discuss several effects which could prevent detection of pulsations.

Appendix B presents a polarization study of a sample of young radio pulsars. We use the polarization results to measure rotation measures and ambient magnetic field strengths in the Galaxy. We also significantly constrain the emission geometry of one of the pulsars in the sample. The constraints on this pulsar can be used in combination with further timing observations to test a proposed model of the pulsar magnetosphere.

Chapter 2

The Parkes Multibeam Pulsar Survey

2.1 Introduction

The Parkes Multibeam Pulsar Survey (PM Survey) is a high-frequency survey for radio pulsars in the Galactic plane which uses a receiver capable of simultaneously observing 13 separate locations on the sky. This multibeam receiver is mounted at the focus of the Parkes radio telescope, which is being used to conduct the survey.

The PM Survey involves a collaboration of researchers from a number of institutions. The survey team consists of the following people and institutions: Andrew Lyne, Michael Kramer, Ingrid Stairs, Nuria McKay, Dominic Morris (Jodrell Bank Observatory and the University of Manchester); Richard Manchester, Jon Bell (Australia Telescope National Facility); Victoria Kaspi, Fronefield Crawford (Massachusetts Insitute of Technology); Nichi D'Amico, Andrea Possenti (Bologna Astronomical Observatory); Fernando Camilo (Columbia University).

After a brief description of pulsar searching, we present the technical motivation for conducting the PM Survey. We then present a description of the survey and a detailed calculation of the survey sensitivity. We then discuss the survey results to date, including the discovery of PSR J1119−6127, an unusual young pulsar. Further study of PSR J1119−6127 is presented elsewhere in the thesis.

2.2 Searching for Pulsars

2.2.1 General Search Technique

Efforts to detect radio pulsar signatures typically make use of the unique property that pulsars have extremely steady spin periods on the time-scales of search observations. This allows even very weak pulsar signals to be detected by way of spectral (Fourier) analysis. The raw sensitivity to pulsar signals in an observation increases with longer integration times. Since pulsars are usually very weak, large telescope collecting areas are required to make a detection. There are a variety of factors which affect the sensitivity of a survey. A full outline of these factors is given in Section 2.6.

2.2.2 Interstellar Propagation Effects

The intervening plasma between a pulsar and observer introduces two important effects which can reduce the sensitivity of a pulsar search. Both of these effects are strongly dependent upon the radio observing frequency, and both effects become significantly worse at lower frequencies.

Interstellar Plasma Dispersion

In pulsar searches, the distance to the pulsar, and hence the amount of plasma between the observer and the pulsar, is unknown prior to the search. The presence of free electrons, which make up the largest fraction of the interstellar medium (ISM), introduces a dispersive effect which causes a frequency-dependent delay in a propagating radio pulse. Lower-frequency components arrive later than higher-frequency components, which results in a time-smearing of the pulse over a finite bandwidth. This pulse-smearing reduces the strength of the fundamental component in the Fourier domain as well as the harmonic components, and the sensitivity of the search is reduced. In most pulsar searches, a wide observing bandwidth B is split into evenly spaced frequency channels of width $\Delta\nu$, where $\Delta\nu \ll B$, in order to correct for this effect.

The group velocity of radio waves in the presence of a homogeneous plasma medium is (Manchester & Taylor 1977)

$$v_g = c\left(1 - \frac{\omega_p^2}{\omega^2}\right)^{1/2}, \tag{2.1}$$

where the plasma frequency ω_p in cgs units is defined as

$$\omega_p^2 = \frac{4\pi n_e e^2}{m_e}. \tag{2.2}$$

Here e and m_e are the charge and mass of the electron, respectively, in esu and g, and n_e is the number density of electrons in cm^{-3}.

The difference in times of arrival of a pulse at two frequencies ω_1 and ω_2 which are above the plasma frequency can be written (to first order in ω_p^2/ω^2) as

$$t_2 - t_1 = \frac{2\pi e^2}{m_e c}\left(\frac{1}{\omega_2^2} - \frac{1}{\omega_1^2}\right)\mathrm{DM}, \tag{2.3}$$

where DM is the dispersion measure, defined as the integrated electron density along the line of sight:

$$\mathrm{DM} = \int_0^L n_e\, dl. \tag{2.4}$$

After conversion to the radio observing frequency in Hz, $\nu = \omega/2\pi$, we can approximate the delay across a frequency bandwidth $\Delta\nu$ as

$$\tau_{\mathrm{DM}} = \left(\frac{202}{\nu}\right)^3 \mathrm{DM}\,\Delta\nu, \tag{2.5}$$

where τ_{DM} is in units of ms, ν is the center observing frequency in MHz, DM is the dispersion measure in units of pc cm^{-3}, and $\Delta\nu$ is the width of the frequency band in MHz. It is evident that the effect of dispersion smearing scales as ν^{-3} and grows significantly worse at lower observing frequencies. Therefore, in a pulsar observation the data must be dedispersed by delaying each frequency channel by an appropriate amount prior to summing the channels to counteract this effect.

Multipath Plasma Scattering

In principle, dispersive smearing can be reduced to a negligible level by dividing the bandwidth into a large number of small frequency channels and properly phase adjusting each channel separately. However, scattering of radio pulses, which also severely limits sensitivity to pulsed emission at low frequencies, cannot be accounted for even in principle with an arbitrarily large number of frequency channels.

When a radio wave passes through an inhomogeneous region of interstellar plasma, the index of refraction of the medium changes due to small fluctuations in the electron density (Manchester & Taylor 1977). Under the assumption that the scattering plasma region is a thin screen located midway between the observer and pulsar (Scheuer 1968), a time smearing is introduced in the impulsive signal since the scattered rays suffer a time delay relative to the unscattered rays. For a power law distribution in the inverse spatial scale q of plasma density inhomogeneities which scales as

$$\Phi(q) \sim q^{-\beta}, \tag{2.6}$$

the intrinsic shape of the impulse is convolved with a truncated exponential function of the form

$$\begin{aligned} g(t) &= e^{-t/\tau_s} \qquad (t \geq 0) \\ &= 0 \qquad\quad (t < 0), \end{aligned} \tag{2.7}$$

where the characteristic time-scale τ_s of the pulse smearing scales as $\nu^{-2\kappa}$ where $\kappa = \beta/(\beta - 2)$ (Manchester & Taylor 1977). For a Kolmogorov spectrum of the size scale of turbulence, $\beta = 11/3$, which yields a frequency dependence for the pulse smearing from scattering of

$$\tau_s \sim \nu^{-4.4}. \tag{2.8}$$

Like the plasma dispersion effects described above, scattering becomes much worse at lower frequencies and can prevent detection of even strong pulsar signals.

2.3 Survey Motivation

The scientific motivation for conducting the PM Survey is outlined in Chapter 1. Finding a large number of pulsars and understanding the selection effects in a pulsar survey is necessary for modeling the underlying pulsar population. A large enough population of observed pulsars can also be used to model and constrain the Galactic environment. Interesting individual systems are also found in large-scale surveys for pulsars and can be studied separately once they are discovered.

The technical motivation for conducting the PM Survey is two-fold. First, the high frequency of the survey reduces the pulse smearing effects described above which can make a pulsar signal undetectable. Second, the multiple beams of the receiver allows increased sensitivity with long integrations without using an excessive amount of telescope time.

2.3.1 High Radio Observing Frequency

Most previous surveys for radio pulsars have been conducted at low observing frequencies ($\sim$ 400 MHz, see Camilo 1997 and references therein), since pulsars are are typically steep-spectrum sources. The average spectral index is $\alpha \sim -1.6$ for the population (Lorimer et al. 1995), where α is defined as $S \sim \nu^{\alpha}$. However, there are significant advantages to conducting a pulsar survey at high frequencies. The two plasma propagation effects described in Section 2.2.2 (dispersive smearing and multipath scattering) which reduce sensitivity to pulsed radio emission are greatly reduced. In fact, many distant pulsars in the plane of the Galaxy (where there are significant concentrations of interstellar plasma) are expected to have been missed in previous low-frequency surveys.

From Equations 2.5 and 2.8, it is evident that dispersive smearing is $\sim$ 40 times worse at 400 MHz than at 1400 MHz for a given bandwidth and scattering can be $\sim$

250 times worse. Since both dispersive and scattering effects are particularly severe for distant, highly dispersed pulsars in the Galactic plane, observing at a high radio frequency is necessary to maintain sensitivity to such pulsars.

2.3.2 The Multibeam Receiver

The PM Survey makes use of a new piece of technology, the multibeam receiver (Staveley-Smith et al. 1996).[1] This receiver is capable of observing 13 distinct parts of the sky at once, thereby greatly increasing observing efficiency and countering the effect of the longer integrations which are required at higher frequencies for comparable sensitivity. An additional advantage of using this instrument is that the receiver has a lower system temperature than previous 1400-MHz receivers at Parkes, which reduces the noise level in the system and improves the sensitivity to pulsar signals.

The multibeam receiver contains 13 identical feeds mounted on a single stage, each of which is sensitive to radio emission in dual linear polarizations. The feeds are cryogenically cooled to a $\sim$ 21 K (36 Jy) system temperature using HEMT low-noise amplifiers and cover a radio frequency range of 1230 MHz to 1530 MHz. The FWHM (half-power) beam coverage of each feed horn at 1374 MHz (the center frequency of the PM Survey) is $\sim 15'$. The thirteen horns are disposed in a hexagonal pattern, each separated by 25 cm, corresponding to a separation of about two beamwidths on the sky ($29'$). Figure 2-1 shows a photograph of the multibeam receiver prior to its installation on the Parkes telescope. The receiver configuration and beam separation allow pointings to be interleaved in such a way as to obtain complete sky coverage in an efficient manner. Figure 2-2 shows a sample set of beam placements from four pointings interleaved for complete coverage of a region.

[1]Details of the multibeam receiver and its capabilities can be found at http://www.parkes.atnf.csiro.au.

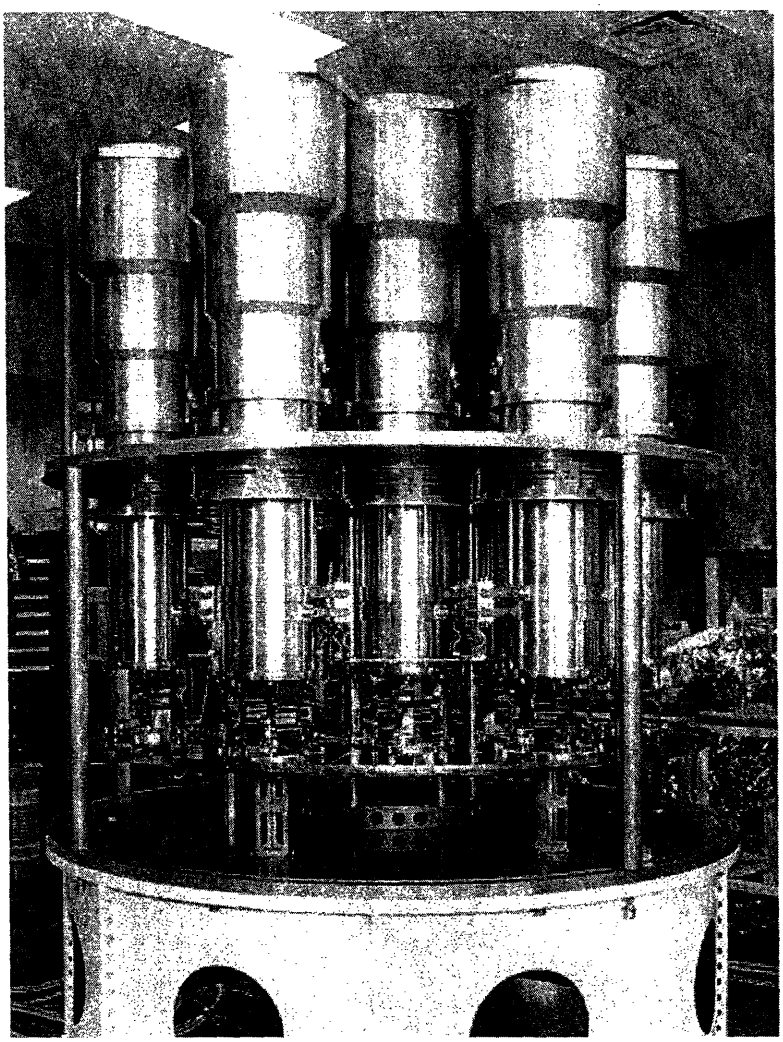

Figure 2-1 A picture of the multibeam receiver prior to installation on the Parkes telescope.

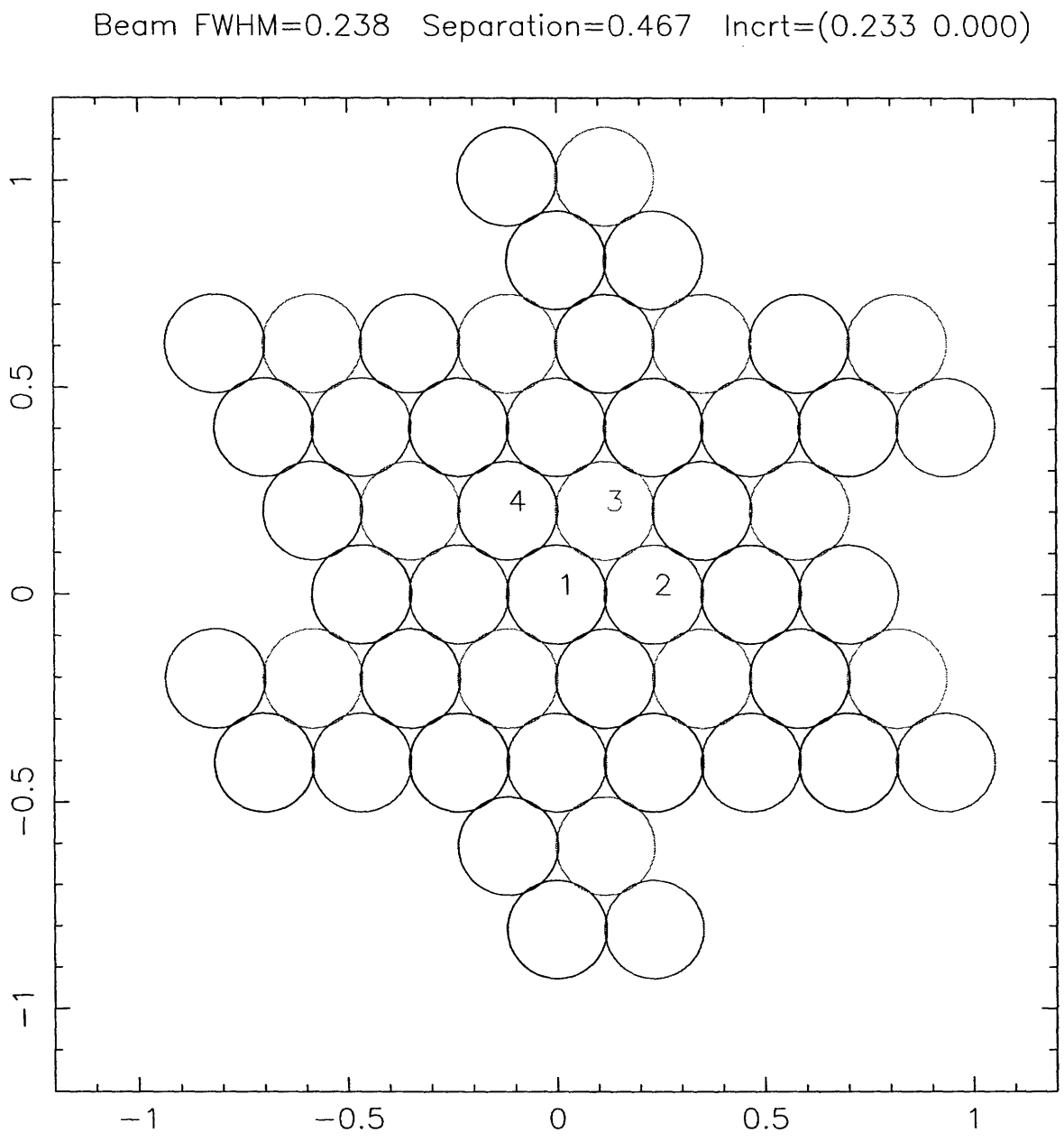

Figure 2-2 Sky positions of beams from four interleaved multibeam pointings. The four pointings are color-coded with the center beam of each pointing labeled with the pointing number. These clusters are then interleaved for tiled sky coverage. The units on both axes are offset degrees from the center beam of the first pointing.

2.4 Comparison with Previous High-Frequency Pulsar Surveys

Only two large-scale high-frequency pulsar surveys have been conducted prior to the PM Survey. Clifton et al. (1992) used the Lovell 76-m telescope to survey the northern sky within 1° of the Galactic plane and surveyed a total of $\sim$ 210 sq. deg. Johnston et al. (1992a) used Parkes to survey 880 sq. deg. of the sky within 4° of the Galactic plane. Both of these surveys were very successful, discovering 40 and 46 new pulsars respectively. At the time, this represented $\sim$ 15% of the known pulsar population of about 560.

Table 2-1 outlines the parameters for both of these surveys and the PM Survey. More details of the two previous surveys can be found in the survey papers themselves. From a comparison of the raw sensitivity of the surveys, one can see that the PM Survey is $\gtrsim 7$ times more sensitive than the Johnston et al. (1992a) survey. This is due primarily to the longer integration time per pointing and better system temperature. Our faster sampling rate and smaller frequency channel widths make the PM Survey more sensitive to fast pulsars. The area surveyed by the PM Survey is also larger. These factors suggest that the PM Survey ought to find a significant number of previously undetected pulsars in the Galactic plane. Initial estimates suggested that 400-500 new pulsars could be discovered in the survey.

2.5 Survey Description

2.5.1 The Parkes 64-m Telescope

The PM Survey uses the Parkes 64-m telescope[2] in Parkes, NSW, Australia to survey the sky for pulsars. A schematic of the Parkes telescope is shown in Figure 2-3. The telescope is a fully steerable paraboloid dish with a 64-m diameter and a focal ratio

[2]http://www.parkes.atnf.csiro.au. The Parkes Observatory is part of the Australia Telescope, which is funded by the Commonwealth of Australia for operation as a National Facility managed by CSIRO.

Table 2-1. Survey Parameters for Three High-frequency Pulsar Surveys

Survey	Clifton et al.	Johnston et al.[a]	PM Survey
Year Published	1992	1992	ongoing
Telescope	Lovell 76-m	Parkes 64-m	Parkes 64-m
Center Frequency (MHz)	1400	1520	1374
Longitude Range	$-5° < l < +100°$	$-90° < l < +20°$	$-100° < l < +50°$
Latitude Range	$\|b\| < 1°$	$\|b\| < 4°$	$\|b\| < 5°$
Survey Area (sq. deg.)	210	880	1550
Number of Beams	1	1	13
Integration Time (min)	10	2.5	35
Bandwidth (MHz)[b]	40 ($2 \times 8 \times 5$)	320 ($2 \times 64 \times 5$)	288 ($2 \times 96 \times 3$)
Sample Time (ms)	2.0	1.2	0.25
System Temperature (Jy)	60	70	36
Sensitivity (mJy)	1.2	1.0	0.15
Pulsars Found/Detected	40/61	46/100	569+/783+

[a]Parameters from System II of this survey.

[b]Total bandwidth (number of detected polarizations $\times$ number of frequency channels $\times$ channel width in MHz).

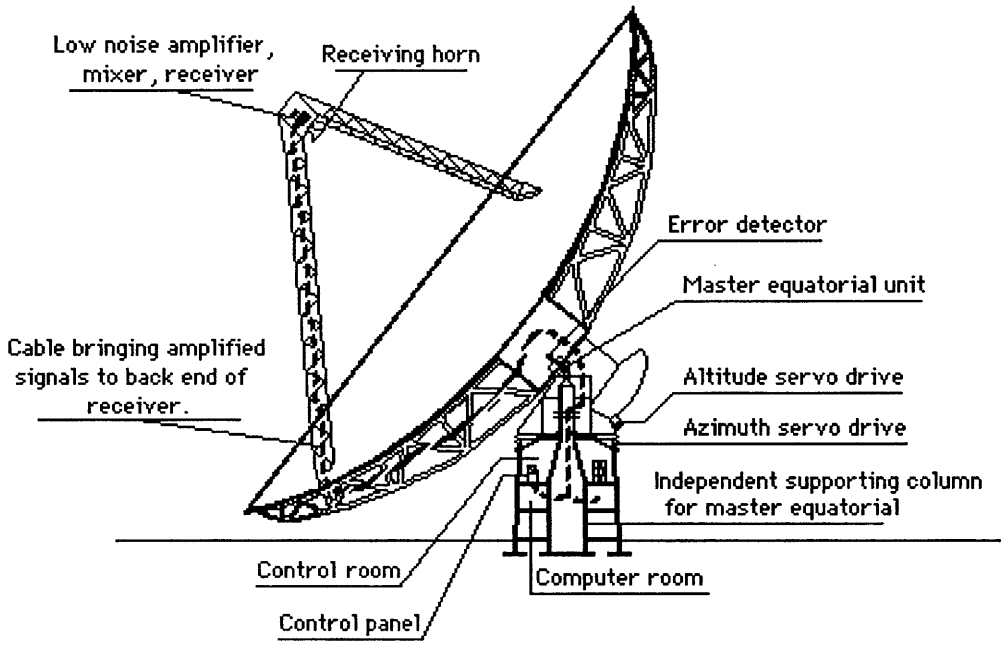

Figure 2-3 A schematic diagram of the Parkes 64-m telescope.

of 0.41 (corresponding to a focus point 26 m above the dish center). An aerial cabin is located at the focal point which houses several receivers, including the multibeam receiver, described above in Section 2.3.2.

2.5.2 Data Acquisition

Radio signals reflected off the dish are detected at the focus by the receiver in orthogonal linear polarizations in each of the 13 feeds separately. The 26 signals are amplified, downconverted, and sent to a filterbank system in the control room. The filterbank provides 2 polarizations $\times$ 96 frequency channels $\times$ 3-MHz channels (288-MHz total bandwidth) for each of the 13 feeds. Bandlimited signals in each channel are square-law detected and added in polarization pairs before being high-pass filtered, one-bit digitized every 0.25 ms, and recorded on magnetic tape (DLT) for later analysis.

2.5.3 Interference Rejection

Since observatory-generated and externally generated radio frequency interference (RFI) regularly appear and are significant factors which reduce the sensitivity of the survey, the data are checked for interference after being recorded but prior to processing. Data are read from DLT tape to disk on Sun workstations, with data from each beam split and stored for each integration as a separate file. The frequency channels are summed and the resulting time series for each beam is Fourier transformed to form a zero-DM amplitude spectrum (since RFI is not expected to be dispersed). The strongest candidates (with signal-to-noise ratio of at least 8) in each spectrum are recorded as potential RFI signals. The fact that the multibeam system has multiple beams can be used to separate pulsar signals from RFI. Externally generated RFI usually appears in multiple beams whereas a pulsar signal generally appears in only one beam. Thus, signals and their harmonics which appear in more than 4 beams of a given pointing are flagged as RFI. Both externally and internally generated RFI can also appear intermittently in more than one pointing. Therefore signals are flagged if they or their harmonics appear in a given beam in 4 different pointings (in which the telescope is looking at different parts of the sky), since multiple appearances would not be expected for a pulsar signal. The modulation frequencies which satisfied one of these conditions are masked in the spectrum along with harmonics for that particular data set in the processing.

2.5.4 Data Processing and Analysis

Data are then reread from DLT tape and again split into separate files for each beam in each pointing. In the search processing, channels are dedispersed at DM trials ranging from 0 to 2203 pc cm^{-3}. For the PM Survey, a tree dedispersion routine is used (Taylor 1974; Manchester et al. 1996). In this method, linear dedispersions valid over small bandwidths are first applied to 6 sub-bands of 16 channels each. 16 trial dedispersions are produced which range from 0 to 35 pc cm^{-3}, the value at which the dispersive smearing τ_{DM} in the highest-frequency channel equals the sample time

of 0.25 ms. A further 16 DM trials are extended out to 70 pc cm^{-3}. The original data are then resampled by summing the samples in pairs to produce an effective sample time of 0.5 ms, twice that of the original. The sub-bands are then dedispersed at another 16 trial DMs ranging from 70 pc cm^{-3} to 139 pc cm^{-3}. This process is repeated for subsequent DM ranges (folds) with resampling times of 1.0, 2.0, 4.0, and 8.0 ms.

Once the dedispersion of the sub-bands has been completed, the sub-bands are combined with appropriate delays corresponding to trial DMs near each of the 16 DMs in each fold. Delays in this case are computed according to the quadratic dispersion relation. Table 2-2 shows the DM range searched and the DM step used for each DM fold.

After the data are dedispersed and summed in each DM trial, the resulting time series is high-pass filtered in software before an amplitude spectrum is formed from a Fast Fourier Transform (FFT) (e.g., Press et al. 1992). The modulation frequency filters from the RFI rejection routine are then applied to the spectrum, and the strongest remaining candidates recorded.

The original data are then reprocessed for each candidate with a signal-to-noise ratio (S/N) of at least 8. The original data are dedispersed and folded at DMs and periods near the candidate DM and period to check for a pulsar-like signature.

2.5.5 Survey Area

By the time it is completed, the PM Survey will have observed 2670 unique pointings in the Galactic plane in the range $-100° < l < +50°$ and $-5° < b < +5°$. This survey area is about 1550 sq. deg., almost twice as large as the area surveyed by Johnston et al. (1992a) and about 7 times larger than the area surveyed by Clifton et al. (1992). Each multibeam pointing is 35 min, corresponding to $\sim$ 1550 h of integration time to complete the entire survey. The total data storage required for the survey is $\sim$ 5 Terabytes.

2.6 Sensitivity Calibration

2.6.1 Background

In order to understand the characteristics and evolution of the pulsar population as a whole, it is important to understand the selection effects which play a role in any survey for new pulsars. The survey sensitivity ideally is a function of P, DM, and the observing parameters, but in practice there are other effects which come into play. First, different pulsars have different duty cycles and pulse profile morphologies which affect the detectability of a signal in a pulsar search observation. This variation is impossible to model for the population as a whole since there is such a variety. Other effects, such as RFI and scintillation, can affect how strongly the signal is detected against a noise background. There are also effects related to instrumentation, such as time-variability in the system temperature of the receiver and, in the case of the multibeam receiver, variations in the system temperatures for different beams. Different parts of the sky observed during the course of a survey also have different sky temperatures. This contributes different amounts of noise to the receivers. Also, the pulsar is not always at the beam center (where the sensitivity is greatest) in a survey observation, and this affects the detectability as well.

In short, there are many effects which cannot be modeled and calibrated for in a general way, but it is important to have an idealized estimate of the sensitivity of a survey from which to work in which as many effects as possible are modeled and accounted for. The sensitivity estimate for the PM Survey which is described here accounts for propagation effects in the ISM, hardware and software filtering effects, and the details of the data processing. Since the processing procedure in software is complicated and the calculated sensitivity is not analytic for all input parameters, the sensitivity must be modeled individually for each trial P and DM. Once the sensitivity value has been calculated for each trial, the values can be combined to get a full sensitivity curve for a range of P and DM.

2.6.2 Calculation of Survey Sensitivity

We estimate the sensitivity of the PM Survey by first considering an idealized pulsar signal to be an infinite train of delta functions in the time domain. This idealized function is convolved with a series of functions which represent both instrumental and astrophysical filtering effects. The fact that the intrinsic pulse width is in reality finite can be accounted for in a similar convolution.

The effect of the convolution of all these filters (represented in the time domain by the function $G(t)$) with the idealized pulse train $F(t)$ in the time domain is a multiplication in the Fourier domain

$$F(t) \otimes G(t) \Longleftrightarrow F(f)G(f), \tag{2.9}$$

where $f \equiv 1/P$ relates to the Fourier conjugate Ω of t according to $f = \Omega/2\pi$ and is the modulation frequency of the pulses.

In the pulsar search analysis, the amplitude spectrum is used, which is the magnitude of the power spectral density function. We are interested in the quantity

$$|F(f)|\,|G(f)|\,, \tag{2.10}$$

where

$$\begin{aligned} |F(f)| &= \sqrt{F^*(f)F(f)} \\ |G(f)| &= \sqrt{G^*(f)G(f)}. \end{aligned} \tag{2.11}$$

Here the asterisk indicates the complex conjugate of the function. Since the Fourier representation of the filters (whose product equals $G(f)$) is completely real in each of the cases we consider, it does not matter whether the magnitude of each filter is taken of separately before or after the product is formed. The reduction in signal strength due to the application of these filters in the Fourier domain is then the inverse of the scaling factor applied to the minimum detectable flux density, which is determined

from the given observing parameters.

We first take the Fourier transform of our idealized pulse train of delta functions $F(t)$. If the pulse separation in the time domain is P (the pulse period), then the Fourier transform $F(f)$ will give an infinite series of delta functions in the amplitude spectrum which have equal amplitudes located at integer multiples n of the fundamental modulation frequency $f_1 = 1/P$ in the Fourier domain:

$$f_n = \frac{n}{P}. \tag{2.12}$$

We let the amplitude of each of these n signals be a constant y_0, which is the inverse of the raw sensitivity, determined by the system parameters:

$$y_0 = \frac{\sqrt{B t_{\rm int} N_p}}{\sigma \beta G T_{\rm sys}}. \tag{2.13}$$

Similar expressions have been used in calculations of the raw sensitivity in previous pulsar searches (e.g, Dewey et al. 1985). Here σ and β are a digitization loss constant and a detection S/N threshold respectively, G is the telescope gain, $T_{\rm sys}$ is the system temperature, B is the observing bandwidth, $t_{\rm int}$ is the observing integration time for each observation, and N_p is the number of orthogonal polarizations detected.

Each of the signals y_0 in the Fourier spectrum at f_n will be attenuated by a series of filters. We consider only the fundamental and first 15 harmonics in the calculation (f_1 through f_{16}) since the processing software only considers these.

Low-pass Filtering from the Intrinsic Pulse Width

We make the assumption that the pulses propagating from the pulsar are in reality intrinsically Gaussian with FWHM width W. In our calculation, we set W equal to 5% of P as the standard assumption for the pulsed duty cycle. Of course, in reality there is a wide range of pulse morphology.

The time series resulting from the convolution of the assumed Gaussian form $g_1(t)$ with the original idealized pulse train $F(t)$ of delta functions yields the filtered time series. The general (unnormalized) form of the Gaussian filter is

$$g_1(t) = \exp\left(-\frac{t^2}{2\sigma^2}\right), \tag{2.14}$$

where σ is the characteristic width of the function. This has the Fourier transform

$$g_1(f) = \exp\left(-\frac{(2\pi f)^2\sigma^2}{2}\right), \tag{2.15}$$

where we have normalized the peak of the function to unity. We rewrite the expression using the FWHM width $W^2 = 8\ln 2\sigma^2$ to get

$$g_1(f) = \exp\left(-\frac{\pi^2 f^2 W^2}{4\ln 2}\right). \tag{2.16}$$

Note that this expression is identical to $|g_1(f)|$, which is the quantity of interest for the filter.

Low-pass Filtering from Filterbank Channels

To account for the effect of dispersive smearing within individual filterbank channels, we assume that the channels are also Gaussian in shape and consider another Gaussian filter of FWHM width $\tau_{\rm DM}$ in the time domain. $\tau_{\rm DM}$ is a measure of the dispersive smearing across each channel (Equation 2.5). Following from Equation 2.16, the channel filter $g_2(f)$ can be written

$$g_2(f) = \exp\left(-\frac{\pi^2 f^2 \tau_{\rm DM}^2}{4\ln 2}\right). \tag{2.17}$$

Here $|g_2(f)| = g_2(f)$ as was the case of $g_1(f)$.

For the PM Survey, the center frequency ν is 1374 MHz and the frequency channel width $\Delta\nu$ is 3 MHz. The DM is a variable input parameter in the calculation.

Hardware Low-pass Filtering from Sampling

The effect of finite sampling must also be considered. In the observing system, the power is integrated for a time $t_{\rm samp}$ and then is output as a single value. Thus, the effect on the time series is a low-pass boxcar filter of full width $t_{\rm samp}$, defined according

to

$$\begin{aligned} g_3(t) &= 1 \qquad (|t| < t_{\rm samp}/2) \\ &= 0 \qquad (|t| > t_{\rm samp}/2). \end{aligned} \tag{2.18}$$

The Fourier transform of this filter is

$$g_3(f) = \frac{\sin(\pi f t_{\rm samp})}{(\pi f t_{\rm samp})}, \tag{2.19}$$

with normalization equal to unity. In this case, $|g_3(f)|$ does not equal $g_3(f)$ for all f, since $g_3(f)$ can be negative. Thus we use

$$|g_3(f)| = \left| \frac{\sin(\pi f t_{\rm samp})}{(\pi f t_{\rm samp})} \right| \tag{2.20}$$

for the filter to be applied in the calculation.

Since tree dedispersion is used in the processing, the effective sampling time will depend on the DM being considered since the data are resampled at larger sampling times in each successive DM fold (see Table 2-2). Hence, $t_{\rm samp}$ must be adjusted in the calculation for different DM ranges.

Hardware High-Pass Filter

Prior to digitization, the signals are high-pass filtered in hardware in order to eliminate slowly varying baseline levels. For an RC time constant high-pass filter with characteristic time τ_H, the Fourier filter which we apply to the amplitude spectrum is (Horowitz & Hill 1989)

$$|g(f)| = \frac{(2\pi f \tau_H)}{[1 + (2\pi f \tau_H)^2]^{1/2}}. \tag{2.21}$$

For the PM Survey a two-pole filter is used which has greater attenuation at low frequencies. This filter is defined as (Horowitz & Hill 1989)

$$|g(f)| = \frac{(2\pi f \tau_H)^n}{[1 + (2\pi f \tau_H)^{2n}]^{1/2}}, \tag{2.22}$$

with $n = 2$. For the PM Survey, $\tau_H \sim 2$ s.

Software High-Pass Filter

During processing, the software performs a boxcar low-pass filter with full width τ_S on the dedispersed time series, then subtracts this resulting time series from the original time series, resulting in a high-pass filtered time series. This filtering accounts for effects which are introduced after the hardware high-pass filtering is done. This process can be represented as

$$F_{\text{high}}(t) = F_{\text{orig}}(t) - F_{\text{low}}(t), \tag{2.23}$$

where $F_{\text{orig}}(t)$, $F_{\text{low}}(t)$, and $F_{\text{high}}(t)$ are the original, low-pass filtered, and resulting high-pass filtered time series. We Fourier transform this to obtain

$$F_{\text{high}}(f) = F_{\text{orig}}(f) - F_{\text{low}}(f). \tag{2.24}$$

Again using the expression for the Fourier transform of the boxcar filter (Equation 2.19), we rewrite $F_{\text{low}}(f)$ to get

$$F_{\text{high}}(f) = F_{\text{orig}}(f) - F_{\text{orig}}(f)\left[\frac{\sin(\pi f \tau_S)}{(\pi f \tau_S)}\right], \tag{2.25}$$

which is

$$F_{\text{high}}(f) = F_{\text{orig}}(f)\left[1 - \frac{\sin(\pi f \tau_S)}{(\pi f \tau_S)}\right] \tag{2.26}$$

$$F_{\text{high}}(f) = F_{\text{orig}}(f) g_5(f). \tag{2.27}$$

Here $g_5(f)$ is the relevant filter to be applied in the Fourier domain. Since $g_5(f)$ is real and is never negative, $|g_5(f)| = g_5(f)$. Also, in some cases $|g_5(f)| > 1$. Thus for

the software high-pass filter we have

$$|g_5(f)| = 1 - \frac{\sin(\pi f \tau_S)}{(\pi f \tau_S)}. \tag{2.28}$$

For the PM Survey, τ_S is determined by the first power-of-two multiple of the sampling time $t_{\rm samp}$ which exceeds 2 s. For the PM Survey, $t_{\rm samp}$ is 0.25 ms, giving $\tau_S = 2.048$ s. Since the resampling during the tree dedispersion is always a power of two of $t_{\rm samp}$ (see Table 2-2), τ_S is not affected by the resampling of the data and remains constant throughout the calculation.

Application of the Filters

In the Fourier domain, each of the 16 signals y_0 at frequencies f_n undergoes multiplication by the product of all of these filters. If $y(f_n)$ is the signal strength at f_n after the application of the filters, then

$$y(f_n) = y_0 |g_1(f_n)||g_2(f_n)||g_3(f_n)||g_4(f_n)||g_5(f_n)|. \tag{2.29}$$

In all cases (except g_5 when $\sin(\pi f_n \tau_S)/(\pi f_n \tau_S) < 0$) the filters act to reduce the signal strength.

In the data processing, all 16 frequencies f_n are checked to see if they fall into a range which is invalid in the processing. The invalid regions are $f < 1/P_{\rm max}$, which is a constant set in the software (for the PM Survey, $P_{\rm max} = 5$ s), and $f > 1/(2t_{\rm samp})$, the Nyquist frequency. $P_{\rm max}$ is set in order to prevent signals from slow baseline variations from appearing in the spectrum. For tree dedispersion, the effective $t_{\rm samp}$ varies with DM, and the Nyquist frequency used in this check will also vary with DM. All signal strengths $y(f_n)$ with f_n in invalid regions are set to zero for the calculation (indicating no signal strength and no sensitivity to these signals).

If the fundamental frequency f_1 under consideration falls below $1/P_{\rm max}$ and is in an invalid frequency range, then successive harmonics are checked until the first one in the valid range is found. This harmonic is then used as the fundamental in the filter calculations (above) and in the harmonic summing (below). For instance, if

the third harmonic were found to be first valid signal, then the harmonic summing would include this third harmonic, the sixth harmonic, the ninth harmonic, etc., of the original fundamental.

Harmonic Summing

The evenly spaced harmonics in the amplitude spectrum can be added in a way which enhances sensitivity (e.g., Nice, Fruchter, & Taylor 1995). This technique, known as harmonic summing, can be used to detect an otherwise undetectable pulsar signal. In this process, the values in the amplitude spectrum are altered in the following way.

1. The value at each location n in the spectrum (where $2n$ does not exceed the Nyquist frequency) is added to the value in the spectrum at location $2n$. Let the result be spectrum A.

2. The value at each location n in the original spectrum (where $4n$ does not exceed the Nyquist frequency) is added to the values in this spectrum at locations $4n$ and $4n/3$, and this sum is added to the value at location n in spectrum A. Let the result be spectrum B.

3. The value at each location n in the original spectrum (where $8n$ does not exceed the Nyquist frequency) is added to the values in this spectrum at locations $8n$, $8n/3$, $8n/5$, and $8n/7$, and this sum is added to the value at location n in spectrum B. Let the result be spectrum C.

4. The value at each location n in the original spectrum (where $16n$ does not exceed the Nyquist frequency) is added to the values in this spectrum at locations $16n$, $16n/3$, $16n/5$, $16n/7$, $16n/9$, $16n/11$, $16n/13$, and $16n/15$, and this sum is added to the value at location n in spectrum C. Let the result be spectrum D.

This process could be continued to higher orders, but as a practical matter the harmonic summing stops at this point. The four spectra A through D (not including the original) each have enhanced sensitivity to signals at certain harmonics of the fundamental. The noise in each composite spectrum is the quadrature sum of the

noise in each of the spectra which are used to make the composite spectrum. Table 2-3 outlines the harmonic enhancement in sensitivity for the spectra described above.

In our calculation, the signals $y(f_n)$ in the spectrum at the n = 2,4,8, and 16 frequencies are enhanced according to

$$y'(f_n) = \frac{\sum_{i=1}^{n} y(f_n)}{\sqrt{n}}. \tag{2.30}$$

The largest $y'(f_n)$ for n = 1,2,4,8, or 16, which we call $y'_{\rm max}(f_n)$, is taken as the value which determines the minimum detectable flux density $S_{\rm min}$ for a pulsar with the assumed P and DM in the calculation:

$$S_{\rm min} = \frac{1}{y'_{\rm max}(f_n)}. \tag{2.31}$$

Note that in the absence of the filtering effects described above and with no harmonic summing, $y'_{\rm max}(f_n) = y_0$ and the raw sensitivity is recovered:

$$S_{\rm min} = \frac{1}{y_0}, \tag{2.32}$$

which is simply

$$S_{\rm min} = \frac{\sigma \beta G T_{\rm sys}}{\sqrt{B t_{\rm int} N_p}}. \tag{2.33}$$

Figure 2-4 shows a plot of the sensitivity of the PM Survey for a range of P and representative DM values of 0, 100, 500, and 1000 pc cm^{-3}. The parameters for the filters described above are presented in Table 2-4. There are a number of features which can be seen in the curves. At low DMs, the effect of harmonic summing can be clearly seen as discrete changes in the sensitivity at several power-of-two multiples of the sampling time. These changes occur at the transition periods of the fundamental at which harmonics fall below the Nyquist frequency and therefore are considered in the harmonic summing. At larger DMs, these jumps are not as evident since the harmonics are significantly attenuated at high frequencies and do not as much to the harmonic summing. The scalloped features evident between about 100 ms and 1 s in

Table 2-2. Tree Dedispersion Resampling Times and DM Ranges

DM Fold	Resampling Factor	Sample Time (ms)	DM Range (pc cm^{-3})	DM Step (pc cm^{-3})
0	1	0.25	0 - 35	0.54
1	1	0.25	35 - 70	0.80
2	2	0.50	70 - 139	1.61
3	4	1.00	139 - 276	3.22
4	8	2.00	276 - 551	6.44
5	16	4.00	551 - 1114	12.9
6	32	8.00	1114 - 2203	25.8

Table 2-3. Signal Enhancements from Harmonic Summing

Spectrum[a]	Original	A	B	C	D
Noise increase factor	1	$\sqrt{2}$	2	$2\sqrt{2}$	4
Signal increase (n=1)[b]	1	1	1	1	1
Signal increase (n=2)[b]	1	2	2	2	2
Signal increase (n=4)[b]	1	2	4	4	4
Signal increase (n=8)[b]	1	2	4	8	8
Signal increase (n=16)[b]	1	2	4	8	16
S/N increase (n=1)[c]	1[d]	$\sqrt{2}/2$	1/2	$\sqrt{2}/4$	1/4
S/N increase (n=2)[c]	1	$\sqrt{2}$[d]	1	$\sqrt{2}/2$	1/2
S/N increase (n=4)[c]	1	$\sqrt{2}$	2[d]	$\sqrt{2}$	1
S/N increase (n=8)[c]	1	$\sqrt{2}$	2	$2\sqrt{2}$[d]	2
S/N increase (n=16)[c]	1	$\sqrt{2}$	2	$2\sqrt{2}$	4[d]

[a]Spectra A through D are harmonically summed as described in Section 2.6.2.

[b]Factor of signal increase for harmonic n. Equal signal strengths are assumed for all n in the original spectrum.

[c]Factor of S/N increase for harmonic n.

[d]Indicates the maximum S/N increase for this harmonic n in any of the spectra.

the curves are due to the software high-pass filtering. At 5 s, which is $P_{\rm max}$ in the calculation, a large increase in the minimum detectable flux density is seen since only harmonics are considered in the calculation at periods greater than this. The reduced sensitivity of the survey at large periods is an important selection effect.

2.6.3 Check of Survey Sensitivity Calculation

We have used independently estimated flux densities obtained from pulsar-gated radio imaging with the Australia Telescope Compact Array (ATCA) (see Chapter 5) to check the PM Survey sensitivity calculation. Flux densities were measured for seven pulsars.

For each pulsar, we used the detection S/N in the Fourier spectrum from survey observations taken at Parkes at 1374 MHz to estimate a flux density. The P and DM of the pulsar (which determine the minimum detectable flux density for the pulsar in the sensitivity calculation) were used to convert the detection S/N into a flux density estimate. The pulsar in each case was not exactly at the beam center, so a correction to the S/N was applied assuming a half-power beam radius of $7.5' \pm 0.5'$. This uncertainty accounts for shape variations in the different beams and provides an uncertainty in the estimated flux density value. Table 2-5 lists the values obtained from the sensitivity calculation and the values estimated from the ATCA pulsar gating for comparison.

In all but two cases the values derived from the two methods are consistent; PSRs J0940−5428 and J1112−6103 show significant discrepancies. The ATCA flux density for PSR J0940−5428 may be an underestimate given that the 2.5-GHz ATCA value (Table 5-3) is larger than the 1.4-GHz value, which is not expected for a non-thermal radio source (e.g., a pulsar). This would account for the positive spectral index α measured for the pulsar. PSR J1112−6103 was weakly detected in the 16-bin profile obtained from gating. The ATCA array configuration used in the gating (1.5A) also had poorer spatial resolution than the 6D array, which was used for the other pulsars in the sample (Table 5-1). In this case, the ATCA flux density could have a significantly underestimated flux density and uncertainty in the fitted value. If either

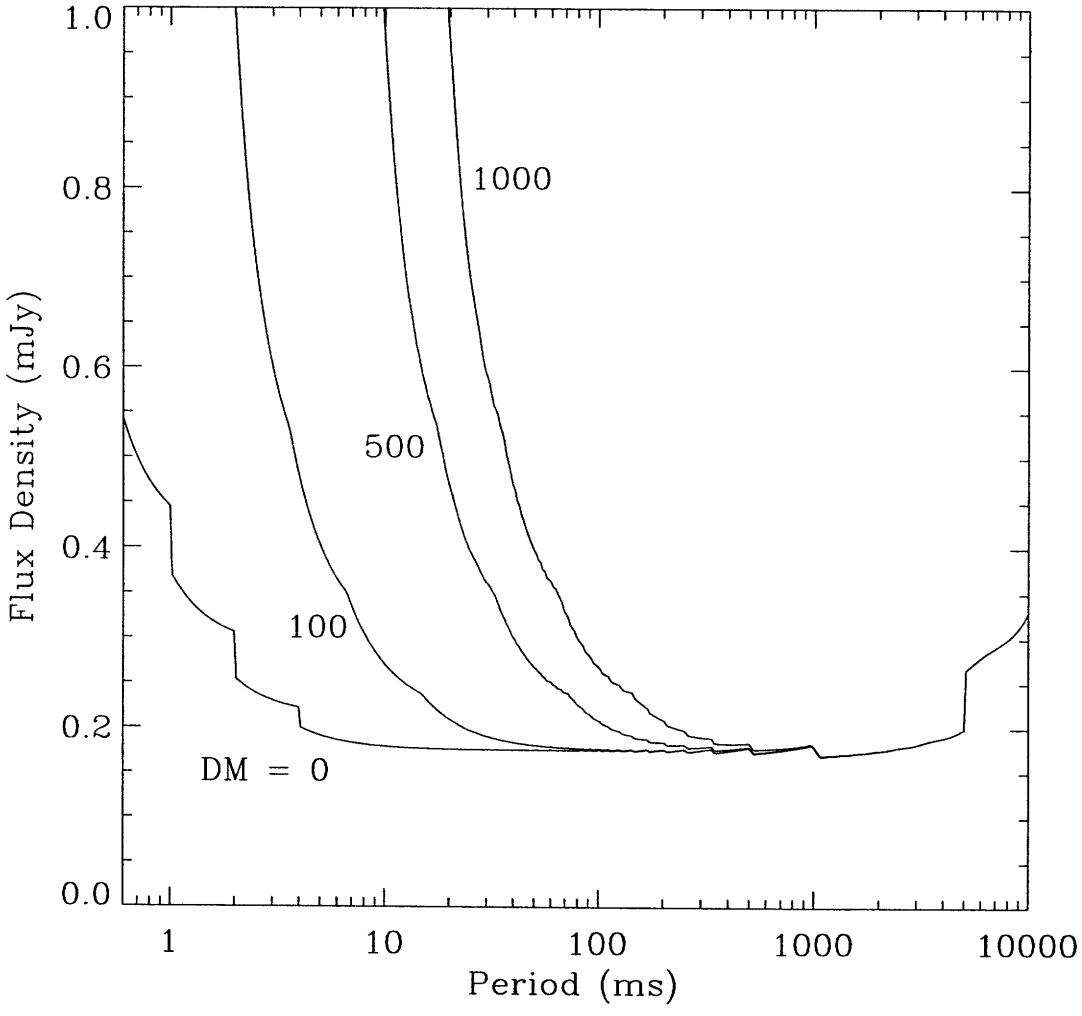

Figure 2-4 PM Survey sensitivity curves for DMs of 0, 100, 500, and 1000 cm^{-3}. A 5% intrinsic pulsed duty cycle is assumed in each case. Features in the curves are described in the text.

of these is true, then the discrepancy in the flux densities may not be as significant as it appears. The other five pulsars in the sample have consistent flux density estimates, including PSR J1420−6048, which probes the sensitivity model with its short period and large DM.

Given the presence of RFI, scintillation effects, variable pulse profile morphology in the sample, and variability in the system temperature during the observations, it is not surprising that there are some differences in the derived flux densities. We conclude that the sensitivity model is adequately accounting for the survey effects which can be modeled.

2.7 Results to Date

The PM Survey is still in progress, and therefore the full array of scientific results and the major conclusions from the survey are to be presented in the future. However, the findings of the survey to date are summarized below.

2.7.1 New Pulsar Discoveries

To date, almost 2100 of the 2670 total expected pointings in the survey area ($\sim 80\%$) have been observed and processed. From these data, we have confirmed 569 new pulsars (of which about 1/3 were found in the data processed at MIT) and redetected 214 previously known pulsars in the survey area (Table 2-1). New pulsars and their parameters are made public after follow-up timing has been completed. Of the 569 new pulsars found so far, 187 (including 6 new binaries) have had timing observations completed and have been made public.[3] These also appear in detail elsewhere in the literature (Camilo et al. 2000; Lyne et al. 2000; Manchester et al. 2000). Table 2-6 lists the names of these 187 pulsars. Radio imaging was conducted on seven of the 187 pulsars which are young in order to determine accurate positions for timing solutions. This imaging follow-up work is described in Chapter 5. Figure 2-5 shows

[3]http://www.atnf.csiro.au/research/pulsar/psr/pmsurv/pmwww/pmpsrs.db.

a P-$\dot{P}$ diagram for these 187 new discoveries, with binary pulsars and pulsars which have been imaged indicated as such. 39 of the 187 pulsars listed were timed as part of this thesis work and are presented in more detail in Chapter 4.

2.7.2 Young Pulsars

A number of pulsars have been discovered in the PM Survey which have been confirmed as young. Pulsars suspected to be young due to a large initial $\dot{P}$ estimate were timed for a year to confirm their age and establish other timing parameters. Table 2-7 lists the physical parameters for the 12 new pulsars discovered to date in the PM Survey with characteristic age $\tau_c < 100$ kyr. This brings the total number of such pulsars known to 38. For 7 of these 12 new young pulsars, radio imaging positions were determined which were used to facilitate timing solutions.

2.7.3 PSR J1119−6127: a Young High-Magnetic-Field Pulsar

Of the many pulsars found in the PM Survey to date, one pulsar in particular, PSR J1119−6127, has proved to be very interesting and is the subject of further study in this thesis (Chapters 5 and 6). PSR J1119−6127 was discovered on 23 August 1997 in a standard 35-min survey observation of the PM Survey. Follow-up regular timing observations were then carried out at Parkes starting 1998 February. Observing and analysis details for the timing effort are presented elsewhere (Camilo et al. 2000). An integrated 1374-MHz pulse profile for PSR J1119−6127 is shown in Figure 2-6.

PSR J1119−6127 has the highest $\dot{P}$ yet measured for any radio pulsar, indicating a very young age ($\tau_c \sim 1.6$ kyr). This pulsar also has an unusually large period ($P = 408$ ms) for such a young pulsar. Since $\dot{P}$ correlates highly with timing noise (Arzoumanian et al. 1994), which can affect the astrometric parameters determined from the timing data, we undertook pulsar-gated radio interferometric observations of PSR J1119−6127 in order to determine an accurate position for the pulsar (see Chapter 5 for details). This position was then used in the timing solution to fit for

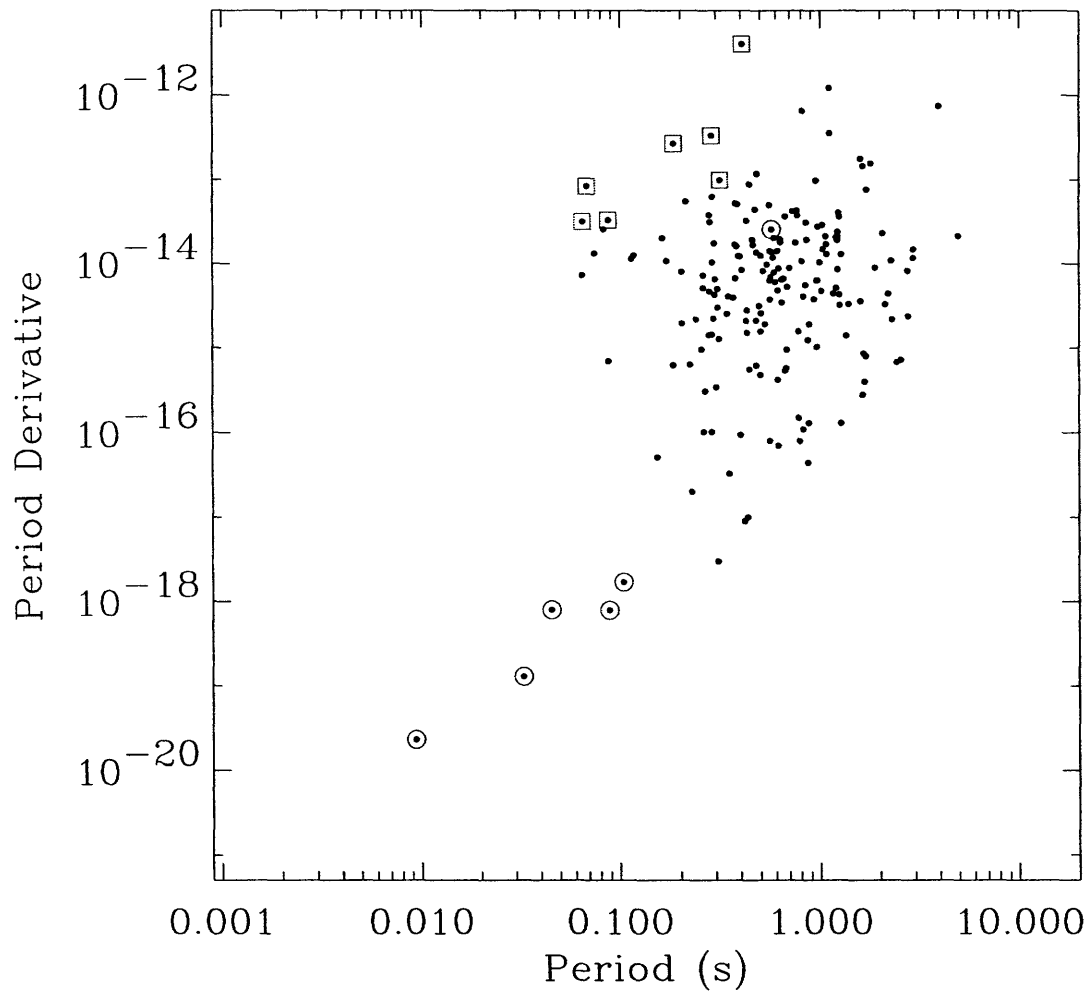

Figure 2-5 P-$\dot{P}$ diagram for new PM Survey discoveries which have had complete timing solutions determined and which have been made public (see Table 2-6). Binary pulsars are indicated by circles, and young pulsars which have had a position determined from radio imaging are indicated by squares. Two of the new PM pulsars have a negative measured $\dot{P}$ (consistent with zero) and are not plotted here.

Table 2-4. Parameters for PM Survey Sensitivity Calculation

Parameter	Value
Digitization Loss Constant (σ)	1.5
S/N Detection threshold (β)	8
Gain (G)	1.7 Jy/K
System Temperature ($T_{\rm sys}$)	21 K
Center Frequency (ν)	1374 MHz
Integration Time per Pointing ($t_{\rm int}$)	2100 s
Bandwidth (B)	288 MHz
Number of Frequency Channels	96
Frequency Channel Width ($\Delta\nu$)	3 MHz
Number of Polarizations (N_p)	2
Sample Time ($t_{\rm samp}$)	0.25 ms
FWHM Duty Cycle (W/P)	5%
Hardware High-pass Time Constant (τ_H)	2 s
Software High-pass Time Constant (τ_S)	2.048 s

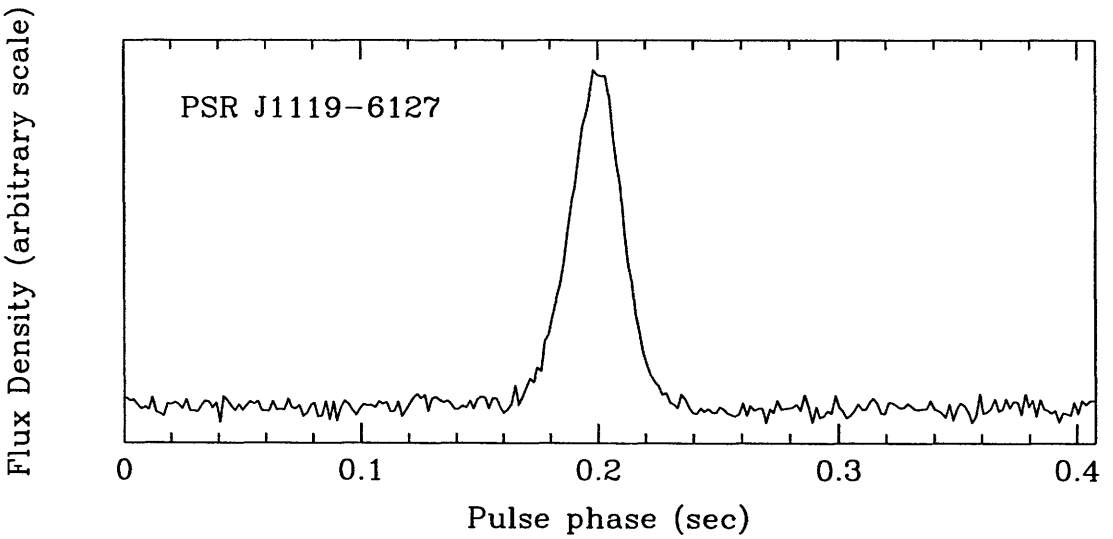

Figure 2-6 Integrated 1374-MHz pulse profile for PSR J1119−6127, a young high-magnetic-field pulsar discovered in the PM Survey.

Table 2-5. Comparison of Flux Densities for Seven Pulsars

PSR	P (s)	DM (pc cm^{-3})	S_{1374}[a] (mJy)	S_{1384}[b] (mJy)	σ[c]
J0940−5428	0.088	136	1.3(2)	0.66(4)	3.1
J1112−6103	0.065	597	1.6(2)	0.54(13)	4.4
J1119−6127	0.408	707	1.3(2)	1.02(7)	1.3
J1301−6305	0.185	374	0.5(2)	0.47(9)	0.1
J1412−6145	0.315	514	0.8(1)	0.6(3)[d]	0.6
J1413−6141	0.286	676	0.9(2)	0.8(4)[d]	0.2
J1420−6048	0.068	362	1.2(2)	1.09(8)	0.5

Figures in parentheses represent 1σ uncertainties in the least-significant digit quoted.

[a]1374-MHz flux density, estimated from detection strengths in Parkes survey observations and scaled using the PM Survey model sensitivity.

[b]1384-MHz flux density, estimated from ATCA pulsar gating (Chapter 5).

[c]Discrepancy in the flux density values. The different frequencies for the two flux density estimates introduces a small difference ($\sim 1\%$) in the comparison.

[d]No pulsar gating used. Flux density obtained from point-source flux density in map.

Table 2-6. 187 New PM Survey Pulsars

PSR	PSR	PSR	PSR	PSR	PSR
J0831−4406	J1144−6146	J1354−6249[c]	J1540−5736	J1649−4349	J1737−3101
J0835−3707	J1144−6217	J1403−6310[c]	J1543−5459	J1649−4653	J1739−3023
J0838−3947	J1152−6012	J1406−6121[c]	J1546−5302	J1649−4729	J1739−3049
J0855−4644	J1216−6223	J1407−6048[c]	J1548−5607	J1650−4341	J1739−3159
J0855−4658	J1220−6318	J1407−6153[c]	J1550−5242	J1650−4502	J1740−3052[b]
J0901−4624	J1224−6208	J1412−6111[c]	J1556−5358	J1651−4519	J1741−2945
J0922−4949	J1231−6303	J1412−6145[a,c]	J1558−5419	J1653−4249	J1741−3016
J0940−5428[a]	J1232−6501[b]	J1413−6141[a,c]	J1601−5244	J1653−4315	J1744−3130
J0954−5430	J1233−6312	J1413−6222[c]	J1601−5335	J1654−4140	J1747−2802
J0957−5432	J1245−6238	J1416−6037[c]	J1605−5215	J1702−4217	J1752−2821
J1000−5149	J1249−6507	J1418−5945[c]	J1607−5140	J1702−4428	J1758−2630
J1001−5559	J1252−6314	J1420−6048[a,c]	J1609−5158	J1705−3936	J1759−2304
J1002−5559	J1254−6150	J1424−5822[c]	J1610−5006	J1708−3827	J1759−2307
J1013−5934	J1301−6305[a,c]	J1425−6210[c]	J1611−4949	J1709−3841	J1805−2033
J1016−5819	J1302−6313[c]	J1429−5935[c]	J1613−5211	J1710−4148	J1806−2125
J1019−5749	J1303−6305[c]	J1434−6006[c]	J1613−5234	J1713−3844	J1809−1917
J1020−5921	J1305−6203[c]	J1434−6029[c]	J1616−5109	J1715−3700	J1810−1820
J1022−5813	J1305−6256[c]	J1435−6100[b]	J1616−5208	J1715−3903	J1810−2005[b]
J1043−6116	J1307−6318[c]	J1444−5941[c]	J1621−5039	J1716−3720	J1811−1736[b]
J1049−5833	J1309−6415[c]	J1452−5851[c]	J1622−4802	J1717−3737	J1811−1835
J1054−5943	J1312−6400[c]	J1454−5846[b]	J1622−4944	J1717−4043	J1812−2102
J1056−5709	J1314−6101[c]	J1457−5902[c]	J1623−4949	J1718−3825	J1813−2112
J1107−6143	J1317−6302[c]	J1502−5828	J1625−4904	J1720−3659	J1814−1649
J1112−6103[a]	J1322−6241[c]	J1511−5835	J1626−4807	J1723−3659	J1814−1744
J1115−6052	J1324−6146[c]	J1513−5739	J1628−4804	J1724−3505	J1815−1909
J1117−6154	J1327−6400[c]	J1522−5525	J1630−4719	J1725−3546	J1823−1807
J1119−6127[a]	J1341−6023[c]	J1524−5706	J1632−4621	J1725−3848	J1913+1145
J1123−6102	J1344−6059[c]	J1529−5611	J1632−4818	J1726−3530	
J1124−6421	J1345−6115[c]	J1530−5327	J1635−4513	J1726−3635	
J1130−5925	J1347−5947[c]	J1536−5433	J1636−4803	J1728−3733	
J1138−6207	J1348−6307[c]	J1537−5645	J1636−4933	J1733−3322	
J1142−6230	J1349−6130[c]	J1538−5438	J1637−4721	J1736−3511	

[a]Radio imaging used to determine position for timing solution (Chapter 5).

[c]Timing parameters obtained as part of this thesis work (Chapter 4).

[b]Binary pulsar.

Table 2-7. Physical Parameters of New PM Survey Pulsars with $\tau_c < 100$ kyr

PSR	P (s)	τ_c[a] (kyr)	$\log B$[b] (G)	$\log \dot{E}$[c] (erg s^{-1})
J1119−6127[d]	0.408	1.61	13.61	36.36
J1301−6305[d]	0.185	11.0	12.85	36.23
J1420−6048[d]	0.068	13.0	12.38	37.03
J1413−6141[d]	0.286	13.6	13.00	35.76
J1112−6103[d]	0.065	32.7	12.18	36.66
J0940−5428[d]	0.088	42.2	12.23	36.30
J1412−6145[d]	0.315	50.6	12.75	35.08
J1809−1917	0.083	51.3	12.18	36.26
J1406−6121	0.213	61.7	12.53	35.34
J0901−4624	0.442	80.0	12.80	34.60
J1814−1744	3.976	84.7	13.74	32.67
J1718−3825	0.075	89.5	12.00	36.11

Entries ranked by characteristic age.

[a]Characteristic age.

[b]Surface magnetic field.

[c]Spin-down luminosity.

[d]Radio imaging used to determine position for timing solution (Chapter 5).

the spin parameters f, $\dot{f}$, and $\ddot{f}$, where $f \equiv 1/P$ is the rotational frequency of the pulsar.

Partly for the reason that it has such a large $\dot{P}$, a stationary $\ddot{f}$ could be measured with a phase-connected timing solution (i.e., through absolute pulse numbering). This is only the second pulsar for which this has been possible using this method, after PSR J1513−5908 (B1509−58) (Kaspi et al. 1994b). The resulting value of the braking index n, determined according to

$$n = \frac{f\ddot{f}}{\dot{f}^2}, \tag{2.34}$$

is $n = 2.91 \pm 0.05$, where the uncertainty includes possible contamination by timing noise.

For the four other pulsars for which n has been measured, the Crab, PSR J0540−6919 (B0540−69), PSR J1513−5908, and the Vela pulsar, n ranges between 1.4 and 2.8 (see Table 1 of Melatos 1997). Observed braking indices smaller than 3 can be explained in a variety of ways, including a kinetic energy-dominated flow at the light cylinder, or an increase in the magnetic moment of the star over time (Blandford & Romani 1988). However, none of these scenarios is consistent with all observations (Arons 1992).

Assuming $P_0 \ll P$, but using the measured values of P, $\dot{P}$, and n (Camilo et al. 2000), the age of PSR J1119−6127 is $\tau = 1.7 \pm 0.1$ kyr, including possible biases due to timing noise and glitches. Of course, if the pulsar were born spinning more slowly, it would be younger than this. If $P_0 = 200$ ms, half the present period, the pulsar's age would be $\tau = 1.2$ kyr (Equation 1.11). In any case, it is clear that PSR J1119−6127 is among the very youngest pulsars known (Table 2-7).

Aside from its young age, this pulsar also has a very strong surface magnetic field. The magnetic field derived from timing parameters implies $B = 4.1 \times 10^{13}$ G. At the time of its discovery, PSR J1119−6127 had the highest magnetic field yet observed for any radio pulsar. Previously, the largest value was $B = 2.1 \times 10^{13}$ G for PSR J0157+6212 (B0154+61) (Arzoumanian et al. 1994). Another pulsar, PSR

J1814−1744, has since been discovered in the PM Survey with a higher magnetic field, $B = 5.5 \times 10^{13}$ G. This pulsar is discussed elsewhere (Camilo et al. 2000).

PSR J1119−6127 is one of the youngest pulsars known and is a good candidate to have an associated supernova remnant (SNR) or pulsar wind nebula (PWN), both of which are seen around other young pulsars. A detailed follow-up radio imaging study was completed on PSR J1119−6127 in order to establish a positional certainty for the pulsar (necessary for the timing solution) and to look for a SNR and a radio nebula powered by the pulsar wind. Results from the radio imaging follow-up work on PSR J1119−6127 are presented in Chapters 5 and 6.

Chapter 3

Pulsars in the Magellanic Clouds

This chapter is a modified self-contained paper titled, "Pulsars in the Magellanic Clouds," to be submitted for publication in the *Astrophysical Journal* (Crawford et al. 2000b).

We report the results of a survey for radio pulsars in the Small Magellanic Cloud (SMC) conducted with the 20-cm multibeam receiver of the Parkes 64-meter telescope. This survey targeted a more complete region of the SMC than a previous pulsar search and had an improvement in sensitivity of a factor of about two for most pulsar periods. Our survey is much more sensitive to fast young pulsars (with $P \lesssim 100$ ms) and is the first survey of the SMC with any sensitivity to millisecond pulsars. Two new pulsars were discovered in the survey, one of which is located within the SMC. The number of pulsars found in the survey is consistent with the expected number derived using several methods. The age distribution of luminous Magellanic Cloud pulsars supports the conjecture that pulsars younger than about 5 Myr are preferentially more luminous than older pulsars. We also report the serendipitous discovery of a new pulsar in the 30 Doradus region of the Large Magellanic Cloud (LMC) and report refined timing results for three previously known LMC radio pulsars as well as timing results for our new discoveries. Our results bring the total number of rotation-powered pulsars currently known in the Magellanic Clouds to eight.

3.1 Introduction

The Magellanic Clouds contain the most distant population of detectable pulsars observable with current technology. Since the distances to the Magellanic Clouds are large, only the most luminous pulsars are detectable. However, despite the small number of pulsars currently known, these pulsars have proved to be among the most interesting in the entire pulsar population. Of the eight pulsars discovered to date, one is in an unusual binary system and two are younger than 10 kyr. For comparison, of over 700 Galactic pulsars discovered and cataloged to date, only one is in a similar binary system, and only five Galactic pulsars are younger than 10 kyr.

Surveying the Magellanic Clouds for radio pulsars is difficult due to the large surface area to be covered and their large distances. Long integrations using a telescope with a large collecting area are needed to detect even their most luminous pulsars. With its southern latitude, the Parkes 64-meter radio telescope[1] in Parkes, NSW, Australia is the most appropriate telescope for conducting such searches for pulsars.

The difficulty of obtaining sufficient sensitivity has been somewhat alleviated by the recent installation of the 20-cm multibeam receiver at Parkes (Staveley-Smith et al. 1996). This receiver is simultaneously sensitive to 13 distinct locations on the sky which can be interleaved in separate pointings to give complete and efficient spatial coverage of large regions. The Parkes Multibeam Pulsar Survey (PM Survey), described in Chapter 2, is currently using this receiver to search for pulsars in the Galactic plane. The fact that the PM Survey has discovered 569 new pulsars to date with only 80% of the survey completed demonstrates that the multibeam system is capable of finding faint pulsars and is an appropriate instrument to search for pulsars in the Magellanic Clouds.

In this chapter we report the results of a survey for pulsars in the Small Magellanic Cloud (SMC). Below we describe a previous survey, the observations and data reduction procedure for our survey, and subsequent timing observations. We discuss

[1]http://www.parkes.atnf.csiro.au. The Parkes Observatory is part of the Australia Telescope, which is funded by the Commonwealth of Australia for operation as a National Facility managed by CSIRO.

our survey results and summarize the currently known Magellanic Cloud pulsar population. We also discuss implications for pulsar luminosity models and the estimated number of detectable pulsars derived using several methods.

3.2 Previous Magellanic Cloud Pulsar Survey Work

Only one full-scale pulsar survey of the Magellanic Clouds has been conducted previously. McConnell et al. (1991) searched for pulsars using Parkes at a wavelength of 50 cm. This survey effort was split into three phases with different observing parameters used for each phase of the survey. Although the region surveyed in each phase is not described, the third phase of the survey was used for five of the seven years of the observing effort, and we use this phase for a sensitivity comparison with our survey. This phase of their survey used a center frequency of 610 MHz with a total bandwidth of 60 MHz split into 24 channels. The sampling time was 5 ms with a 5000 s integration time per pointing and had sensitivity to two orthogonal polarizations.

In their data reduction procedure, McConnell et al. (1991) report that they assumed a dispersion measure (DM) of 100 pc cm^{-3} in an initial sub-band dedispersion in their analysis. Magellanic Cloud pulsars found to date have DMs which are roughly centered on this value, but the observed DM range is about 70 pc cm^{-3} to 150 pc cm^{-3}. Thus, their sensitivity to pulsars with DMs far from 100 pc cm^{-3} was reduced and some pulsars may have been missed in their survey. The McConnell et al. (1991) survey also targeted the optical bar and the southern and western parts of the SMC (see Figure 1 of McConnell et al. 1991). We have used a map of the IRAS 60-μm emission[2] as a guide for the boundaries of the SMC to survey, and hence we have more complete coverage in the northern and eastern regions of the SMC. McConnell et al. (1991) reported the discovery of four pulsars, three in the Large Magellanic Cloud (LMC) and one in the SMC.

[2]http://www.ipac.caltech.edu.

3.3 Observations and Data Reduction

3.3.1 Survey Observations and Data Reduction

The multibeam receiver is capable of simultaneously observing 13 separate locations on the sky and has been designed to interleave pointings in such a way that clusters can be formed from each set of four pointings, thereby offering efficient and complete sky coverage (Staveley-Smith et al. 1996). System and observing details can be found elsewhere in descriptions of the Parkes Multibeam Pulsar Survey (Lyne et al. 2000; Manchester et al. 2000; see also Chapter 2). The receiver for each beam is a dual-channel cryogenically cooled system sensitive to orthogonal linear polarizations. A 288-MHz bandwidth is centered on a frequency of 1374 MHz. Each beam has a full-width half-power diameter of $\sim 15'$ and a system noise temperature of 21 K (36 Jy) on cold sky. A filterbank system covering the 288-MHz bandwidth was used which has 96 separate 3-MHz channels for each polarization for each beam.

During observing, detected signals from each channel were square-law detected and added in polarization pairs before undergoing high-pass filtering. The signals were then one-bit digitized every 0.25 ms and recorded on magnetic tape (DLT) for processing and analysis. We observed a total of 12 pointings (156 separate beams) for 8400 s per pointing, corresponding to a limiting flux density sensitivity of ~ 0.08 mJy for most of the expected pulsar period range. Figure 3-1 illustrates the distribution of beams in our survey overlaid on an IRAS 60-μm image of the region in grayscale.

Processing was done by first reading the data for each beam from DLT tape to disk on Sun workstations. Each beam was then dedispersed at 191 trial DMs ranging from 0 to 442 pc cm^{-3}, encompassing the range of observed DMs for Magellanic Cloud pulsars. The 96 frequency channels for each DM trial were appropriately aligned, summed, and high-pass filtered in software before an amplitude spectrum was formed via a 2^{25}-point FFT. Portions of the spectrum (typically a few percent) were masked for each DM trial according to whether radio-frequency interference appeared significantly in the zero-DM spectrum.

The strongest candidates in each DM trial were recorded if they had a signal-

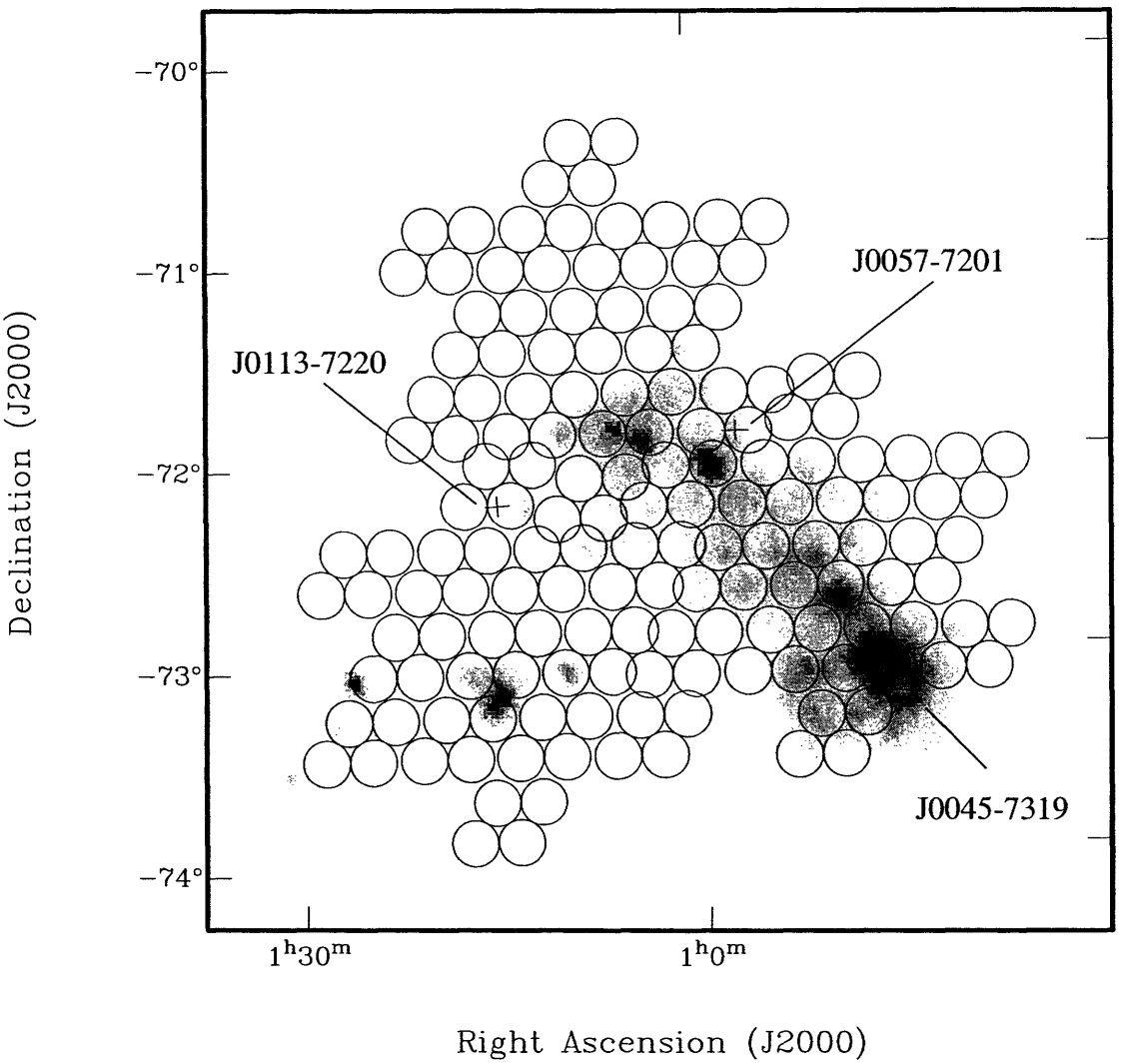

Figure 3-1 Multibeam survey coverage of the SMC. Each circle represents the half-power beamwidth of a single beam of the receiver. A total of 12 pointings (156 beams) were interleaved for tiled coverage. IRAS 60-μm emission is indicated in grayscale and roughly defines our survey region. The locations of the three pulsars discovered in the direction of the SMC to date are indicated by crosses. PSR J0057−7201 is a foreground pulsar while the other two lie in the SMC.

to-noise ratio of at least 7 and appeared in at least 6 of the DM trials (in order to avoid an excess of spurious candidates). The original data were then reprocessed by dedispersing and folding the data at DMs and periods near the candidate DM and period. Follow-up confirmation observations were undertaken in the cases where the resulting folded data showed a pulsar-like signature.

The relatively high frequency of the multibeam receiver compared to the lower frequency used in the McConnell et al. (1991) survey is an advantage since dispersive smearing and scattering are greatly reduced at this frequency, thereby allowing the detection of fast, distant, and highly scattered pulsars which may have been previously missed. However, the high observing frequency also has the drawback that pulsars are much fainter and longer integration times are required to achieve comparable sensitivity.

Since our survey was conducted at a different frequency than the McConnell et al. (1991) survey, we must scale the sensitivity of each survey in order to compare them. We have scaled each survey to a 400-MHz luminosity (L_{400}), assuming a distance to the SMC of 57 kpc (Cole 1998) and a typical pulsar spectral index $\alpha = -1.6$ in each case (Lorimer et al. 1995), where α is defined according to $S \sim \nu^{\alpha}$. Figure 3-2 shows a comparison of the sensitivity of the two surveys for a variety of pulsar periods and DMs. Our survey is significantly more sensitive to fast young pulsars (with $P \lesssim 100$ ms) and is the first survey of the SMC which has any sensitivity to millisecond pulsars.

3.3.2 Timing Observations and Data Reduction

New pulsars discovered in our survey were timed regularly for about a year following their discovery. The observing system used for timing these pulsars at Parkes is identical to that used in the survey with the exception that we only record data from the center beam of the multibeam receiver and made several additional timing observations at 70 cm. The start time of each observation was recorded and was synchronized with an observatory time standard, and data were typically recorded on Exabyte tape. Frequency channels in the recorded data were delayed by an amount

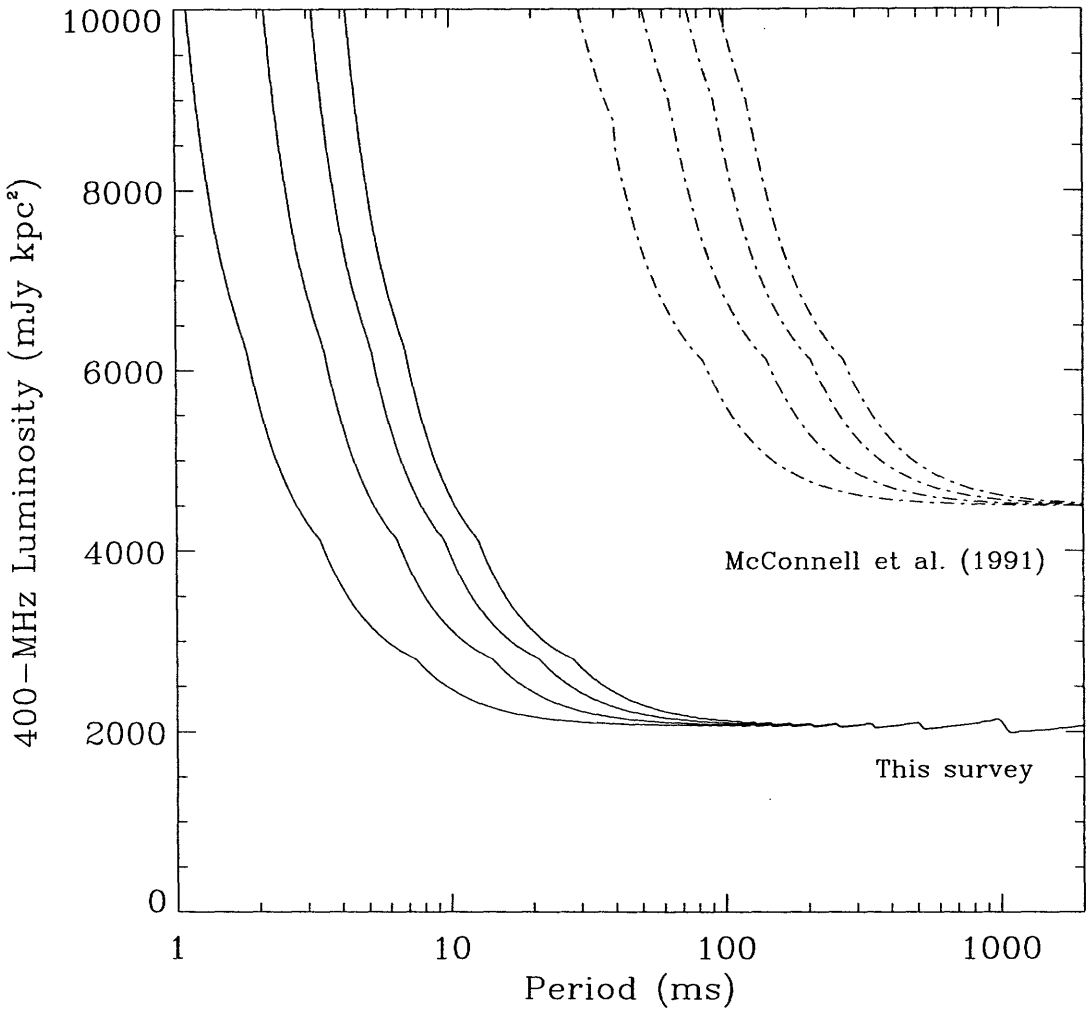

Figure 3-2 Sensitivity to SMC pulsars as a function of pulsar period for our survey (solid line) and for the McConnell et al. (1991) survey (dashed-dotted line). A 5% pulsed duty cycle is assumed in each case. The two surveys were conducted at different radio frequencies, so the sensitivity has been scaled to a minimum detectable 400-MHz luminosity assuming a standard pulsar spectral index ($\alpha = -1.6$) and an SMC distance of 57 kpc. Curves for DM values of 50, 100, 150, and 200 pc cm^{-3} are shown (from left to right) for each survey, roughly corresponding to the range of DM values for known pulsars in the Magellanic Clouds. The sensitivity calculation used here follows the one for the PM Survey described in detail in Chapter 2.

proportional to the DM and summed. The resulting time series was then folded at the topocentric rotation period of the pulsar, generating a single pulse profile for each observation. A topocentric pulse time-of-arrival (TOA) was then measured for each timing observation by cross-correlating the pulse profile with a high signal-to-noise template profile. Spin and astrometric parameters were then determined using the TEMPO software package,[3] and the JPL DE200 planetary ephemeris (Standish 1990). The TEMPO package converts each TOA to the solar system barycenter and refines the estimated spin and astrometric parameters by minimizing the residual differences between measured and model TOAs over the span of observations. Timing data for three known pulsars in the LMC were previously obtained at several observing frequencies at Parkes with an observing system described elsewhere (Kaspi 1994; Johnston et al. 1995). These data were reprocessed with a later version of TEMPO in the manner described above to obtain refined timing parameters.

3.4 Results

We have discovered two new pulsars in our SMC survey. One pulsar, PSR J0057−7201, has a significantly smaller DM than the population of known Magellanic Cloud pulsars, and therefore we believe it is a foreground object. The other new pulsar, PSR J0113−7220, has a DM larger than the only previously discovered SMC pulsar, PSR J0045−7319, indicating that it is located within the SMC. This brings the number of known SMC pulsars to two.

As part of an ongoing campaign to search for radio pulsations from X-ray targets in the LMC, such as the X-ray pulsar PSR J0537−6910 (Marshall et al. 1998), we have serendipitously discovered one new LMC pulsar, PSR J0535−6935, in one of the outlying beams of the multibeam receiver. Integrated 1374-MHz profiles for the three newly discovered radio pulsars are shown in Figure 3-3. 1374 MHz flux densities for these pulsars were estimated from the detection strengths in the discovery observations.

[3] http://pulsar.princeton.edu/tempo.

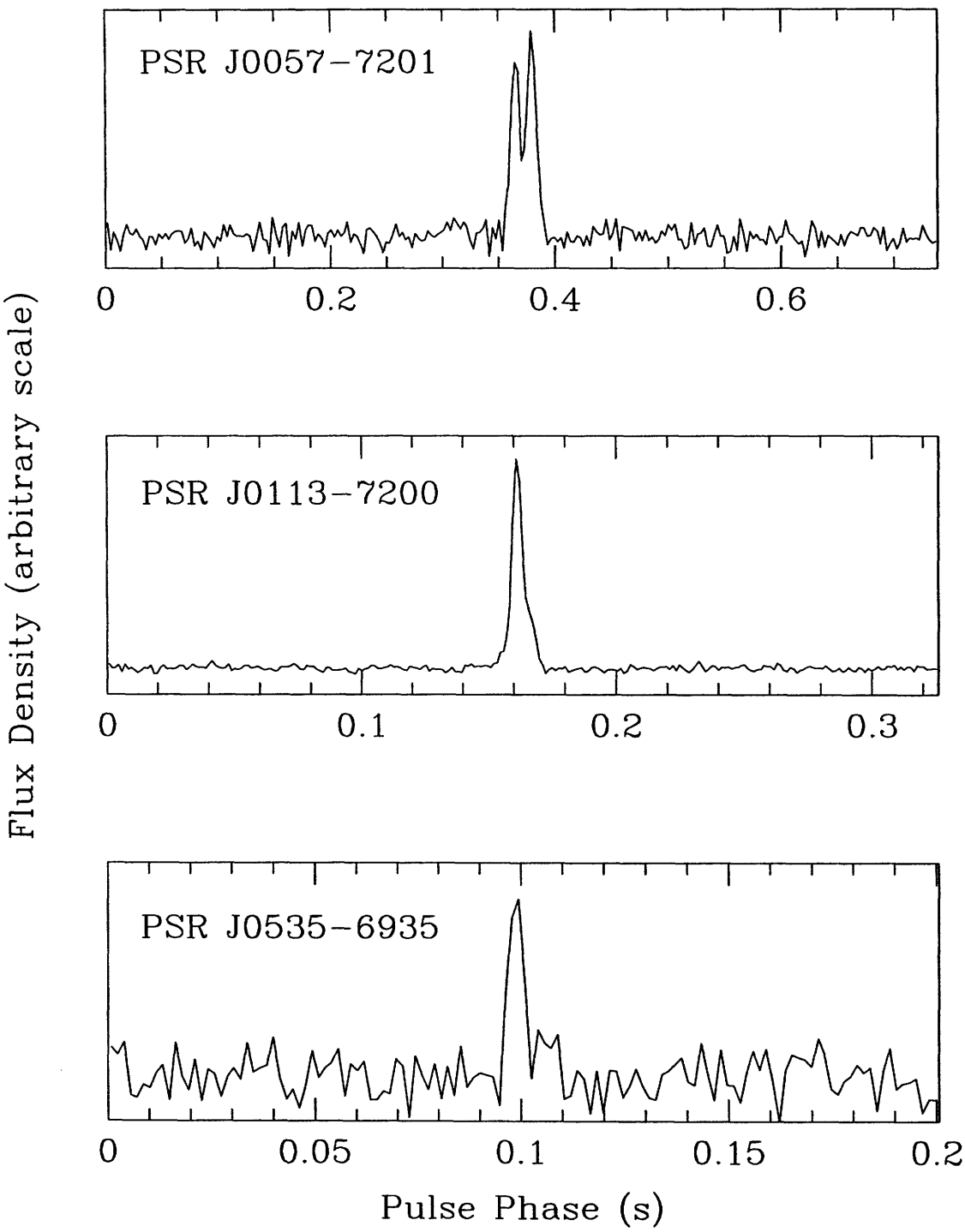

Figure 3-3 1374-MHz integrated total intensity profiles for PSRs J0057−7201, J0113−7220, and J0535−6935, the three newly discovered radio pulsars reported here.

Below we briefly describe and summarize each of the previously known pulsars in the Magellanic Clouds and the new pulsars discovered in this survey. A summary of the general characteristics of the eight currently known pulsars in the Magellanic Clouds is presented in Table 3-1.

3.4.1 PSR J0045−7319

PSR J0045−7319 was discovered in the SMC in the previous survey of the region by McConnell et al. (1991). It was subsequently timed and found to be in a 51-day binary orbit around a B1 class V star with a mass of 9 $M_{\odot}$ (Kaspi et al. 1994a). Of over 700 pulsars discovered to date in our own Galaxy (Taylor, Manchester, & Lyne 1993),[4] only one other pulsar, PSR J1302−6350 (B1259−63), has been shown to be in a similar system (Johnston et al. 1992b). The large DM sin $|b|$ of the pulsar (Figure 3-4) and its location on the DM vs. $|b|$ diagram (Figure 3-5) both suggest that it is in the SMC. Confirmation of its location in the SMC was obtained with its association with its B star companion, which was known to be in the SMC.

We detected PSR J0045−7319 in several diagnostic observations in the survey. We notice an unusual broadband ($\gtrsim$ 300 MHz) effect at 20 cm in which nulling occurs on time-scales of tens of minutes. This cannot be accounted for by scintillation, which is expected to have smaller fluctuation bandwidths (Cordes, Weisberg, & Boriakoff 1985), and the pulsar does not turn on and off as abruptly as known nulling pulsars do. In some timing observations, the pulsar is not detectable at all at 20 cm. A detailed study of this behavior is beyond the scope of this chapter.

3.4.2 PSR J0057−7201

PSR J0057−7201 is a 738-ms pulsar that was discovered in our survey. From its DM of 27 pc cm^{-3}, which is significantly smaller than the lowest known DM for a suspected Magellanic Cloud pulsar (69 pc cm^{-3} for PSR J0502−6617), we conclude that it is

[4]The updated catalog containing entries for 706 pulsars can be found at http://pulsar.princeton.edu.

Table 3-1. Currently Known Magellanic Cloud Pulsars

PSR	Location	Radio?	X-ray?	Timing Ref.	Interesting Features
J0045−7319	SMC	Y	N	1	Binary with B star
J0113−7220	SMC	Y	N	2	
J0535−6935	LMC[a]	Y	N	2	
J0537−6910	LMC[a]	N	Y	3	Fastest young pulsar, nebula
J0540−6919	LMC[a]	Y	Y	4	Crab twin, nebula
J0455−6951	LMC	Y	N	2	
J0502−6617	LMC	Y	N	2	
J0529−6652	LMC	Y	N	2	

(1) Kaspi et al. (1994)

(2) This work

(3) Marshall et al. (1998)

(4) Manchester et al. (1993)

[a]Located in the 30 Doradus region of the LMC.

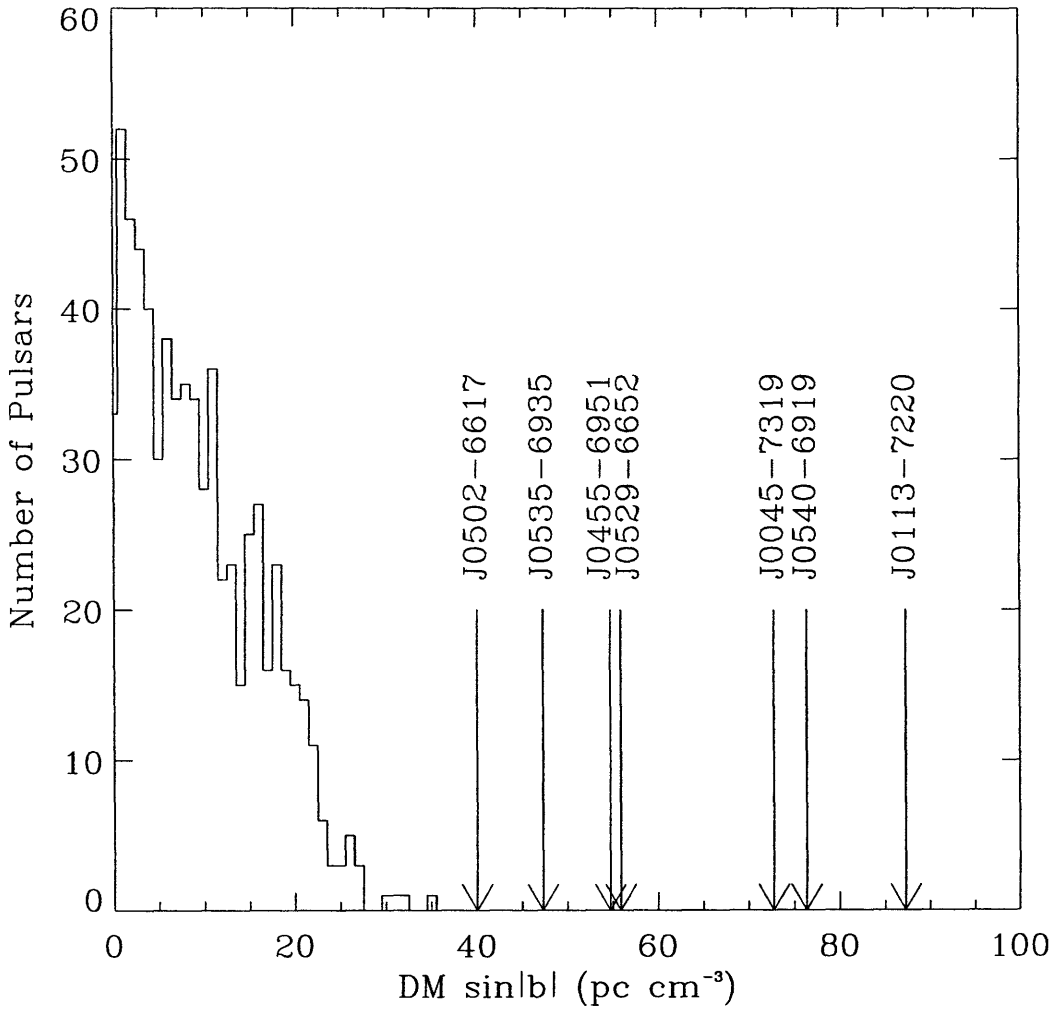

Figure 3-4 Histogram of DM $\sin|b|$ for 681 Galactic pulsars. Values of DM $\sin|b|$ for the seven Magellanic Cloud pulsars for which the DM has been measured are indicated by arrows.

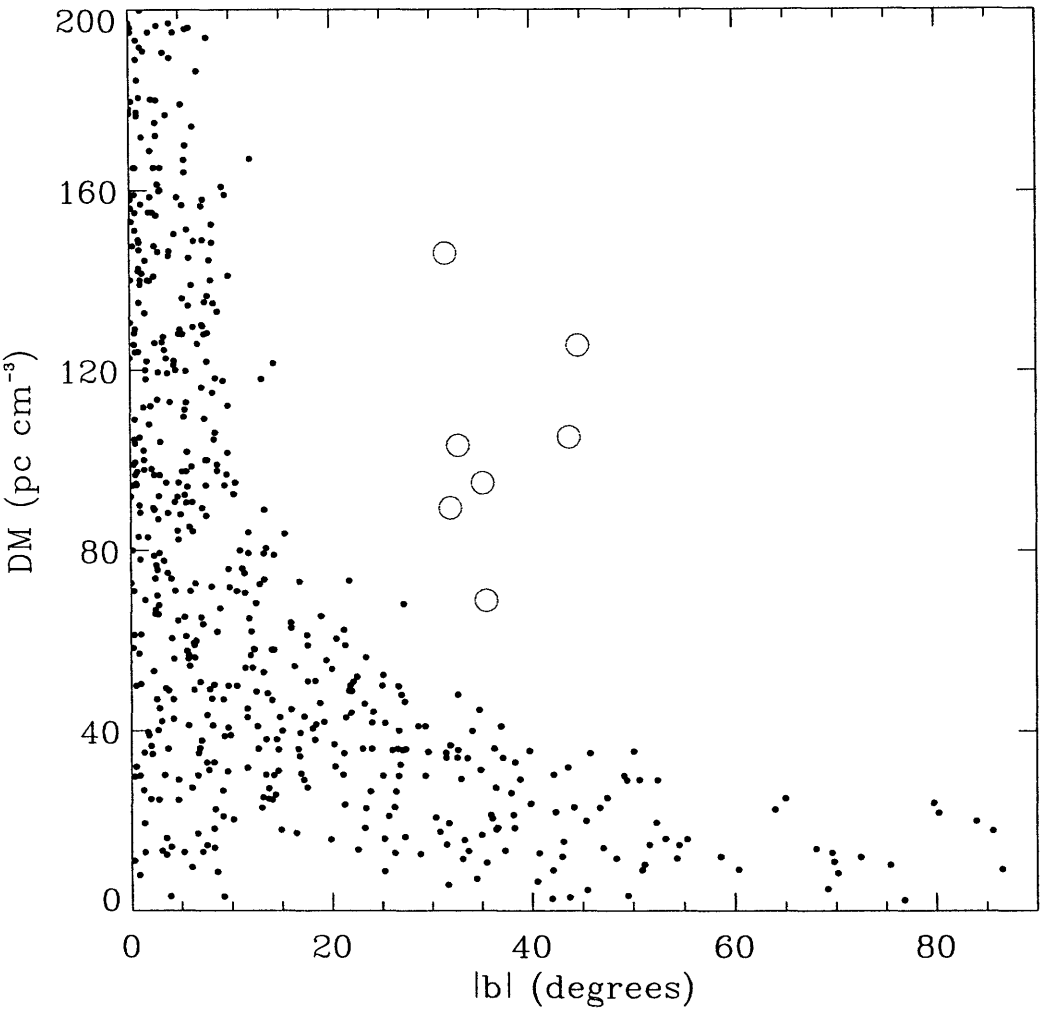

Figure 3-5 DM vs. $|b|$ for 681 Galactic pulsars (dots) and the seven Magellanic Cloud pulsars for which the DM has been measured (open circles). Galactic pulsars with DM > 200 pc cm^{-3} are off the scale of the plot.

a foreground object. The Taylor & Cordes (1993) DM-distance model indicates that the distance to PSR J0057−7201 is greater than 2.5 kpc, which is the limit of the Galactic plasma in the direction of this pulsar. However, the value of DM $\sin|b|$ for PSR J0057−7201 is 19 pc cm^{-3}, still well within the distribution of Galactic pulsars (Figure 3-4), and its location on the DM vs. $|b|$ diagram is also consistent with the Galactic distribution (Figure 3-5). Thus, despite that fact that it lies beyond the Galactic plasma layer, we cannot conclude that it is located within the SMC. The pulsar exhibits significant scintillation and was only detectable in about half of the 20-cm timing observations and in none of the 70-cm observations. Timing results for PSR J0057−7201 are presented in Table 3-2.

3.4.3 PSR J0113−7220

PSR J0113−7220 was first discovered in our SMC survey and has a 325-ms period. The pulsar shows no noticeable scintillation or nulling. Its DM of 125 pc cm^{-3} is larger than that of PSR J0045−7319, the only other known SMC pulsar, and implies that it is also located within the SMC. Radio timing results for PSR J0113−7220 (presented in Table 3-2) reveal a characteristic age of $\sim$ 1 Myr. PSR J0113−7220 is also very luminous with a narrow profile peak. It is the most luminous pulsar currently known in either of the Magellanic Clouds.

3.4.4 PSR J0535−6935

PSR J0535−6935 was discovered serendipitously in the 30 Doradus region of the LMC in one of the outlying beams of the multibeam receiver during a deep search for radio pulsations from PSR J0537−6910 with the center beam (Crawford et al. 1998). Figure 3-6 shows an 843-MHz radio image from the Sydney University Molonglo Sky Survey[5] of the 30 Doradus region, with the location of the three known pulsars in that region. PSR J0535−6935 proved too faint for regular timing, so an estimate of $\dot{P}$ was made by comparing the barycentric period in observations obtained one year

[5]http://www.astrop.physics.usyd.edu.au/SUMSS.

Table 3-2. Astrometric and Spin Parameters for Newly Discovered Pulsars

Name	J0057−7201	J0113−7220	J0535−6935
α (J2000)	$00^h57^m44^s.0(4)$	$01^h13^m11^s.09(3)$	$05^h35^m(2)$
δ (J2000)	$-72°01'19''(2)$	$-72°20'32''.20(15)$	$-69°35'(7)$
P (ms)	738.0624426(2)	325.88301613(1)	200.51011(2)
$\dot{P}$ ($\times 10^{-15}$)	0.10(8)	4.8590(15)	11.4(8)[a]
DM (pc cm^{-3})	27(5)	125.49(3)	89.4(8)
Epoch of Period (MJD)	51213.0	51212.0	51006.8
RMS residual (ms)	1.2	0.3	–
Number of TOAs	16/0/0	35/0/3	–
Timing span (days)	300	430	–
τ_c (Myr)[c]	~ 100	1.1	0.28
B ($\times 10^{12}$ G)[d]	~ 0.3	1.3	1.5
$\dot{E}$ (erg s^{-1})[e]	$\sim 10^{31}$	5.5×10^{33}	5.6×10^{34}
Notes	foreground	in SMC	in LMC

Figures in parentheses represent 1σ uncertainties in the least-significant digit quoted.

[a]Estimated by comparing the barycentric period in observations taken a year apart.

[b]Number of 20cm/50cm/70cm TOAs used.

[c]Characteristic age.

[d]Surface magnetic field.

[e]Spin-down luminosity.

apart. Table 3-2 lists the result. The positional uncertainty remains large ($\sim 7'$, the radius of the detection beam). The pulsar was detected in observations of length 21600 s and 17200 s and would have been too faint to detect in the standard 8400 s integrations of the SMC survey.

3.4.5 PSR J0537−6910

PSR J0537−6910 is a 16-ms X-ray pulsar in the 30 Doradus region of the LMC (Figure 3-6). This Crab-like pulsar was first detected in X-rays (Marshall et al. 1998) and is associated with the supernova remnant (SNR) nebula SNR 0538−69.1 (N157B) in the LMC. The pulsar has a characteristic age of ~ 5 kyr, making it the fastest young rotation-powered pulsar currently known and one of the few pulsars with a confirmed SNR association. Efforts to find a radio counterpart to this X-ray pulsar have so far been unsuccessful at both 50 cm and 20 cm (Crawford et al. 1998), but constraints on the radio luminosity are poor due to the large distance.

3.4.6 PSR J0540−6919

PSR J0540−6919 (B0540−69) is a 50-ms Crab-like pulsar in the 30 Doradus region of the LMC (Figure 3-6) which was first discovered in X-rays (Seward, Harnden, & Helfand 1984) and subsequently detected at radio wavelengths (Manchester et al. 1993). The pulsar is associated with SNR 0540−69.3 in the LMC and is very young, with a characteristic age of 1.7 kyr, making this system a twin of the Crab system. The measured DM of 146 pc cm^{-3} for PSR J0540−6919 is the largest yet measured for any pulsar in the Magellanic Clouds.

3.4.7 PSR J0455−6951, PSR J0502−6617, and PSR J0529−6652

These three pulsars were first discovered in the 50-cm survey of the Magellanic Clouds by McConnell et al. (1991) but were not subsequently timed by them. Timing results were first obtained by Kaspi (1994) but not published elsewhere. In Table 3-3 we present updated and refined timing results for these pulsars which we obtained by

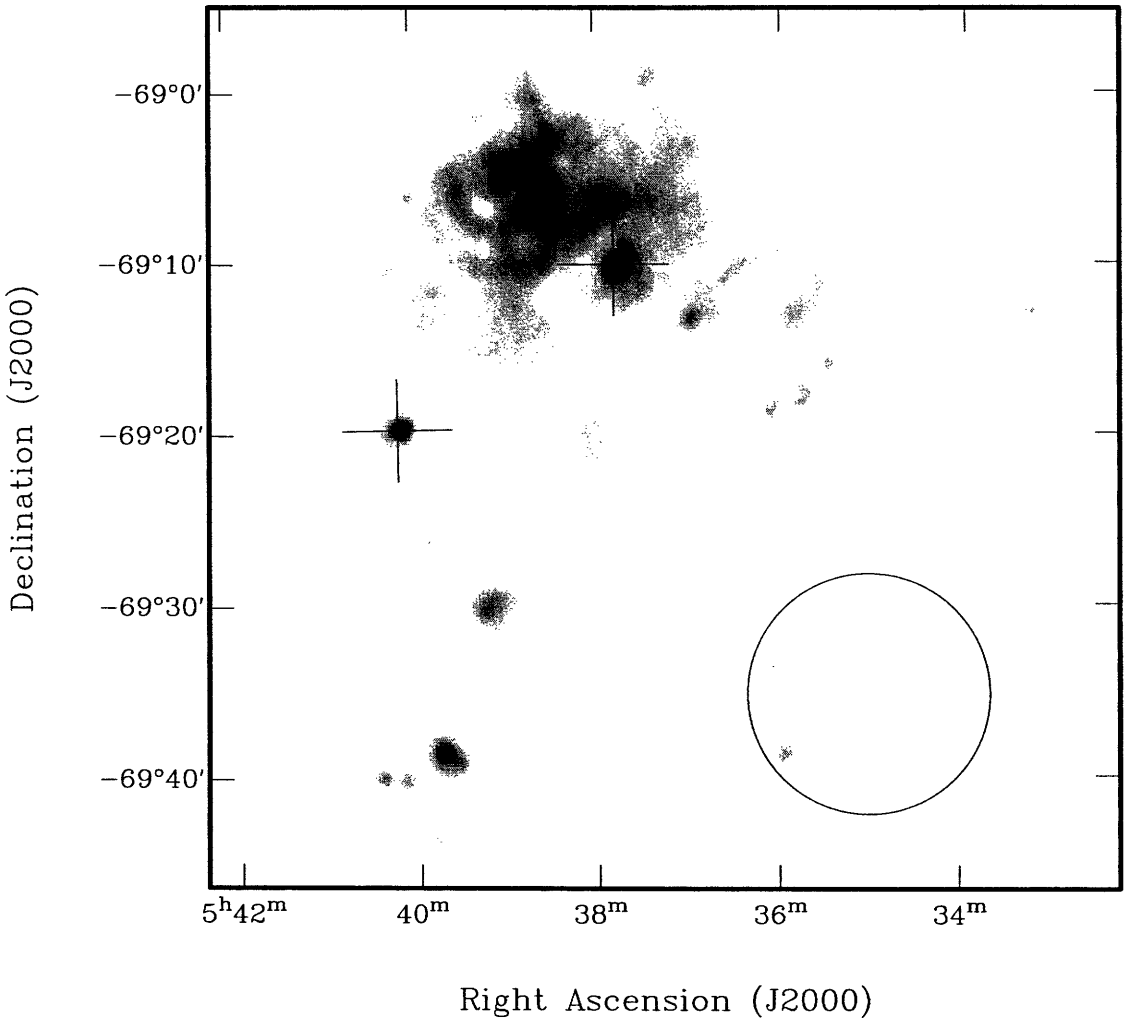

Figure 3-6 A Molonglo Observatory Synthesis Telescope 843 MHz image of the 30 Doradus region of the LMC. The two crosses indicate the positions of two young pulsars, PSR J0537−6910 (upper right) and PSR J0540−6919 (lower left), which are associated with the nebulae SNR 0538−69.1 (N157B) and SNR 0540−69.3 respectively. The discovery of PSR J0535−6935 in an outlying beam beam of the multibeam receiver during a search for radio pulsations from PSR J0537−6910 with the center beam is reported here; the error circle for this pulsar's location is shown. The faint source within the circle is too bright to be the pulsar.

reprocessing the timing data with a later version of the TEMPO package. PSR J0529−6652 was re-detected with a high signal-to-noise ratio in one of the other beams of the multibeam receiver during a targeted search of SGR 0526−66 for radio pulsations with the center beam. This observation was not used in the timing effort.

3.5 Discussion

3.5.1 Expected Number of Detectable Pulsars in the Magellanic Clouds

Establishing formation rates of neutron stars and determining the beaming fraction and luminosity characteristics of pulsars is important for understanding the birth and emission characteristics of the pulsar population. Although the Galactic pulsar population currently provides a much larger sample of pulsars with which to model and test these parameters, the Galactic population suffers from selection effects and distance uncertainties. The Magellanic Clouds, which suffer much less from these effects, can be used to constrain and test these parameters. We can compare the observed number of pulsars in the SMC with the number predicted from several methods using different model assumptions. Table 3-4 summarizes the predictions using each of the methods described below.

Estimate Using the Solar Neighborhood Pulsar Population

Here we follow the method of McConnell et al. (1991) to estimate the number of SMC pulsars expected to be detectable in our survey. The number of potentially observable pulsars in the SMC, $N_{\rm SMC}$, can be estimated using the number of potentially observable pulsars in our solar neighborhood which is defined as a cylinder with a base area of 1 kpc^2 in the Galactic disk. We scale this number by a factor which includes the mass ratio of the SMC and the solar neighborhood and their relative star formation rates,

Table 3-3. Refined Astrometric and Spin Parameters for Three Previously Known Pulsars

Name	J0455−6951	J0502−6617	J0529−6652
α (J2000)	$04^h55^m47^s.55(8)$	$05^h02^m50^s.53(10)$	$05^h29^m50^s.92(13)$
δ (J2000)	$-69°51'34''.3(6)$	$-66°17'58''.8(9)$	$-66°52'38''.2(9)$
P (ms)	320.422711526(12)	691.25141818(4)	975.72496638(6)
$\dot{P}$ ($\times 10^{-15}$)	10.2119(15)	23.090(6)	15.509(6)
DM (pc cm^{-3})	94.89(14)	68.9(3)	103.2(3)
Epoch of Period (MJD)	48757.0	48771.0	48739.0
RMS residual (ms)	1.6	2.2	3.1
Number of TOAs	1/7/28	2/0/27	4/1/28
Timing span (days)	850	850	900
τ_c (Myr)	0.50	0.48	1.0
B ($\times 10^{12}$ G)	1.8	4.0	3.9
$\dot{E}$ (erg s^{-1})	1.2×10^{34}	2.8×10^{33}	6.6×10^{32}
Notes	in LMC	in LMC	in LMC

Parameters as in Table 3-2.

Table 3-4. Predicted Number of Non-recycled SMC Pulsars

Method	Solar neighborhood pulsar density	Supernova remnant formation rate	Type II supernova rate
Reference	McConnell et al. (1991)	Filipovic et al. (1998)	Turatto (2000)
N ($L > 1$ mJy kpc^2)[a]	960 ± 200	7200 ± 1500	1520 ± 1070
N ($L > L_0$)[b]	0.5 ± 0.1	3.7 ± 0.8	0.8 ± 0.5

[a]Number of potentially observable pulsars with $L_{400} > 1$ mJy kpc^2.

[b]Number of potentially observable pulsars with L_{400} greater than our survey sensitivity limit L_0 of 1950 mJy kpc^2.

$$N_{\rm SMC} = R\frac{N_{\rm SN}M_{\rm SMC}}{M_{\rm SN}}. \quad (3.1)$$

Here R is the star formation rate in the SMC relative to the solar neighborhood, $N_{\rm SMC}$ is the number of potentially observable pulsars in the solar neighborhood, and $M_{\rm SMC}$ and $M_{\rm SN}$ are the masses of the SMC and solar neighborhood respectively.

Vangioni-Flam et al. (1980) indicate that the number of massive O and B stars per unit mass is about the same for the SMC and solar neighborhood, indicating that R is about equal to unity. However, Lequeux (1984) indicates that the star formation rate per unit total mass in the SMC is greater than the solar neighborhood, yielding $R = 1.6$. We use the latter number in our calculation.

The total masses of the solar neighborhood and SMC are estimated to be $9 \times 10^7 M_\odot$ and $1.8 \times 10^9 M_\odot$ (Vangioni-Flam et al. 1980). The number of potentially observable pulsars with $L_{400} > 1$ mJy kpc^2 in the solar neighborhood has been estimated by Lyne et al. (1998). They derive a local space density of 30 ± 6 kpc^{-2} and 28 ± 12 kpc^{-2} for non-recycled and millisecond pulsars respectively above this luminosity limit. These estimates include beaming effects.

Putting these numbers in Equation 3.1 gives 960 ± 200 and 900 ± 385 for the number of potentially observable non-recycled and millisecond pulsars respectively in the SMC with $L_{400} > 1$ mJy kpc^2, where the uncertainties are dominated by the estimate of $N_{\rm SN}$.

We can convert this result into an estimate of the number of pulsars detectable in our survey, which is sensitive to pulsars with $L_{400} > 1950$ mJy kpc^2 for most periods. We assume that the Galactic and SMC luminosity distributions are similar. Lorimer et al. (1993) show for the Galactic population, the number of pulsars above a luminosity threshold L_0 scales as the inverse of L_0. Thus, the expected number of pulsars above our detection limits in the SMC is 0.5 ± 0.1 non-recycled pulsars and 0.5 ± 0.2 millisecond pulsars. The number of detectable millisecond pulsars is an upper limit since this number may be overestimated for two reasons. First, our survey sensitivity begins to significantly decrease at millisecond periods (see Figure

3-2), and second, the younger age of the oldest star clusters in the SMC relative to the Galaxy (Olszewski, Suntzeff, & Mateo 1996) may indicate that the SMC contains fewer old recycled pulsars at the present epoch.

There are currently two known SMC pulsars, both of which are non-recycled. Assuming Poisson statistics, we find that the model prediction is excluded at about the 1σ level for non-recycled pulsars. No such statement can be made for the millisecond pulsars since the model prediction is an upper limit. Thus our current findings remain consistent with this model prediction. We would need to find a total of about 10 non-recycled and 10 millisecond pulsars above our luminosity sensitivity limit to exclude the model predictions at the 3σ level.

Estimate Using the SNR Formation Rate in the SMC

We can also estimate the expected number of detectable non-recycled pulsars in the SMC by using the estimated SNR formation rate. Filipovic et al. (1998) have estimated the SNR formation rate in the SMC by assuming a relationship between flux density and SNR age (van Buren & Greenhouse 1994). By using a sample of 10 SNRs in the SMC complete down to 100 mJy, Filipovic et al. (1998) estimate that a SNR is formed once every 350 ± 70 years in the SMC. If we make the assumptions that 85% of supernovae come from massive progenitors (Tammann, Löffler, & Schröder 1994) with all of these supernovae forming neutron stars (NSs), that the mean lifetime for a pulsar is 10 Myr, and that all NSs formed are active pulsars, then the number of active pulsars predicted in the SMC is 24000 ± 5000. If we then make the assumption that the pulsars will have periods in the range $0.1 \text{ s} < P < 1 \text{ s}$ (typical of non-recycled pulsars), we can apply a beaming factor of 0.3 for this period range (Biggs 1990) to get 7200 ± 1500 potentially observable pulsars.

We again use the Lorimer et al. (1993) luminosity distribution and assume that all pulsars formed will have $L_{400} > 1$ mJy kpc^2. From this we estimate that there should be 3.7 ± 0.8 non-recycled pulsars detectable in our SMC survey. We observe two, which deviates from the prediction at only the 1σ level (assuming Poisson statistics), making the model predictions consistent with our findings. We would need to find a

total of 15 non-recycled SMC pulsars to exclude the model prediction at the 3σ level.

Estimate Using the Supernova Rate in Irregular Galaxies

We can estimate the number of pulsars detectable in our survey using the supernova rate for irregular galaxies, of which the SMC is one. Turatto (2000) estimates that the Type II supernova rate for irregular galaxies is 0.65 ± 0.39 SNu, where SNu is a unit defined as

$$\mathrm{SNu} = \frac{1}{100 \text{ yr}} \frac{1}{10^{10} L_{\odot}^{B}}, \tag{3.2}$$

where $L_{\odot}^{B}$ is the bolometric luminosity of the galaxy in solar units and where $H_0 = 75$ km s^{-1} Mpc^{-1} is assumed.

Vangioni-Flam et al. (1980) estimate the SMC bolometric luminosity to be 7.8×10^8 $L_{\odot}$, implying a Type II supernova rate of $(5 \pm 3) \times 10^{-4}$ per year. We again assume that all compact objects formed in these supernovae are NSs, and that all NSs formed are active pulsars with $L_{400} > 1$ mJy kpc^2 with a mean lifetime of 10 Myr. This yields 5100 ± 3600 active pulsars in the SMC. We again apply the Biggs (1990) beaming fraction of 0.3 for non-recycled pulsars in the range 0.1 s $< P <$ 1 s to get 1520 ± 1070 potentially observable pulsars in the SMC. Scaling this to the number expected to be detectable in our survey using the luminosity law of Lorimer et al. (1993) gives 0.8 ± 0.5 for the predicted number of detectable non-recycled pulsars in our survey.

Our observed sample of two does not exclude this prediction at even the 1σ level. We would need to find a total of 11 non-recycled pulsars above our luminosity sensitivity limit to exclude this prediction at the 3σ level.

3.5.2 The Magellanic Cloud Pulsar Luminosity Distribution on the P-$\dot{P}$ Diagram

Distances to pulsars in our Galaxy are generally determined by the DM-distance model of Taylor & Cordes (1993) which has large uncertainties. This unfortunately

introduces large uncertainties in pulsar luminosity estimates. The Magellanic Clouds have more accurately determined distances than Galactic pulsars, and therefore their pulsars have better known luminosities. Since only the upper end of the luminosity function is detectable in the Magellanic Clouds, we can use luminosity estimates of their pulsars to compare the high end of the Magellanic Cloud pulsar luminosity function with that of the Galaxy.

Table 3-5 lists radio luminosities for the seven known radio pulsars in the Magellanic Clouds using flux density estimates from several sources. Taylor, Manchester, & Lyne (1993) have shown that Galactic pulsars older than $\sim$ 5 Myr have significantly lower luminosities than younger pulsars. Figure 3-7 shows a P-$\dot{P}$ diagram for the seven Magellanic Cloud radio pulsars and the Galactic pulsars which have cataloged radio luminosities, with the 5-Myr isochrone marked. The distribution of the Magellanic Cloud pulsars (which are very luminous) is consistent with the Galactic distribution of luminous pulsars and supports the suggestion of Taylor, Manchester, & Lyne (1993).

3.5.3 Tests of Pulsar Luminosity Laws

The form of luminosity models in which the radio luminosity depends on period and period derivative was first suggested by Lyne, Ritchings, & Smith (1975):

$$\log L = \log \gamma + \alpha \log P + \beta \log \dot{P}_{-15}. \tag{3.3}$$

Here α, β, and γ are adjustable parameters in a given luminosity model, P is the pulsar period in s, and $\dot{P}_{-15}$ is the period derivative divided by 10^{-15}. Lorimer et al. (1993) have suggested two luminosity models in which they have fit model luminosities to the observed Galactic pulsar sample. Table 3-6 lists their best fit model parameters, and they quote a Gaussian standard deviation of 0.8 for each predicted $\log L$ value in the models.

For a range of $\log P$ and $\log \dot{P}_{-15}$ which spans the expected range for non-recycled pulsars and for which our survey sensitivity is roughly constant ($-1.0 < \log P <$

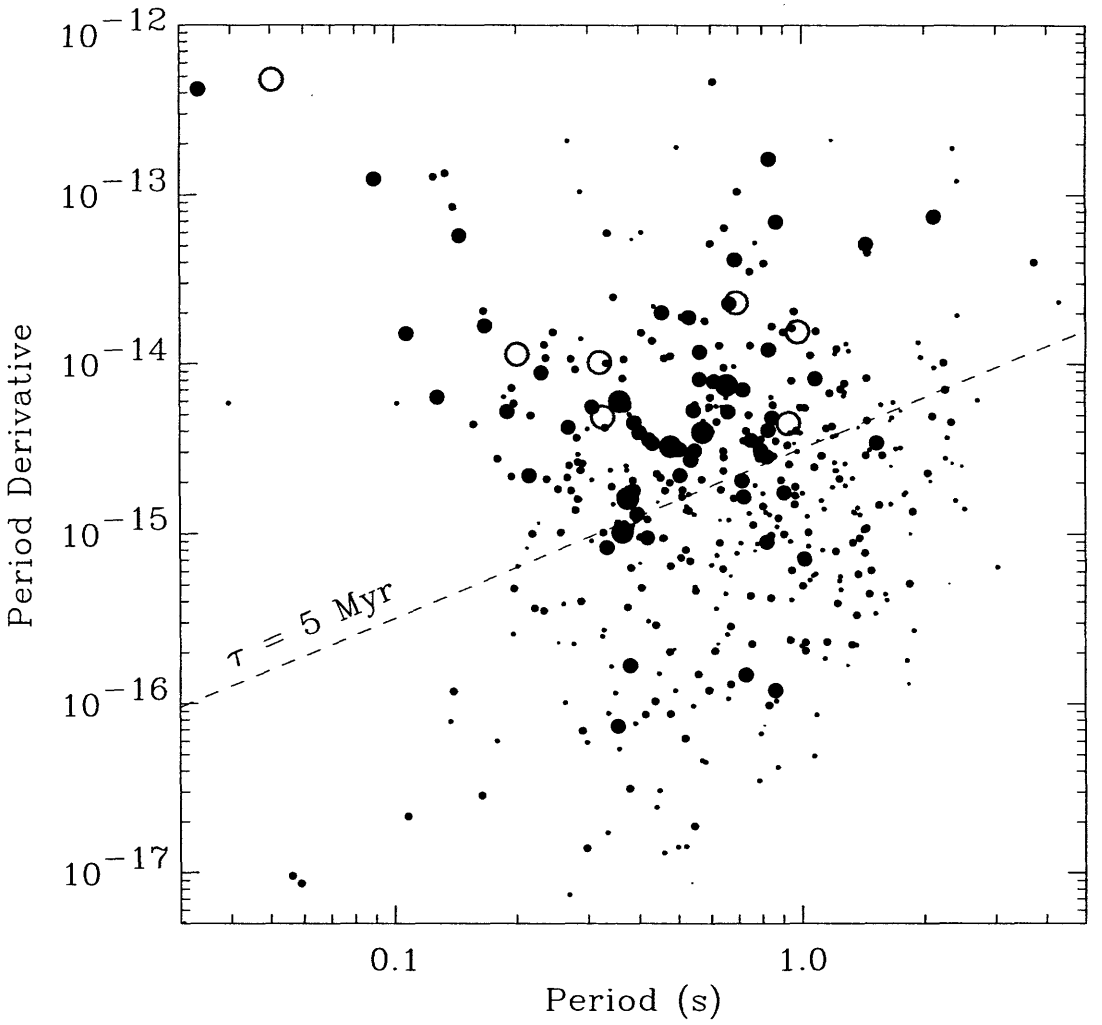

Figure 3-7 P-$\dot{P}$ diagram for a subset of Galactic pulsars with cataloged radio luminosities (filled circles). The symbol size scales logarithmically with increasing radio luminosity. Also shown are the seven Magellanic Cloud pulsars for which a radio luminosity has been estimated (open circles). The dashed line is the 5-Myr isochrone.

Table 3-5. Luminosity Estimates for Magellanic Cloud Pulsars

Name	S_{1374} (mJy)	Reference	S_{610} (mJy)	Reference	L_{400}[a] (mJy kpc^2)
J0045−7319	0.3 ± 0.1	1	1.0 ± 0.2	2	7000 ± 2500
J0113−7220	0.4 ± 0.1	1			9500 ± 2500
J0535−6935	~ 0.05	1			~ 1000
J0537−6910	< 0.06	3	< 0.2[b]	3	< 1200
J0540−6919			~ 0.4[c]	4	~ 2000
J0455−6951			1.0 ± 0.5	2	4900 ± 2500
J0502−6617			0.7 ± 0.4	2	3500 ± 2000
J0529−6652	0.3 ± 0.1	1	1.8 ± 0.8	2	6000 ± 1500

(1) This work

(2) McConnell et al. (1991)

(3) Crawford et al. (1998)

(4) Manchester et al. (1993)

[a]Distances to the LMC and SMC are assumed to be 50 kpc and 57 kpc respectively (Cole 1998).

[b]660-MHz flux density estimate.

[c]640-MHz flux density estimate.

$+0.48$, $-2.0 < \log \dot{P}_{-15} < +3.0$), we have calculated model luminosities and have used the standard deviation quoted to calculate the fraction of radio luminosities above our survey sensitivity limit (1950 mJy kpc^2) relative to luminosities above 1 mJy kpc^2, which we consider to be the potentially observable luminosity range. We used a step size of 0.01 for both $\log P$ and $\log \dot{P}_{-15}$ in the calculation.

This fraction was averaged over the range of $\log P$ and $\log \dot{P}_{-15}$ that we considered, with a weighting factor proportional to the pulsar characteristic age in each case. For a constant pulsar birth rate, this weighting factor accounts for the greater number of pulsars in the larger step sizes at larger ages.

This weighted average was then used with the observed SMC population of two pulsars with $L_{400} > 1950$ mJy kpc^2 to calculate how many pulsars should be potentially observable in the SMC. Table 3-6 outlines Models A and B of Lorimer et al. (1993) and the predicted number of potentially observable pulsars for the SMC in each case.

Assuming Poisson statistics for our observed sample of two pulsars, we find that a total of 14000 ± 10000 and 10000 ± 7000 potentially observable non-recycled SMC pulsars are predicted for Model A and B respectively. Both of these estimates are larger than the three independent estimates of 960, 7200, and 1520 presented above. However, all of the estimates are statistically consistent given the large uncertainties. If additional SMC pulsars are found in more sensitive searches in the future, these model estimates will be more revealing.

3.5.4 OB Associations and Supernova Remnants in the SMC

Only three OB associations are cataloged in the SMC (Wang & Wu 1992) despite the large number of O and B stars in the SMC. None of the associations is located near the newly discovered SMC pulsar PSR J0113−7220. A plot of the known O and B stars in the SMC (Azzopardi 1987; Meyssonnier & Azzopardi 1993) shows that there is no clustering of stars near PSR J0113−7220, though there are a number of O and B stars in the vicinity (Figure 3-8). There is no obvious connection between the location of PSR J0113−7220 and a possible birthplace in an OB association.

The large characteristic age of PSR J0113−7220 is also not helpful, since the pulsar could have traveled half a degree in the SMC during its lifetime if it had a transverse velocity of $\sim$ 500 km/s. Thus the birthplace of the pulsar cannot be pinned down. None of the 15 known SNRs in the SMC (Ye & Turtle 1993) (see Figure 3-8) is likely to be associated with this pulsar. The observable lifetime of a SNR is much less than the pulsar's characteristic age of $\sim$ 1 Myr, and we do not expect such a SNR to be visible. We conclude that we cannot trace the origin of the newly discovered PSR J0113−7220 beyond the fact that it lies in the SMC.

3.5.5 Distribution of Dispersion Measures

The Taylor & Cordes (1993) model of the electron distribution in the Galaxy incorporates layers of electrons in which the density decreases with increasing z-distance from the Galactic plane. This clearly limits the Galactic contribution to the DM as a function of Galactic latitude. One reason that pulsars are believed to be in the Magellanic Clouds is their large DMs, which exceed those expected for Galactic pulsars at that Galactic latitude. The quantity DM $\sin|b|$ is a measure of the z-contribution to the DM and can be used to distinguish Galactic from extragalactic pulsars. Figure 3-4 shows a histogram of the measured DM $\sin|b|$ values for 681 Galactic pulsars. There is a clear dropoff close to zero at about 27 pc cm^{-3} with several pulsars between 30 pc cm^{-3} and 35 pc cm^{-3}. The DM $\sin|b|$ values of Magellanic Cloud pulsars range from 40 pc cm^{-3} to about 90 pc cm^{-3}, a much larger range than the Galactic population itself. One reason for this is that the projected z-contribution of electrons from the Magellanic Clouds is not a flat disk (like our Galaxy), but rather is extended in that direction. This difference can also be seen in Figure 3-5 showing DM vs. $|b|$; the population of Magellanic Cloud pulsars is clearly set apart from the Galactic population of 681 pulsars.

One interesting question to ask is whether the spread in DM seen in the known pulsar population can reveal anything about the Magellanic Clouds themselves. The observed range for the two SMC pulsars is 105 pc cm^{-3} to 125 pc cm^{-3}. The observed range in the LMC (where there are more known pulsars) is about 80 pc cm^{-3}, from

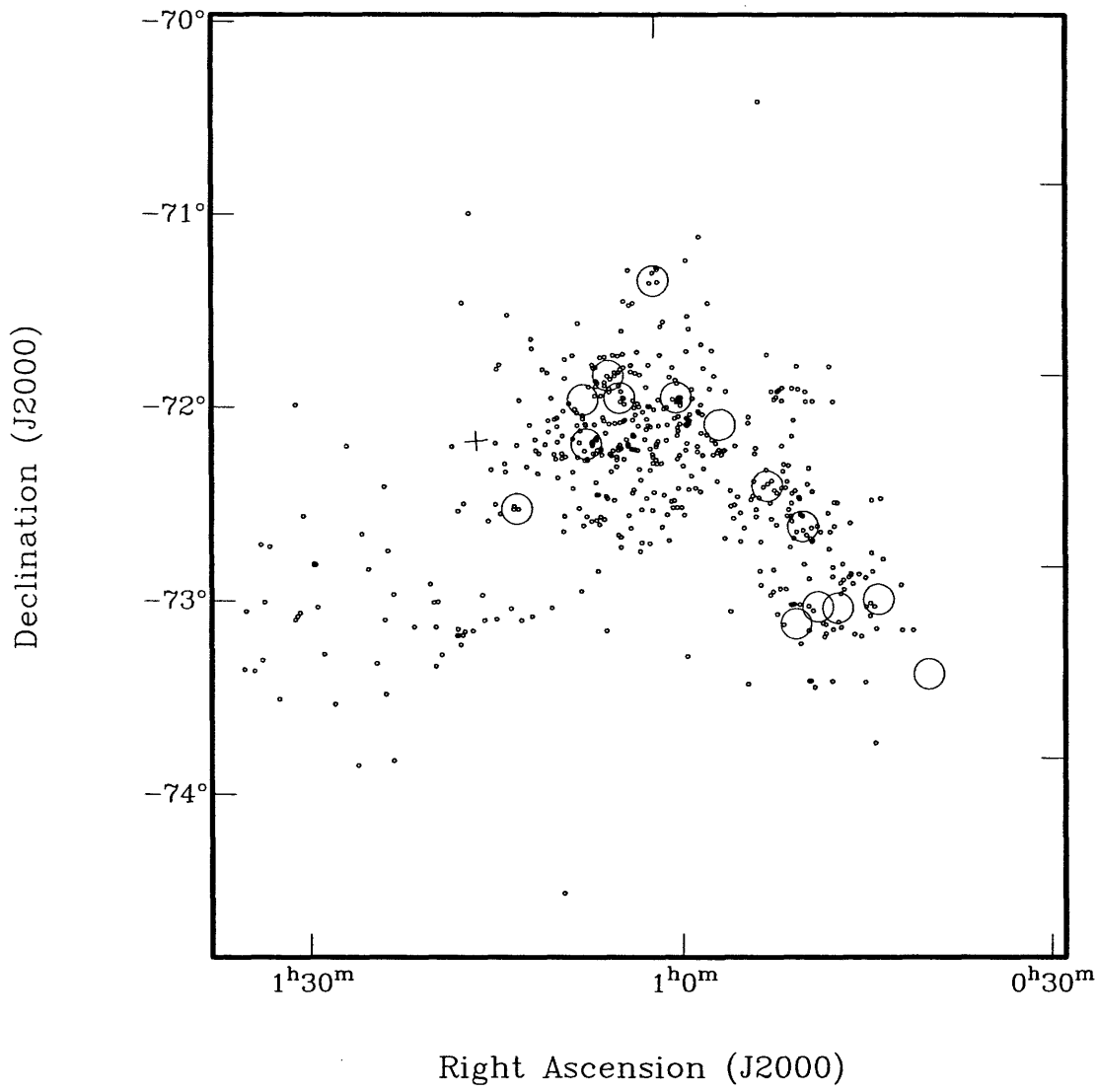

Figure 3-8 Locations of cataloged O and B stars in the SMC (small circles) and 15 known SNRs in the SMC (large circles). The location of the newly discovered SMC pulsar, PSR J0113−7220, is indicated by the cross.

the smallest value of about 70 pc cm^{-3} to the largest value of about 150 pc cm^{-3}. Assuming an electron density of 0.03 cm^{-3} for the Magellanic Clouds, which is comparable to estimated mean Galactic values (Manchester & Taylor 1977; Spitzer 1978; Taylor & Cordes 1993), the DM spread corresponds to a distance range of 0.7 kpc and 2.7 kpc for the SMC and LMC respectively.

From distance measurements of 161 Cepheids in the SMC, Mathewson (1985) has estimated that the depth of the SMC is between 20 kpc and 30 kpc, much larger than the projected size of the SMC on the sky of $\sim$ 4 kpc ($\sim 4°$). The observed DM spread for pulsars in both Magellanic Clouds indicates line-of-sight depths that are much smaller than this, as indicated above. In fact, for an SMC depth of 20-30 kpc, the observed DM distribution implies a mean electron density $n_e < 0.001$ cm^{-3}, much smaller than Galactic values. Our survey is sensitive to high-DM pulsars and our data processing includes DM $\lesssim$ 450 pc cm^{-3}, but we did not detect any pulsars with DM $>$ 125 pc cm^{-3}. Our results are more consistent with the recent finding that the inner part of the SMC is roughly spherical in morphology (Zaritsky et al. 2000). Should a significant number of additional SMC pulsars be found in the future with this same DM range, this will be at odds with an elongated line-of-sight morphology for the SMC.

3.6 Conclusions

We have conducted a survey of the SMC for radio pulsars and have discovered two new pulsars, one of which is located within the SMC. We present timing results for both of these pulsars as well as refined values for three previously known LMC pulsars. We have also discovered serendipitously a new pulsar in the LMC which is too weak to allow a coherent timing solution to be obtained, bringing the total number of known rotation-powered pulsars in the Magellanic Clouds to eight. The results of our survey are consistent with the expected number of detectable SMC pulsars estimated using several methods. The observed SMC population is also consistent with two pulsar luminosity models of Lorimer et al. (1993). However, the small

number of pulsars currently known in the SMC prevents significant constraints on the parameter assumptions made in these estimates. The luminosity distribution of the Magellanic Cloud pulsar population on the P-$\dot{P}$ diagram is consistent with the Galactic distribution of luminous pulsars and supports the conclusion of Taylor, Manchester, & Lyne (1993) that pulsars younger than ~ 5 Myr are preferentially more luminous than older pulsars. The DM distribution of the newly discovered pulsars is consistent with the known pulsar population in the Magellanic Clouds. Both of the known SMC pulsars are in a narrow DM range, and if additional SMC pulsars are found in the future which are also confined to this narrow DM range, this will be at odds with the SMC depth estimated from Cepheid observations. The discovery of a larger number of pulsars through increased survey sensitivity may be able to set constraints on various interesting parameters for the Magellanic Clouds (e.g., star formation rates, supernova and SNR formation rates, and morphology and plasma distribution).

Table 3-6. Predictions from Two Luminosity Models

Parameter	Model A	Model B
α	-1.50	-1.61
β	0.50	0.64
γ (mJy kpc^2)	2.85[a]	3.50
f[b]	0.0001416	0.0002071
N ($L > 1$ mJy kpc^2)[c]	14000 ± 10000	10000 ± 7000

Models from Lorimer et al. (1993).

[a]For Model A, if $L > 28.5$ mJy kpc^2 in the calculation, then L is set to 28.5 mJy kpc^2.

[b]Fraction of model pulsars with luminosities above $L_{400} > 1950$ mJy kpc^2 (our SMC survey sensitivity) relative to all model pulsars with $L_{400} > 1$ mJy kpc^2.

[c]Number of potentially observable non-recycled SMC pulsars with $L > 1$ mJy kpc^2, assuming Poisson statistics.

Chapter 4

Timing of New PM Survey Pulsars

This chapter describes follow-up pulsar timing studies of 39 newly discovered pulsars from the Parkes Multibeam Pulsar Survey (PM Survey) (described in Chapter 2) in the right ascension range $13^{\rm h} < \alpha < 15^{\rm h}$. We report timing results for the 39 pulsars, and discuss several of the pulsars which have interesting characteristics determined from timing.

4.1 Introduction

Much of the scientific motivation for pulsar timing is presented in Chapter 1. After a pulsar is discovered and confirmed in a survey, it is regularly observed in timing observations for about a year to determine accurate spin and astrometric parameters. It is through timing results that physical parameters can be estimated. Measurements of P and $\dot{P}$ are used to estimate the characteristic age, surface magnetic field, and spin-down luminosity for the pulsar (derived in Sections 1.3.9 and 1.3.10). Establishing these parameters not only identifies interesting pulsars which are worthy of further study individually, but it also provides the necessary information for pulsar population synthesis studies. Models of the underlying pulsar population and its evolution can be constructed and tested with a large sample of observed pulsars. This can help address a number of interesting issues, such as the birth properties of pulsars, the evolution of the pulsar magnetic field and radio luminosity with age, and the total

number of pulsars in the Galaxy.

In a few cases, a second frequency derivative $\ddot{f}$ can be measured with sufficient accuracy to estimate a braking index, and this can be compared to the theoretical value of $n = 3$ for magnetic dipole radiation. These measurements can be used to test pulsar emission models (e.g., Melatos 1997). An accurate position is also established through timing. Accurate positions can be used for proper motion studies and associations with coincident objects such as supernova remnants (SNRs) and pulsar wind nebulae (PWN) in the case of young pulsars.

Timing results can also be used to establish the presence of a binary companion. Features of the companion (e.g., mass, orbital period) can also be constrained with the timing solution. Pulsar timing also reveals irregularities in the pulsar period, which can be traced in some cases to timing noise (described in Chapter 1). This is particularly relevant for young pulsars, which exhibit the most timing noise. Sudden changes in the spin period which are caused by glitches can also be seen in timing observations. Studies of glitch behavior can be used to constrain the neutron star interior.

4.2 Timing Procedure

In order to determine the astrometric and spin parameters for a pulsar, observations are taken roughly monthly for a span of about a year. In each observation, the start time of the observation is accurately recorded and is synchronized with the observatory time standard. After the data are recorded, the frequency channels are dedispersed at the pulsar's estimated dispersion measure (DM) and summed, and the time series is folded at the estimated P for the pulsar to create a pulse profile. The folded profile is then cross-correlated with a high signal-to-noise ratio (S/N) template profile of the pulsar to obtain an accurate time-of-arrival (TOA) for a pulse in the observation. A single TOA is recorded for each observation.

The recorded TOAs are analyzed using the TEMPO software package[1] and the

[1] http://pulsar.princeton.edu/tempo.

JPL DE200 planetary ephemeris (Standish 1990). TEMPO converts each TOA to the solar system barycenter and fits the observed TOAs to those predicted from a model which includes astrometric and spin parameters for the pulsar. Underlying the model is the assumption that the rotational phase ϕ of the pulsar is described by

$$\phi(T) = \phi_0 + fT + \frac{1}{2}\dot{f}T^2 + \frac{1}{6}\ddot{f}T^3 + \ldots, \tag{4.1}$$

where $f \equiv 1/P$ is the spin frequency of the pulsar and T denotes pulsar proper time.

Residuals in phase are determined by the time difference between the observed and model TOAs. A best-fit model is determined by minimizing the set of residuals according to

$$\chi^2 = \sum_{i=1}^{N} \left(\frac{\phi(t_i) - n_i}{\sigma_i / P} \right)^2, \tag{4.2}$$

where N is the number of TOAs used in the fitting procedure, ϕ is the observed pulse phase at time t_i, n_i is the phase of the nearest integer pulse number in the model, and σ_i is the uncertainty in the measured TOA.

Residuals defined in this way have a phase ambiguity in which a residual deviation greater than half a pulse period results in the observed TOA being compared to the TOA of the adjacent predicted pulse. Thus, the parameters must be boot-strapped toward a best-fit solution in which TOAs are successively incorporated when the residual is assured to be significantly smaller than half a pulse period for the next TOA included. This phase-connection procedure allows the timing solution to avoid local minima in the minimization of χ^2.

In practice, this phase-connection procedure means that several observations must be taken in rapid succession (over the course of a few days) in order to establish a sufficiently accurate P before a non-zero intrinsic $\dot{P}$ introduces a phase ambiguity. Once P has been established, $\dot{P}$ is then incorporated into the model and additional TOAs are included in the analysis.

The presence of timing noise can causes a phase jitter which can prevent a phase-connection from being obtained due to the fact that the astrometric and spin param-

eters are both initially uncertain in the model. In cases where the initial position in the timing model is wrong, a sinusoidal trend in the residuals is introduced which has a one-year period. In the early stages of the timing, this trend is similar to the parabolic trend introduced from a large value of $\dot{P}$. Observations must be taken for a significant fraction of a year ($\gtrsim$ 9 months) to determine the true trend in the residuals and distinguish between the two cases. In some cases, pulsars which were thought to be young due to a large $\dot{P}$ had a wrong position instead.

Both of these difficulties can be avoided by radio imaging with pulsar gating, which can establish with certainty the pulsar position and thereby reveal a young age in early stages in the timing. An independently established position will constrain the model sufficiently accurately to obtain a phase connection in the one case and will break the position/period derivative degeneracy in the other. Young pulsars are particularly good targets for imaging since they are often interesting systems to study individually, they typically have large $\dot{P}$ values, and they are the pulsars which exhibit the most timing noise.

4.3 Observations

Thirty-nine newly discovered PM Survey pulsars in the right ascension range $13^{\rm h} < \alpha < 15^{\rm h}$ were timed as part of this thesis work. After confirmation, each new pulsar was observed in a set of grid pointings in which the pointing center of the beam was adjusted by $9'$ in four directions (N, S, E, and W). The S/N of each of the resulting detections was used to determine a more accurate position than that obtained in the discovery observation.

Each pulsar was then typically observed regularly in timing observations for a span of about a year, yielding a total of 15-25 TOAs which were used to obtain a timing solution. Included in these TOAs were several closely-spaced TOAs, used for phase connecting the timing solution (described above). Timing observations were taken at Parkes using the multibeam receiver with the same observing setup as used for the PM Survey (described in Chapter 2), with the exception that only the center beam

was used. Observing integration lengths for each pulsar depended on the detection strength in the discovery observation. Typical lengths were a few minutes for most pulsars. Data were stored on Exabyte tape and were processed by dedispersing and folding the data as described above.

Several of the pulsars timed as part of this effort were also imaged using pulsar gating in order to determine positions and thereby confirm their young ages in the timing solutions. Several of the timing solutions presented in this chapter make use of the position results from the imaging effort, which is presented in Chapter 5.

4.4 Results and Discussion

Each of the 39 pulsars which was timed is isolated and appears in the publically available list of 187 newly discovered PM Survey pulsars[2] (Table 2-6). Tables 4-1, 4-2, and 4-3 list the astrometric, spin, and derived physical parameters respectively for the 39 pulsars. Figures 4-1 and 4-2 show the 1374-MHz integrated pulse profiles for the sample.

Four of these pulsars were suspected to be young initially from a large $\dot{P}$ measured in a comparison of P in observations separated in time. These pulsars were imaged to obtain accurate positions (see Chapter 5). All of these pulsars proved to be young, and they are listed in Table 2-7.

The timing results presented here will be part of a comprehensive study of the characteristics of the pulsar population once the PM Survey has been completed and all of the new discoveries have been timed. The timing sample presented in this thesis is directionally biased (due to the artificial right ascension limits) and is not large enough by itself to conduct such a study. A population synthesis analysis is beyond the scope of this thesis and will be done by others in the future.

[2]http://www.atnf.csiro.au/research/pulsar/psr/pmsurv/pmwww/pmpsrs.db.

Table 4-1. Observing and Astrometric Parameters for 39 PM Survey Pulsars

PSR	α (J2000) (hh:mm:ss)	δ (J2000) (dd:mm:ss)	$N_{\rm TOA}$	Span (d)	rms[a] (ms)
J1301−6305[b]	13:01:45.8(1)	−63:05:34(1)	39	600	2.3
J1302−6313	13:02:19.2(7)	−63:13:29(4)	16	360	7.7
J1303−6305	13:03:00.0(2)	−63:05:01(1)	16	400	1.8
J1305−6203	13:05:20.9(3)	−62:03:22(1)	17	400	1.7
J1305−6256	13:05:28.0(4)	−62:56:39(3)	15	400	2.5
J1307−6318	13:07:54.7(6)	−63:18:35(4)	21	560	8.8
J1309−6415	13:09:16.6(7)	−64:15:59(5)	15	420	4.9
J1312−6400	13:12:07.2(1)	−64:00:55.6(9)	25	430	0.8
J1314−6101	13:14:23.4(9)	−61:01:16(6)	22	370	7.0
J1317−6302	13:17:44.69(7)	−63:02:52.2(6)	23	400	0.8
J1322−6241	13:22:32.1(1)	−62:41:53.5(8)	18	400	1.0
J1324−6146	13:24:43.9(5)	−61:46:00(3)	27	370	4.5
J1327−6400	13:27:10.3(1)	−64:00:13.1(6)	25	600	1.7
J1341−6023	13:41:07.37(3)	−60:23:34.7(5)	17	380	0.3
J1344−6059	13:44:40.0(6)	−60:59:27(6)	12	400	4.7
J1345−6115	13:45:44.4(2)	−61:15:31(2)	17	400	1.8
J1347−5947	13:47:19.38(4)	−59:47:39.8(5)	16	420	0.3
J1348−6307	13:48:42.4(4)	−63:07:04(4)	17	440	3.8
J1349−6130	13:49:36.65(4)	−61:30:17.1(4)	23	400	0.5
J1354−6249	13:54:35(1)	−62:49:30(7)	14	360	7.7
J1403−6310	14:03:14.0(2)	−63:10:27(1)	17	360	1.1
J1406−6121	14:06:50.04(6)	−61:21:27.9(6)	30	520	1.4
J1407−6048	14:07:58.6(1)	−60:48:59(1)	21	540	2.6
J1407−6153	14:07:56.5(5)	−61:53:59(6)	17	500	8.0
J1412−6111	14:12:59.6(1)	−61:11:30.5(7)	20	360	0.8
J1412−6145[b]	14:12:07.69(5)	−61:45:28.8(6)	39	650	1.5
J1413−6141[b,c]	14:13:09.87(9)	−61:41:13(1)	56	680	2.2
J1413−6222	14:13:05.47(8)	−62:22:28(1)	27	480	1.8
J1416−6037	14:16:30.6(2)	−60:37:59.5(9)	18	360	0.9
J1418−5945	14:18:32.2(5)	−59:45:03(9)	13	380	3.6
J1420−6048[b]	14:20:08.3(1)	−60:48:18.1(9)	20	400	0.3
J1424−5822	14:24:32.11(3)	−58:22:56.0(2)	18	420	0.3
J1425−6210	14:25:07.7(3)	−62:10:05(1)	15	360	1.1
J1429−5935	14:29:25.9(1)	−59:35:59(1)	20	560	1.6
J1434−6006	14:34:05.3(2)	−60:06:29.0(9)	17	370	1.2
J1434−6029	14:34:39.1(3)	−60:29:49(3)	16	400	2.3
J1444−5941	14:44:46.5(3)	−59:41:19(3)	17	400	2.3
J1452−5851	14:52:52.58(7)	−58:51:13(2)	16	400	1.0
J1457−5902	14:57:31.9(1)	−59:02:04(2)	17	420	1.3

Figures in parentheses represent 1σ uncertainties in the last digit quoted.

[a]Root-mean-square of residuals in the best-fit timing solution.

[b]Independent position determined from radio imaging.

[c]Glitched twice during timing span.

Table 4-2. Spin Parameters for 39 PM Survey Pulsars

PSR	P (s)	$\dot{P}$ (10^{-15} s/s)	Epoch (MJD)	DM (pc cm^{-3})
J1301−6305[a]	0.18452809509(6)	266.747(3)	51206.0	374(1)
J1302−6313	0.9678462129(4)	6.33(8)	51342.0	532.6(1)
J1303−6305	2.3066415539(4)	2.18(16)	51138.0	351(1)
J1305−6203	0.42776184224(8)	32.14(3)	51138.0	468(1)
J1305−6256	0.47823093284(12)	2.11(4)	51138.0	971(1)
J1307−6318	4.9624272525(20)	21.1(4)	51206.0	440(1)
J1309−6415	0.6194535568(3)	8.79(12)	51303.0	581.7(1)
J1312−6400	2.43743249609(11)	0.68(5)	51303.0	119.1(1)
J1314−6101	2.9483896038(15)	11.7(9)	51396.0	319.7(1)
J1317−6302	0.26127055606(3)	0.102(6)	51138.0	683(1)
J1322−6241	0.50605841373(5)	2.587(18)	51138.0	619(1)
J1324−6146	0.8441085753(3)	5.58(14)	51397.0	805.7(1)
J1327−6400	0.280677974168(13)	31.177(4)	51206.0	687(1)
J1341−6023	0.627285365870(16)	19.461(8)	51280.0	371.2(1)
J1344−6059	0.5401023201(3)	−0.02(9)	51312.0	446.9(1)
J1345−6115	1.25308459010(18)	3.25(8)	51138.0	271(1)
J1347−5947	0.609961754304(15)	14.160(7)	51294.0	297.1(1)
J1348−6307	0.9277722389(3)	3.79(7)	51304.0	599.1(1)
J1349−6130	0.259362860073(9)	5.125(4)	51138.0	284(1)
J1354−6249	2.951938334(3)	14.8(11)	51396.0	252.0(1)
J1403−6310	0.39917017693(5)	0.094(20)	51341.0	303.1(1)
J1406−6121	0.213074653776(14)	54.701(3)	51111.0	544(1)
J1407−6048	0.49234420664(5)	3.156(8)	51161.0	575(1)
J1407−6153	0.7016149492(3)	8.85(7)	51093.0	627(1)
J1412−6111	0.52915639797(4)	1.91(3)	51031.0	309(1)
J1412−6145	0.315224970657(12)	98.6598(13)	51186.0	514(1)
J1413−6141[b]	0.28562462018(16)	333.44(15)	51500.0	676(1)
J1413−6222	0.2924077024 9(3)	2.229(6)	51092.0	808(9)
J1416−6037	0.29558048193(3)	4.280(15)	51031.0	289(1)
J1418−5945	1.6725956721(9)	0.4(4)	51286.0	355.0(1)
J1420−6048[a]	0.06817789226(3)	82.9230(7)	51312.0	361.5(1)
J1424−5822	0.366734060217(6)	3.943(3)	51368.0	323.7(1)
J1425−6210	0.50173030987(8)	0.48(4)	51031.0	421(1)
J1429−5935	0.76391483053(8)	42.751(9)	51232.0	453(1)
J1434−6006	0.30636786268(4)	3.020(17)	51396.0	331.6(1)
J1434−6029	0.96334832315(16)	1.03(8)	51137.0	275(1)
J1444−5941	2.7602279448(6)	8.2(3)	51137.0	163(1)
J1452−5851	0.38662501748(3)	50.706(18)	51280.0	265.1(1)
J1457−5902	0.39073936418(5)	12.306(14)	51312.0	477.4(1)

Figures in parentheses represent 1σ uncertainties in the last digit quoted.

[a]Second frequency derivative also fitted in timing solution.

[b]Glitched twice during timing span.

Table 4-3. Physical Parameters for 39 PM Survey Pulsars

PSR	$\log \tau_c$[a] (yr)	$\log B$[b] (G)	$\log \dot{E}$[c] (erg s^{-1})
J1301−6305	4.0	12.9	36.2
J1302−6313	6.4	12.4	32.4
J1303−6305	7.2	12.4	30.8
J1305−6203	5.3	12.6	34.2
J1305−6256	6.6	12.0	32.9
J1307−6318	6.6	13.0	30.8
J1309−6415	6.0	12.4	33.2
J1312−6400	7.8	12.1	30.3
J1314−6101	6.6	12.8	31.3
J1317−6302	7.6	11.2	32.4
J1322−6241	6.5	12.1	32.9
J1324−6146	6.4	12.3	32.6
J1327−6400	5.2	12.5	34.7
J1341−6023	5.7	12.5	33.5
J1344−6059	–	–	–
J1345−6115	6.8	12.3	31.8
J1347−5947	5.8	12.5	33.4
J1348−6307	6.6	12.3	32.3
J1349−6130	5.9	12.1	34.1
J1354−6249	6.5	12.8	31.4
J1403−6310	7.8	11.3	31.8
J1406−6121	4.8	12.5	35.3
J1407−6048	6.4	12.1	33.0
J1407−6153	6.1	12.4	33.0
J1412−6111	6.6	12.0	32.7
J1412−6145	4.7	12.8	35.1
J1413−6141	4.1	13.0	35.8
J1413−6222	6.3	11.9	33.5
J1416−6037	6.0	12.1	33.8
J1418−5945	7.8	11.9	30.5
J1420−6048	4.1	12.4	37.0
J1424−5822	6.2	12.1	33.5
J1425−6210	7.2	11.7	32.2
J1429−5935	5.5	12.8	33.6
J1434−6006	6.2	12.0	33.6
J1434−6029	7.2	12.0	31.7
J1444−5941	6.7	12.7	31.2
J1452−5851	5.1	12.7	34.5
J1457−5902	5.7	12.3	33.9

[a]Characteristic age.

[b]Surface magnetic field.

[c]Spin-down luminosity.

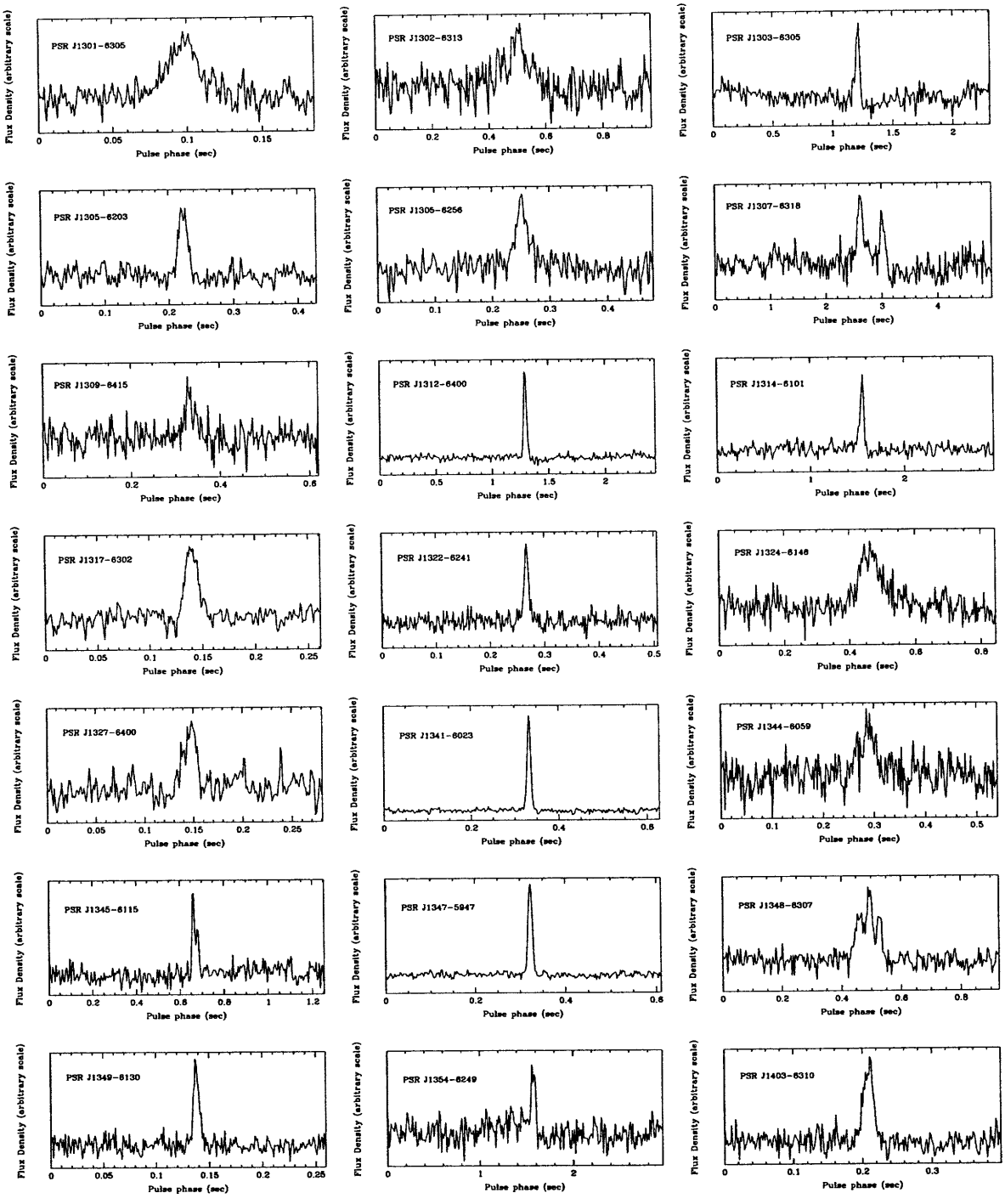

Figure 4-1 Integrated 1374-MHz pulse profiles for PM Survey pulsars which were timed as part of this thesis work.

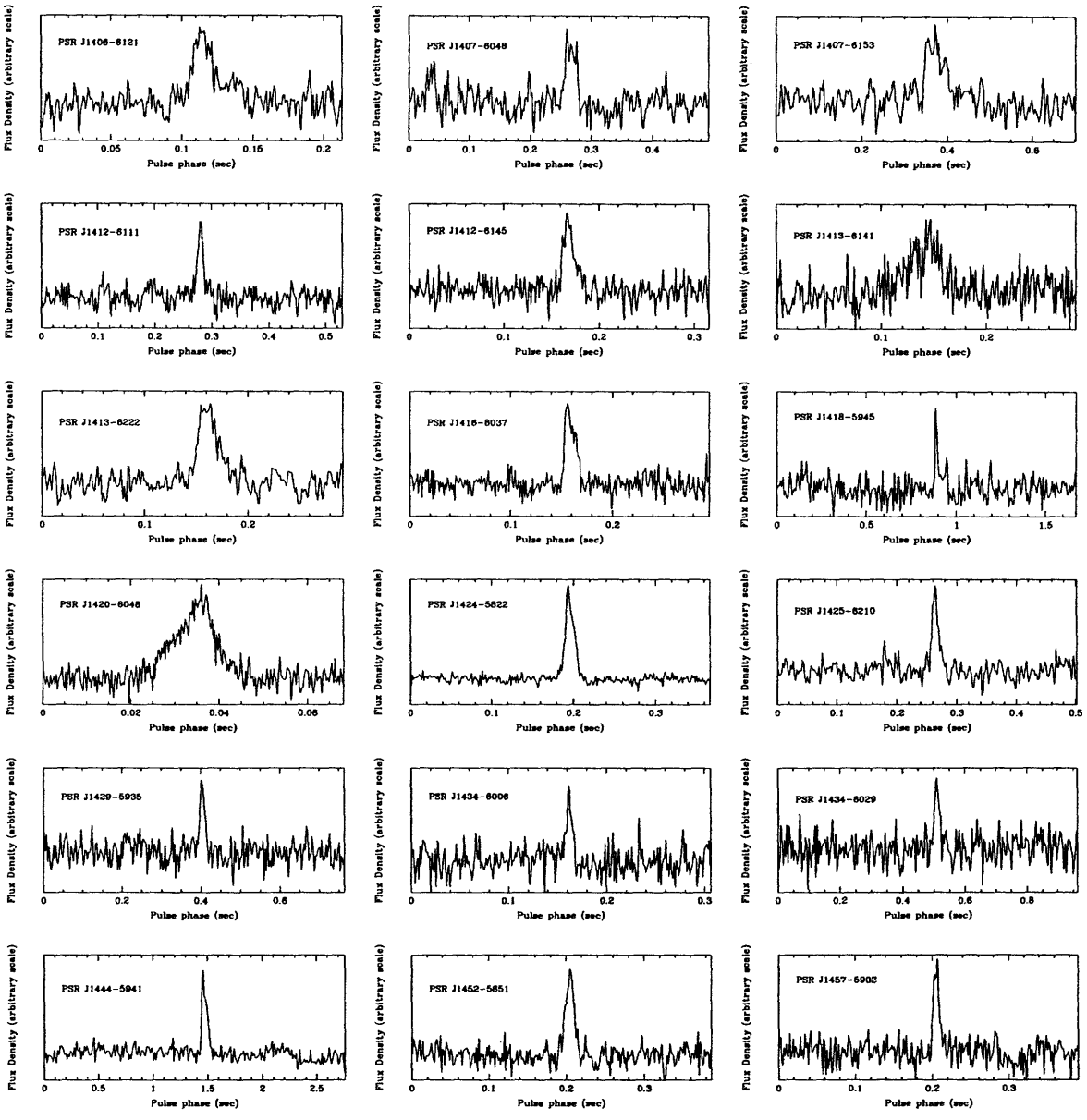

Figure 4-2 Integrated 1374-MHz pulse profiles for PM Survey pulsars which were timed as part of this thesis work (continued).

4.4.1 PSRs J1301−6305 and J1420−6048: Two Young Pulsars with Timing Noise

Four of the 39 pulsars in the timing list were imaged to establish accurate positions (see Chapter 5). In two cases (PSRs J1301−6305 and J1420−6048), when the position established from the imaging was fixed in the timing solution, a clear cubic residual was seen. A second frequency derivative $\ddot{f}$ was therefore incorporated into the timing solution.

The values of $\ddot{f}$ obtained for these pulsars are listed in Table 4-4 along with the implied braking indices. The fact that the measured values for the braking indices in these two cases are much too large to be accounted for in braking models indicates that the second frequency derivatives arise from timing noise and are not intrinsically related to the pulsar's electromagnetic braking.

4.4.2 PSR J1420−6048: A Gamma-ray Pulsar?

The position of PSR J1420−6048 firmly establishes a spatial coincidence with both an extended X-ray source seen in *ASCA* imaging observations and the gamma-ray source GeV J1417−6100 (2EGS J1418−6049) (Roberts & Romani 1998; Roberts et al. 1999). Roberts et al. (1999) speculated on the presence of an energetic pulsar in the vicinity which could be the source of this emission, but no such pulsar was seen at the time. It is suggestive that since PSR J1420−6048 has been shown through pulsar timing to be a fast, energetic young pulsar, it could be powering extended X-ray emission and be a source of gamma-rays.

Figure 4-3 shows an *ASCA* image of the region (see also Figure 4 of Roberts & Romani 1998) with the established position of PSR J1420−6048 indicated. The pulsar is clearly coincident with one of the extended X-ray sources in the field, and this source could be an X-ray nebula powered by the pulsar wind. A positive identification of PSR J1420−6048 with the gamma-ray source GeV J1417−6100 would also be quite interesting: this would help answer the question of the nature of Galactic gamma-ray sources, most of which have not been identified. The position of the gamma-ray

source error circle encompasses several extended radio and X-ray sources (see Figure 1 of Roberts et al. 1999), but PSR J1420−6048 is the best candidate currently known for the gamma-ray source. A full discussion is presented elsewhere (D'Amico et al. 2000).

4.4.3 PSR J1307−6318: A Pulsar with a 4.9 s Period

PSR J1307−6318 has a 4.9 s period, the third longest period yet measured for a radio pulsar. The results from timing indicate that PSR J1307−6318 has a magnetic field which is large ($B \sim 1 \times 10^{13}$ G) but still within the normal range for the population. This pulsar is also not particularly young, with $\tau_c \sim 3.7$ Myr.

The two radio pulsars known to have longer periods, PSRs J1951+1123 (Camilo & Nice 1995) and J2144−3933 (Young, Manchester, & Johnston 1999), have rotation periods of 5.1 s and 8.5 s, respectively. Both of these pulsars have smaller magnetic fields (4×10^{12} G and 2×10^{12} G) and are older (27 Myr and 270 Myr) than PSR J1307−6318.

One striking feature of PSR J1307−6318 is its pulse profile morphology. Figure 4-4 shows four integrated 1374-MHz profiles from four separate timing observations. These profiles show that the pulsar has a double-peak morphology. However, the profile morphology is variable, with a changing amplitude for the peaks. One of the peaks even disappears in the noise in one of the profiles, possibly due to mode nulling in the radio emission. The profiles also suggest a bridge of emission connecting the two peaks.

The overall morphology of the profile suggests that the emission is originating from a hollow conal beam and that the magnetic axis is close to the line-of-sight axis (Lyne & Manchester 1988). Conal emission is a characteristic which is more prevalent among young, fast pulsars (see Appendix B). Radio polarimetry of PSR J1307−6318 could help determine whether the emission is from a hollow conal beam and could help constrain the emission geometry of the pulsar.

In contrast to PSR J1307−6318, both PSRs J1951+1123 and J2144−3933 have single-peak profiles which are among the narrowest observed. Measured half-power

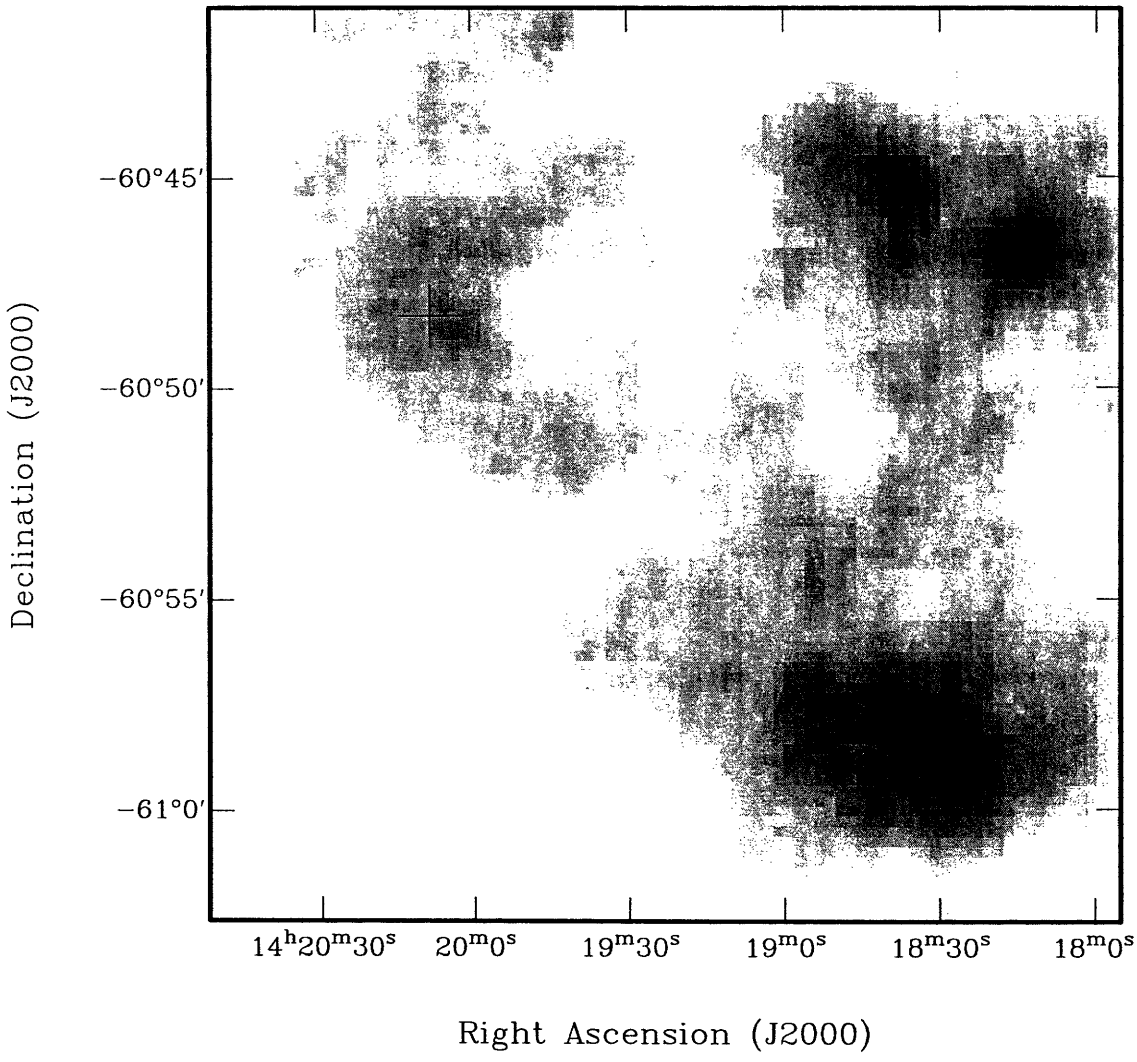

Figure 4-3 An *ASCA* X-ray image of the region containing PSR J1420−6048 (see also Figure 4 of Roberts & Romani 1998). The position of the pulsar established from timing is indicated by the cross and is spatially coincident with one of the extended X-ray sources in the region.

Table 4-4. Measured Second Frequency Derivatives for Two Pulsars

PSR	$\ddot{f}$ $(10^{-22}$ Hz$^{-3})$	n^{a}
J1301−6305	2.3 ± 0.4	20 ± 4
J1420−6048	7 ± 2	32 ± 10

[a]Measured braking index $n = f\ddot{f}\dot{f}^{-2}$, where $f \equiv 1/P$ (see Table 4-2 for measured values of P and $\dot{P}$). These values are likely due to timing noise and do not reflect the true braking indices for the pulsars.

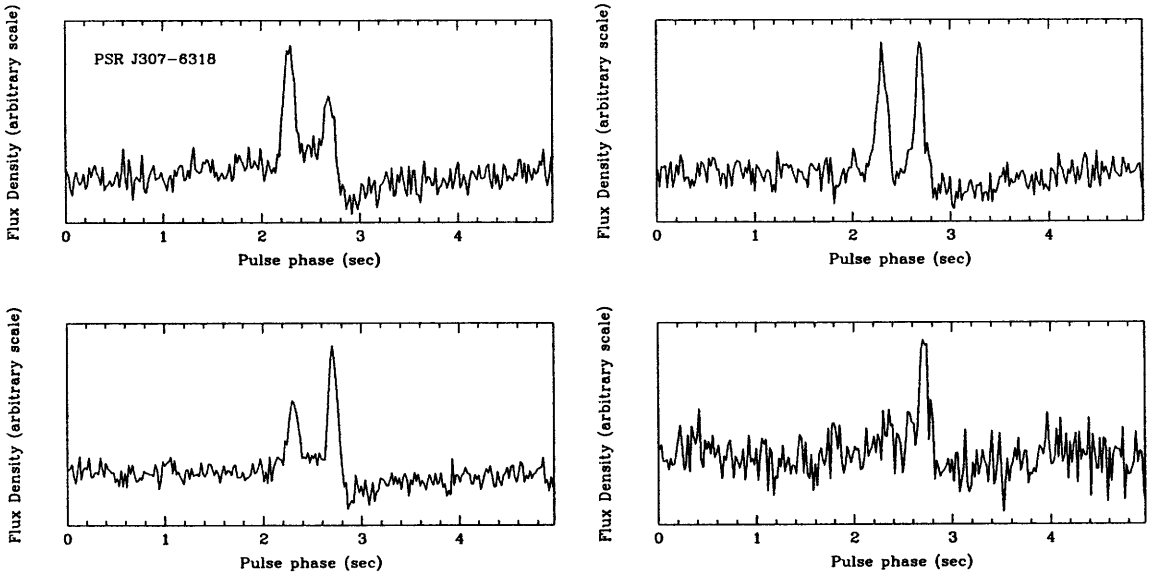

Figure 4-4 Four integrated 1374-MHz pulse profiles for PSR J1307−6318, a pulsar with a 4.9 s period. Each profile was obtained by folding a timing observation of length 300 s, except for the lower-right profile which had length 100 s. The dual peak in the profile is in contrast to the very narrow peaks seen in other old radio pulsars with long periods and suggests emission from a hollow conal beam (see Appendix B). The variability in the amplitudes of the peaks and the changing profile morphology in the different observations is clear.

widths for the peaks are 0.39% and 0.23% of the pulse period, respectively (Camilo & Nice 1995; Young, Manchester, & Johnston 1999). This morphology is suggestive of a single core component for the emission mechanism (Lyne & Manchester 1988). The profile morphology of long-period pulsars has important implications for their detectability and beaming fraction, since narrow profiles are less likely to intersect our line of sight.

4.4.4 PSR J1413−6141: A Glitching Pulsar

PSR J1413−6141 has been shown to have undergone two glitches during the 680 d timing span. Since these glitch parameters introduce additional degrees of freedom in the timing model, it was crucial to establish an accurate position for the pulsar through imaging in order to get a timing solution. A final timing solution was obtained by using the position of a point source in a radio image of the region which was suspected to be the pulsar (see Chapter 5).

Incorporating the two glitches in the timing model and fitting over the entire timing data span gave a solution with a final position (listed in Table 4-1) which was consistent with the point-source position in the radio image. The glitch parameters for the best-fit timing solution are presented in Table 4-5. PSR J1413−6141 is the seventeenth young radio pulsar ($\tau_c < 100$ kyr) known to glitch, including the recently reported glitch activity for PSR J1119−6127 (Camilo et al. 2000), PSR J1617−5055 (Torii et al. 2000), and several other young pulsars (Wang et al. 2000). PSR J1413−6141 is the first pulsar discovered in the PM Survey observed to glitch.

Table 4-5. Glitch Parameters for PSR J1413−6141

Parameter	First Glitch	Second Glitch
$\Delta f/f$ ($\times 10^{-8}$)[a]	3.4 ± 0.2	97.1 ± 0.2
Epoch of Glitch (MJD)	51301 ± 2	51464 ± 9
Non-zero $\lvert\Delta \dot{f}\rvert$ seen?	Y	N

[a]Fractional increase in rotational frequency f at time of glitch.

Chapter 5

Pulsar-Gated Radio Imaging of Young PM Survey Pulsars

5.1 Introduction

We have observed fields containing seven young pulsars which have been discovered in the Parkes Multibeam Pulsar Survey (PM Survey) (described in Chapter 2). All of these pulsars have southern declinations ($-64° < \delta < -54°$) and were observed with the Australia Telescope Compact Array (ATCA).

5.1.1 Motivation for Pulsar-Gated Imaging

Pulsar-gated radio imaging of young pulsars is important for several reasons. The primary motivation for using this technique is to establish with certainty the positions of pulsars. The purpose of this is two-fold. First, accurate positions are sometimes necessary for obtaining timing solutions, particularly for young pulsars which can exhibit timing noise. Timing noise, explained in Chapters 1 and 4, can prevent a timing solution from being obtained since it introduces deviations in the spin-down behavior which cannot be modeled and accounted for. With accurate positions, the timing solution has fewer free parameters and can more easily be constrained.

The second reason for obtaining accurate positions with gating is to establish as-

sociations with extended radio objects. This is also particularly relevant for young pulsars, which can be associated with supernova remnants (SNRs) or pulsar wind nebulae (PWNe). The motivation for finding and studying such associations is presented in Chapter 1. Sensitivity to PWNe can also be enhanced with pulsar gating by allowing the pulsed flux to be subtracted from the image, thereby increasing sensitivity to faint underlying emission. Spectral index information can also be obtained from imaging to help identify objects as sources with a non-thermal emission mechanism. Chapter 6 discusses this in further detail.

5.1.2 Radio Interferometry

The following description follows the one presented in the ATCA User's Guide.[1]

For the radio imaging work on the pulsars in this chapter, we have used the ATCA, an earth-rotation aperture synthesis radio interferometer. Earth-rotation aperture synthesis is explained in detail elsewhere (Clark 1989; Thompson, Moran, & Swenson 1986). In radio synthesis observations, the antennas of the array are used in pairs to form interferometers. By correlating the signals from each antenna pair, called a baseline, one measures the fraction of the signal which is common to both antennas in the pair.

Combining these correlated signals obtained over a long period of time and using a large range of antenna spacings yields a measurement of the spatial coherence function throughout a range of values in the u-v plane, which is the Fourier plane to the sky image plane. The spatial coherence function V is the Fourier transform of the sky intensity distribution:

$$V(u,v) = \int I(\hat{s}) e^{(2\pi i\, \hat{s}\cdot(\vec{r}_i - \vec{r}_j)/\lambda)}\, d\Omega. \tag{5.1}$$

Here $I(\hat{s})$ is the two dimensional intensity distribution on the sky, $\hat{s}$ is the unit vector in the direction of the pointing center toward the celestial source, $(\vec{r}_i - \vec{r}_j)$ is the separation vector between antenna pair ij, and $d\Omega$ indicates integration over the

[1] http://www.narrabri.atnf.csiro.au.

celestial sphere. This expression assumes that the radiation is monochromatic with wavelength λ.

By Fourier transformation of the spatial coherence function, an image of a radio source is produced. This image is convolved with the sampling function determined by the aperture coverage in the u-v plane, and the image must be deconvolved from this sampling function to recover the true intensity distribution. The image formed has the same angular resolution as would be obtained for an image with a single antenna with a diameter equal to the largest baseline separation.

5.1.3 The Australia Telescope Compact Array

The ATCA consists of six 22-m radio antennas located near Narrabri, NSW, Australia (Frater, Brooks, & Whiteoak 1992). Five of the six antennas lie along a three-kilometer railway track, which is oriented east-west. The sixth antenna lies on a 75-m rail-track three kilometers further west, thus allowing a maximum baseline of 6 km. These antennas can be moved along the railway tracks and positioned at any of 37 fixed stations, each of which contains a port that allows the data from the antenna to be transferred to the control building. Due to the location of the stations and other physical constraints, the shortest baseline possible is $\sim$ 30 m.

The antennas are regularly moved to different stations, corresponding to different array configurations used for observing. An observation length of 12 h fully covers the possible spacings in the u-v plane for a given configuration. By observing a given source using multiple configurations and combining the separate u-v data sets, one can get more complete u-v coverage for the sampling function and generally make better images.

Each of the six antennas has an altitude-azimuth mount and a Cassegrain design, with receivers located at the main reflector surface. The feeds are mounted along the main optic axis, allowing observations to be made in two simultaneous orthogonal linear polarizations with low ($\sim$ 1%) instrumental polarization. Each antenna has receivers which are sensitive to four radio frequencies centered at roughly 1.5, 2.4, 5.3, and 8.5 GHz. There are two feeds mounted on each antenna, one of which is

sensitive to radiation at both 1.5 GHz and 2.4 GHz and one at both 5.3 GHz and 8.5 GHz. Each feed has a separate receiver for each of the two frequencies. All receivers run continuously and use cooled FET and HEMT amplifiers that provide wide bandwidths and total system temperatures between 30 K to 65 K, depending on the frequency.

The received signals are amplified and downconverted by mixing with a signal from a local oscillator. The ATCA allows simultaneous observations of both polarizations at the two available frequencies in either dual-receiver system. The center frequencies can be anywhere in the range covered by the selected feed. After downconversion, the signals from each antenna are digitized using two-bit sampling and sent to a correlator. A synchronizing code is added to the data stream from each antenna at the start of each integration cycle to allow each bit in the signal stream to be correctly identified at the correlator.

The correlator compares simultaneous signals from the two data streams from each antenna pair: if the signal from both antennas is in the same state, then the signals are correlated. A plane wavefront approaching the array will, in general, arrive at different antennas at different times due to a geometric delay between the antennas. The signals from the antennas therefore need to be delayed before being presented to the correlator to account for this delay and to account for additional delays from path length differences and instrumental variations.

The output from the correlator for each antenna pair (baseline) is the cross-correlation (lag) function of the signals from the two antennas, which is the Fourier transform of the cross-power spectrum of the two signal streams. This correlator output is then sent to a computer which Fourier transforms the cross-correlation function to recover the (complex) cross-power spectrum for each baseline. Data are averaged for the integration cycle and then written to disk. For our observations, we used an integration cycle time of 40 s. These complex values are the visibilities in the u-v plane which sample the spatial coherence function. A radio image can then be constructed from the measured spatial coherence function by taking the Fourier transform of the function and deconvolving the resulting image. This step is neces-

sary since the spatial coherence function cannot be perfectly sampled by the baseline tracks in the u-v plane.

5.1.4 Pulsar Gating

In normal interferometric radio observations described above, each baseline is integrated for the cycle (in our case 40 s) and a single complex correlation value is obtained for each baseline, representing a single point in the u-v plane. The pulsar gating feature of the ATCA can be used to separately record data for each phase bin of the pulsar's profile. Using an ephemeris for the pulsar, a topocentric pulsar period is determined over the course of the observation. This period will vary slightly over the course of the observation but is constant for each integration cycle. During observing, each integration cycle is split into an integral number of pulse periods, each of which in turn is split into (typically) 32 bins. Each bin is integrated separately, and at the end of the integration cycle, a complex correlation value is output for each phase bin of the profile. Using this technique, the separately recorded binned data can then grouped into on and off-pulse data, thereby allowing two maps to be made from the two data sets, with the difference that the pulsed emission appears at the pulsar's location in only one of the maps. A comparison of the maps reveals the pulsar's position, and a map made from the off-pulse data set provides an increased sensitivity to faint underlying emission at the pulsar's location. Figure 5-1 shows on and off-pulse maps for PSR J1119−6127, using data from only the 6D array configuration. The pulsar is clearly seen as a point source in the on-pulse image and does not appear in the off-pulse image.

5.2 Observations and Data Reduction

Each of the seven pulsar fields we have observed had a southern declination ($\delta < -50°$). We therefore used the ATCA in several configurations for these observations. Typical integrations were about 12 h in each configuration. Two 128-MHz bandwidths (split into 32 × 4-MHz frequency channels) were simultaneously observed, centered

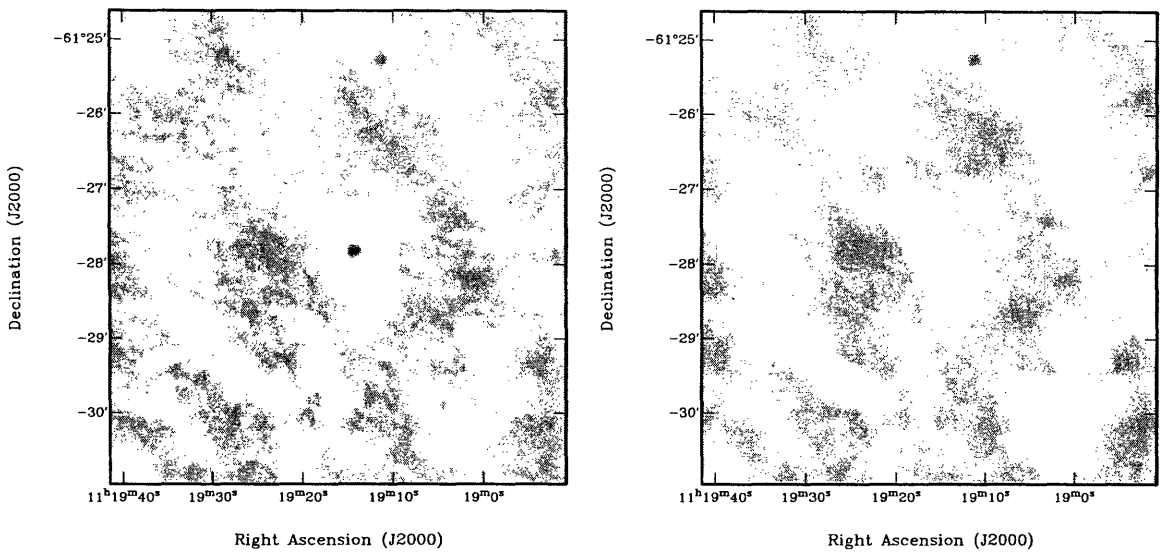

Figure 5-1 1.4-GHz maps of the region containing PSR J1119−6127 made with on-pulse (left) and off-pulse (right) data from gating. The only feature (aside from noise) which is different in the two maps is the pulsar, which appears as a point source.

on radio frequencies of 1.4 GHz and 2.5 GHz. Each of the 32 frequency channels was sensitive to full Stokes parameters for each baseline. Table 5-1 lists the observing parameters for each of the observations.

Using the MIRIAD[2] data reduction package (Sault & Killeen 1998), the data were first edited for radio frequency interference (RFI). The amplitudes of every point in the u-v plane are checked for excessively large values, which would clearly indicate the presence of RFI. These data were removed (flagged). The remaining data were then phase calibrated and flux calibrated using the sources listed in Table 5-1. Phase calibration determines a time-dependent gain function for each antenna in the array. Both phase and amplitude corrections based on these gain functions are then applied to the recorded u-v data. Phase calibration also determines the instrumental polarization as a function of time and corrects for this. In flux calibration, an overall scale factor (which is tied to the flux density of a well-known source) is applied to the u-v data.

In the observations with the highest spatial resolutions, we used pulsar gating

[2]http://www.atnf.csiro.au/computing/software/miriad.

Table 5-1. ATCA Observing Parameters for Seven Pulsars

PSR	Observing Dates	Array Config	PKS Phase Calibrator	PKS Flux Calibrator	Integration Time (h)
J0940−5428	1999 Aug 18-19	6D[a]	0823−500	1934−638	6.8
J1112−6301[b]	1999 Nov 28-29	0.375	1036−697	1934−638	12.9
	1999 Dec 16	1.5A[a]	1036−697	1934−638	12.4
J1119−6127	1998 Oct 30-31	6D[a]	1036−697	1934−638	12.8
	1998 Nov 1[c]	6D	1036−697	1934−638	7.6
	1999 Nov 25-26	0.375	1036−697	1934−638	12.8
	1999 Dec 14	1.5A	1036−697	1934−638	13.0
J1301−6305	1999 Aug 22-23	6D[a]	1329−665	1934−638	10.6
	1999 Dec 15-16	1.5A	1329−665	1934−638	12.4
J1413−6141[d]	1998 Nov 1	6D[e]	1329−665	1934−638	8.8
	1998 Nov 1-2	6D[e]	1329−665	0823−500	4.6
	1999 Nov 27-28	0.375	1329−665	1934−638	13.1
	1999 Dec 17-18	1.5A	1329−665	1934−638	12.6
J1420−6048	1999 Aug 20-21	6D[a]	1329−665	1934−638	11.5

Unless otherwise specified, data were taken at center frequencies of 1384 MHz and 2496 MHz with 32 phase bins used in the gating. 128-MHz bandwidths were used for each frequency in each observation.

[a]Gating results used to estimate a position and flux density.

[b]16 phase bins used in gating.

[c]Center frequencies of 1344 MHz and 2240 MHz used.

[d]PSR J1412−6145 also included in these observation fields.

[e]Glitch activity prevented successful gating.

to separately record data for each of 32 phase bins of the pulsar's profile. In the case of PSR J1112−6301, the gating hardware could only accommodate 16 bins due to the fast period of the pulsar. The bins for each frequency channel were phase adjusted to account for the effect of dispersion using the MIRIAD task PSRFIX. Since the dispersion measure (DM) for each pulsar is known prior to observation, the dispersive time delay of the pulse in each of the frequency channels is known. This can be converted into a pulse phase delay by dividing the time delay by the pulsar period P, which is also known. The adjusted phase bins were grouped into on and off-pulse data. In two cases pulsar gating was not used. PSRs J1412−6145 and J1413−6141 were in the same field, and gating on PSR J1413−6141 was attempted. However, since this pulsar had glitched, an accurate topocentric pulse period was not obtained.

5.3 Position and Flux Density Results

From the gated data we made on and off-pulse u-v data sets. The off-pulse u-v data set was subtracted from the on-pulse data set, leaving only the pulsar's pulsed signal in the presence of noise. We then used the UVFIT procedure in MIRIAD to find a best-fit point source position and flux density in the u-v data set with uncertainties in this fit. The fitted positions had an additional uncertainty from the position uncertainty of the phase calibrators. The calibrator with the most poorly determined position, PKS 1036−697, had an uncertainty less than $0.1''$ (N. Tasker, unpublished work). Adding in quadrature the positional uncertainty from the fit with that of the phase calibrator yielded a best-fit gated position for each pulsar. This position was checked for consistency against the position of the pulsar roughly determined from a comparison of maps made with the on and off-pulse data (Figure 5-1).

These interferometric positions were then used for the pulsar positions in the timing solution. Once sufficiently accurate model parameters were obtained in each timing solution, the position was allowed to vary in the fit to fully minimize the residuals. In several cases a second frequency derivative was introduced in the timing

solution to maintain consistency between the timing model position and the position from gating. Table 5-2 lists the best-fit positions from the pulsar gating and from the final timing solutions for comparison. In the case of PSRs J1412−6145 and J1413−6141, positions were estimated from point-source positions in the maps. In two cases (PSRs J0940−5428 and J1420−6048) there are minor discrepancies in the declination values estimated from the two methods. This can be attributed to timing noise, which is prevalent among young pulsars.

Due to timing noise and a degeneracy between the astrometric and spin parameters, a timing solution was obtained for PSR J1119−6127 which was incorrect. ATCA gated observations of this pulsar were used to break this degeneracy by establishing the position with certainty. Once the position was established, a correct timing solution was determined which included a braking index. The timing results for PSR J1119−6127 are presented along with a full discussion of the procedure elsewhere (Camilo et al. 2000).

The best-fit flux density from UVFIT was also recorded. An additional 5% uncertainty in the flux density was added in quadrature to the UVFIT flux density uncertainty. This conservatively accounts for the uncertainty in the flux calibration. Table 5-3 lists the flux density estimates from both the 1.4-GHz and 2.5-GHz data. In most cases the spectral index α could also be estimated, though with a large uncertainty. For PSRs J1412−6145 and J1413−6141, flux densities were estimated from the flux densities of point-sources in the maps at the pulsar location.

We have used the estimated 1.4-GHz flux densities to check the PM Survey sensitivity calculation presented in Chapter 2. This check is described in Chapter 2.

Table 5-2. ATCA Position Estimates for Seven Pulsars

PSR	Freq (MHz)	Array Config	Gated Position[a]	Timing Position[a]	σ^b
J0940−5428	1384	6D	α = 09:40:58.258(15)	α = 09:40:58.22(4)	0.9
			δ = −54:28:39.78(23)	δ = −54:28:40.6(3)	2.2
J1112−6103	2496	1.5A	α = 11:12:14.859(86)	α = 11:12:14.81(4)	0.5
			δ = −61:03:31.74(65)	δ = −61:03:31.1(6)	0.7
J1119−6127	1384	6D	α = 11:19:14.300(21)	α = 11:19:14.24(5)	1.1
			δ = −61:27:49.48(15)	δ = −61:27:49.8(5)	0.6
J1301−6305	1384	6D	α = 13:01:45.725(27)	α = 13:01:45.8(1)	0.7
			δ = −63:05:34.48(23)	δ = −63:05:34(1)	0.5
J1412−6145[c]	1384	6D	α = 14:12:08(1)	α = 14:12:07.69(5)	0.3
			δ = −61:45:29(4)	δ = −61:45:28.8(6)	0.1
J1413−6141[c]	1384	6D	α = 14:13:10(1)	α = 14:13:09.87(9)	0.1
			δ = −61:41:13(4)	δ = −61:41:13(1)	0.0
J1420−6048	2496	6D	α = 14:20:08.237(16)	α = 14:20:08.3(1)	0.6
			δ = −60:48:16.43(15)	δ = −60:48:18.1(9)	1.8

Figures in parentheses represent 1σ uncertainties in the least-significant digit quoted.

[a]J2000 positions in units of hours:minutes:seconds for right ascension (α) and degrees:arcminutes:arcseconds for declination (δ).

[b]Discrepancy in the values obtained from gating and timing.

[c]No pulsar gating used. Position obtained from point-source position in map.

Table 5-3. ATCA Flux Density Estimates for Seven Pulsars

PSR	Freq (MHz)	Array Config	Flux Density (mJy)	α^{a}
J0940−5428	1384	6D	0.66(4)	+0.7(3)
	2496		0.98(12)	
J1112−6103	1384	1.5A	0.54(13)	−1.3(8)
	2496		0.25(5)	
J1119−6127	1384	6D	1.02(7)	−1.4(3)
	2496		0.44(5)	
J1301−6305	1384	6D	0.47(9)	−0.9(6)
	2496		0.28(4)	
J1412−6145[b]	1384	6D	0.6(3)	–
	2496		0.2(2)	
J1413−6141[b]	1384	6D	0.8(4)	–
	2496		0.4(2)	
J1420−6048	1384	6D	1.09(8)	−1.0(7)
	2496		0.61(17)	

Figures in parentheses represent 1σ uncertainties in the least-significant digit quoted.

[a]Spectral index α determined from 1.4-GHz and 2.5-GHz flux density measurements, where $S \sim \nu^{\alpha}$.

[b]No pulsar gating used. Flux density obtained from point-source flux density in map.

Chapter 6

G292.2−0.5: A New SNR Associated with PSR J1119−6127

This chapter is a modified self-contained paper titled, "G292.2−0.5: A New Supernova Remnant Associated with PSR J1119−6127," to be submitted for publication in the *Astrophysical Journal* (Crawford et al. 2000a).

From radio observations with the Australia Telescope Compact Array (ATCA), we have discovered a previously unknown shell supernova remnant (SNR), G292.2−0.5, coincident with the 1.7 kyr-old pulsar PSR J1119−6127. The shell morphology and size are consistent with other young shell SNRs and support the interpretation that G292.2−0.5 is physically associated with and has an age comparable to PSR J1119−6127. We have also set upper limits on the surface brightness of a pulsar wind nebula (PWN) associated with PSR J1119−6127. These upper limits are consistent with the faint PWN expected around a young, high-magnetic-field pulsar. These results suggest a possible explanation for the lack of central activity in many young SNR shells.

6.1 Introduction

The motivation for finding and studying associations between pulsars and supernova remnants (SNRs) is outlined in Chapter 1. The discovery of PSR J1119−6127 in the

Parkes Multibeam Pulsar Survey (PM Survey) and its characteristics derived from pulsar timing are described in Chapter 2. PSR J1119−6127 is a 408-ms pulsar with the highest period derivative yet measured for any radio pulsar. Full details of the timing results for this pulsar are outlined elsewhere (Camilo et al. 2000; see also Chapters 2 and 5). The characteristic age of PSR J1119−6127 is $\tau_c \equiv P/2\dot{P} = 1.6$ kyr, and a measurement of the second period derivative, and hence a braking index, indicates an age of $\tau = 1.7 \pm 0.1$ kyr, assuming an initial period much less than the current one. If the initial period were closer to the present period, the pulsar would be even younger (Equation 1.11). PSR J1119−6127 is clearly one of the youngest pulsars known.

Each of the other three known radio pulsars with $\tau_c < 2$ kyr is associated with a SNR: PSR J0534+2200 (B0531+21), the Crab pulsar, is associated with the Crab nebula (Staelin & Reifenstein 1968), PSR J1513−5908 (B1509−58) is associated with SNR G320.4−1.2 (Seward & Harnden 1982; Gaensler et al. 1999), and PSR J0540−6919 (B0540−69) is associated with SNR 0540−69.3 (Seward, Harnden, & Helfand 1984). However, the next two youngest pulsars, PSRs J1614−5047 (B1610−50) and J1617−5055 are not associated with any known SNR (Kaspi et al. 1998; Stappers, Gaensler, & Johnston 1999). Table 6-1 shows the list of known radio pulsars with $\tau_c < 10$ kyr and their associations.

It therefore might be expected that PSR J1119−6127 would be associated with a SNR. There is no cataloged SNR in the immediate vicinity of PSR J1119−6127 (Green 1998),[1] and the only previous radio image of this region, an 843-MHz radio image of the region from the Molonglo Galactic Plane Survey (Green et al. 1999),[2] does not convincingly demonstrate the presence of a SNR. Figure 6-1 shows this image with the positional uncertainty of PSR J1119−6127 from the discovery observation indicated by the circle. There are several bright radio sources in the vicinity of the pulsar, including two which have been identified as HII regions (NGC 3603 and NGC 3576). These sources lie within 1° of the pulsar and have sidelobes which interfere with the

[1] http://www.mrao.cam.ac.uk/surveys/snrs/.
[2] http://www.astrop.physics.usyd.edu.au/MGPS/.

Table 6-1. SNR Associations for Pulsars with $\tau_c < 10$ kyr

PSR	τ_c[a] (kyr)	P (ms)	B[b] ($\times 10^{12}$ G)	SNR	Radio shell?	Radio PWN?
J0534+2200	1.26	33	3.8	G184.6−5.8 (Crab)	N	Y
J1513−5908	1.55	150	15.4	G320.4−1.2	Y	N
J1119−6127[c]	1.61	408	41.0	G292.2−0.5	Y	N
J0540−6919	1.67	50	5.0	0540−69.3	Y	Y
J0537−6910[d]	4.98	16	0.9	0538−69.1 (N157B)	N	Y
J1614−5047	7.41	231	10.8		N	N
J1617−5055	8.01	69	3.1		N	N

Entries ranked by characteristic age.

[a]Characteristic age.

[b]Surface magnetic field.

[c]Discovered in PM Survey.

[d]X-ray pulsar only.

emission near the pulsar. There are also artifacts from the mosaicking process which was used to make the image. The presence of sidelobes and imaging artifacts prevent a clear detection of extended radio emission in the vicinity of the pulsar. Additional imaging data with spectral index information and better resolution and sensitivity are necessary to establish whether or not this radio emission is associated with PSR J1119−6127.

In addition, pulsar-gated observations allow the pulsed flux to be subtracted from the image, thereby giving a precise interferometric position for the pulsar and increased sensitivity to faint underlying emission which might otherwise be missed. Searching for a possible pulsar wind nebula (PWN) associated with PSR J1119−6127 is particularly important since of the three youngest pulsars known, two (the Crab and PSR J0540−6919) have observed radio PWNe and one (PSR J1513−5908) does not (see Table 6-1). PSR J1513−5908 is similar to PSR J1119−6127 in two respects. Both of these pulsars have relatively long periods (150 ms for PSR J1513−5908 and 408 ms for PSR J1119−6127) compared to other young pulsars: the periods of the Crab pulsar and PSR J0540−6919 are 33 ms and 50 ms, respectively. Both PSRs J1513−5908 and J1119−6127 also have significantly larger magnetic field strengths than other young pulsars. The magnetic field is an important factor determining the evolution of both the pulsar and its PWN, as demonstrated below.

As part of the imaging campaign to establish positions for young pulsars (see Chapter 5), we determined an accurate position for PSR J1119−6127 using pulsar gating. The position and flux density results for the pulsar are presented in Chapter 5, and we use this position in the rest of the figures shown in this chapter.

6.2 Observations

We have undertaken radio observations toward PSR J1119−6127 with the Australia Telescope Compact Array (ATCA),[3] which is described in detail in Chapter 5. A

[3]http://www.narrabri.atnf.csiro.au. The Australia Telescope is funded by the Commonwealth of Australia for operation as a National Facility managed by CSIRO.

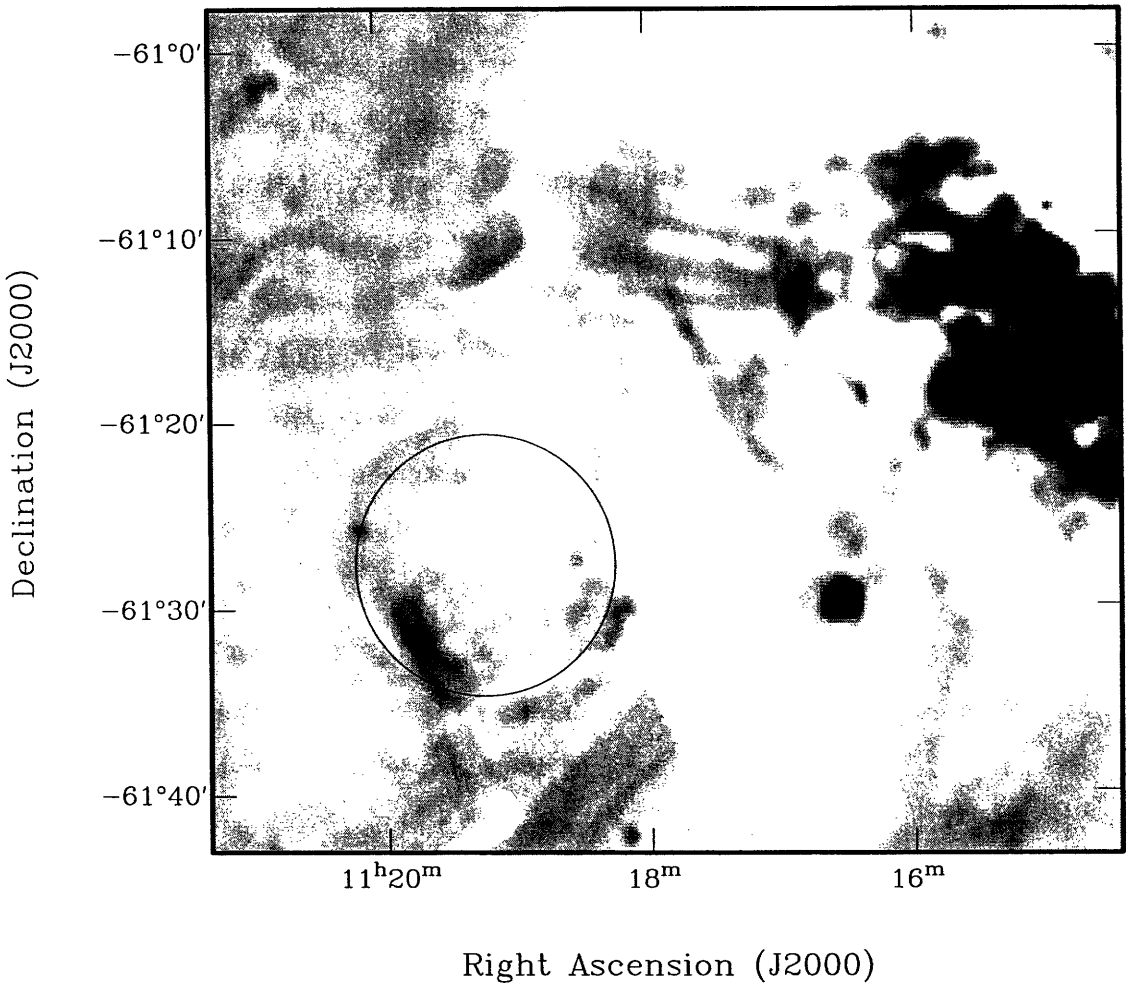

Figure 6-1 An 843-MHz image from the Molonglo Galactic Plane Survey (Green et al. 1999) of the region in which PSR J1119−6127 was discovered. The circle indicates the positional uncertainty of the pulsar from the discovery beam. Extended radio emission from the bright HII region NGC 3603 is seen at the right of the image. Artifacts from the mosaicking imaging process can also be seen in the figure. Extended emission is hinted at near the pulsar's location, but sidelobes from the bright source and imaging artifacts prevent a clear detection of this emission.

set of four observations was taken in three array configurations (6D twice, 0.375, and 1.5A) with integration times of about 12 h in each configuration. Two 128-MHz bandwidths were simultaneously observed, centered on radio frequencies of 1384 MHz and 2496 MHz. Slightly different center frequencies were used in one of the two observations with the 6D configuration to avoid repetition of u-v coverage. Each 128-MHz bandwidth was split into 32 frequency channels with full Stokes parameters for each channel separately recorded for each baseline. All pointings were centered on a single point located about $1'$ from the location of the pulsar. The dates of the observations and details of the observing parameters are presented in Table 5-1.

The recorded data were edited (flagged) to eliminate data corrupted by interference. The data were then phase calibrated and flux calibrated with the sources PKS 1036−697 and PKS 1934−638, respectively, using the MIRIAD[4] software package (Sault & Killeen 1998) (see Chapter 5 for more details). The combined u-v data set consisted of a total of 1172860 unflagged correlations in 60 baselines. The array baselines used ranged from 31 m to 5878 m for the entire data set.

We also used the pulsar gating feature of the ATCA to separately record data for each of 32 phase bins of the pulsar's profile. In Chapter 5 we describe the gating feature of the ATCA, the data processing procedure to determine a position and flux density for PSR J1119−6127, and the results of this effort.

6.3 Data Reduction and Results

6.3.1 Total Intensity Maps

Total intensity maps were made from the ATCA data at both 1.4 GHz and 2.5 GHz using data from all pulsar phase bins from u-v spacings shorter than 7.5 kλ (for the 1.4-GHz map) and from u-v spacings between 0.5 kλ and 7.5 kλ (for the 2.5-GHz map) from all four observations. Baselines with spacings less than 0.5 kλ were discarded for the 2.5-GHz map to reduce interfering sidelobes from the presence of two bright HII

[4]http://www.atnf.csiro.au/computing/software/miriad.

regions, NGC 3603 and NGC 3576, near the pulsar's location. These restricted baseline ranges increased the surface brightness sensitivity in the maps thereby allowing detection of faint extended structure. The maps were deconvolved using a maximum entropy routine (e.g., Cornwell & Evans 1985; Narayan & Nityananda 1986), and the resulting models were restored with a Gaussian beam of size $29'' \times 25''$ (for the 1.4-GHz map) and $21'' \times 20''$ (for the 2.5-GHz map). These beam sizes were determined by the baseline coverage (sampling function) in the u-v plane. The resulting images are shown in Figures 6-2 and 6-3. The two maps clearly indicate extended structure with a circular shell morphology with radius $\sim 7'$. We call this radio shell G292.2−0.5 from its Galactic coordinates. The location of PSR J1119−6127, determined from pulsar gating, lies at the center of the shell. The shell appears limb-brightened and shows no evidence at these spatial scales of radio emission at the location of the pulsar (see below for a more extensive discussion of a possible PWN powered by PSR J1119−6127). The root-mean-square (rms) noise level near the shell is ~ 0.5 mJy in both maps, much higher than the theoretical rms of ~ 0.05 at 1.4 GHz and ~ 0.1 mJy at 2.5 GHz. This is not surprising given the very complicated nature of the region and the presence of the bright HII regions in the vicinity.

6.3.2 Spatial Filtering and Tomography

Spectral index measurements can reveal information about the radio emission mechanism and can help distinguish SNRs from other objects. In order to determine a spectral index for the shell G292.2−0.5, we compared the flux of the brightest features of the shell in the 1.4-GHz and 2.5-GHz maps. However, since the 1.4-GHz and 2.5-GHz maps were made with different u-v coverage and antenna response functions, the two maps must first be spatially filtered before a comparison can be made. This ensures that they have the same spatial resolution and u-v sampling. In the spatial filtering process, we first divided the best 1.4-GHz model of the emission by the 1.4-GHz antenna response function. We then applied the 2.5-GHz response function to this resulting model. This model was then sampled by the 2.5-GHz u-v tracks. These sampled model data were then inverted and deconvolved with exactly the same

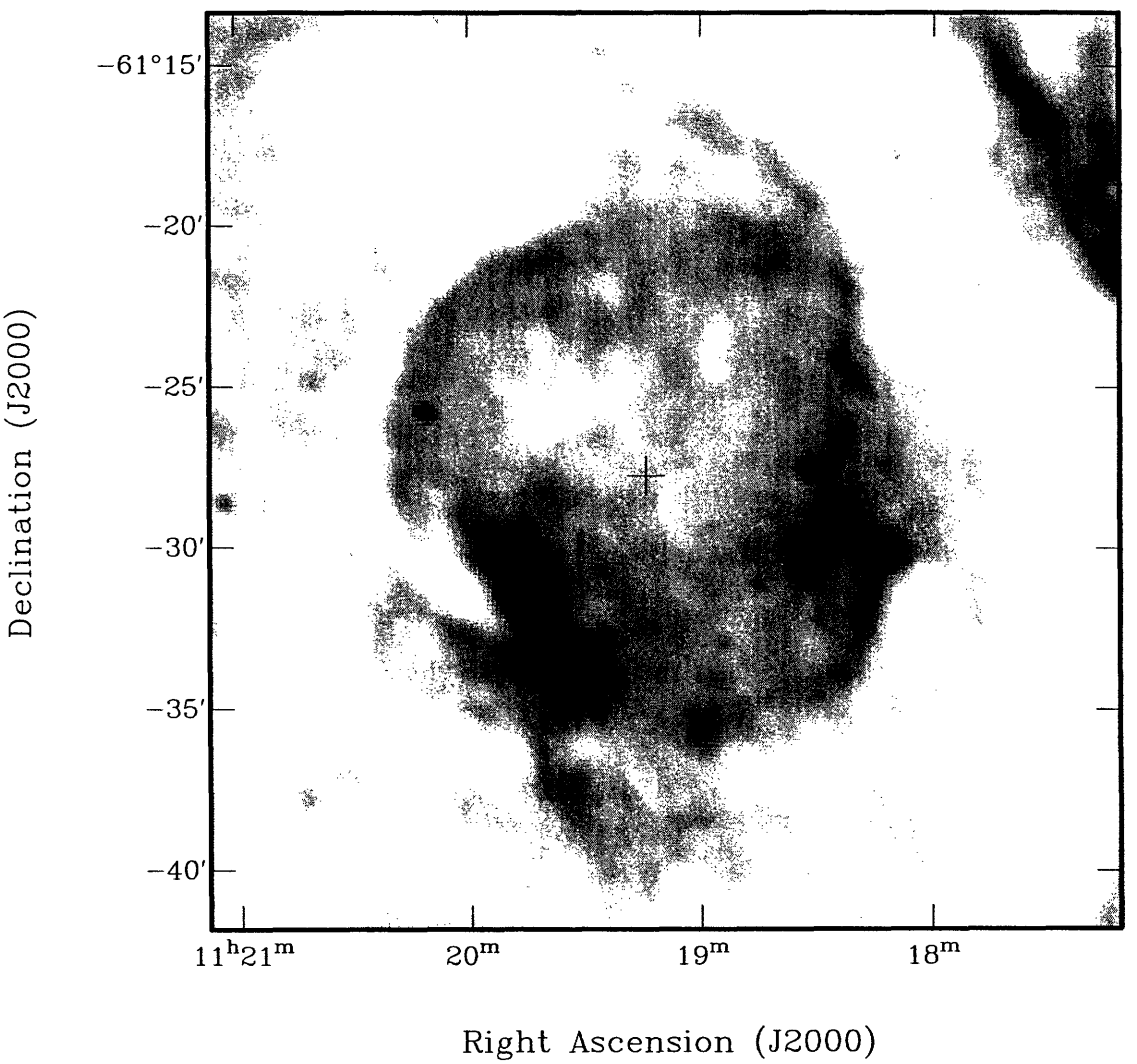

Figure 6-2 1.4-GHz ATCA total intensity map of the shell G292.2−0.5 made using u-v spacings less than 7.5 kλ from all array configurations. The beam size in the map is $29'' \times 25''$ and the rms noise level is $\sim$ 0.5 mJy. The position of PSR J1119−6127 determined from pulsar gating is indicated by the cross.

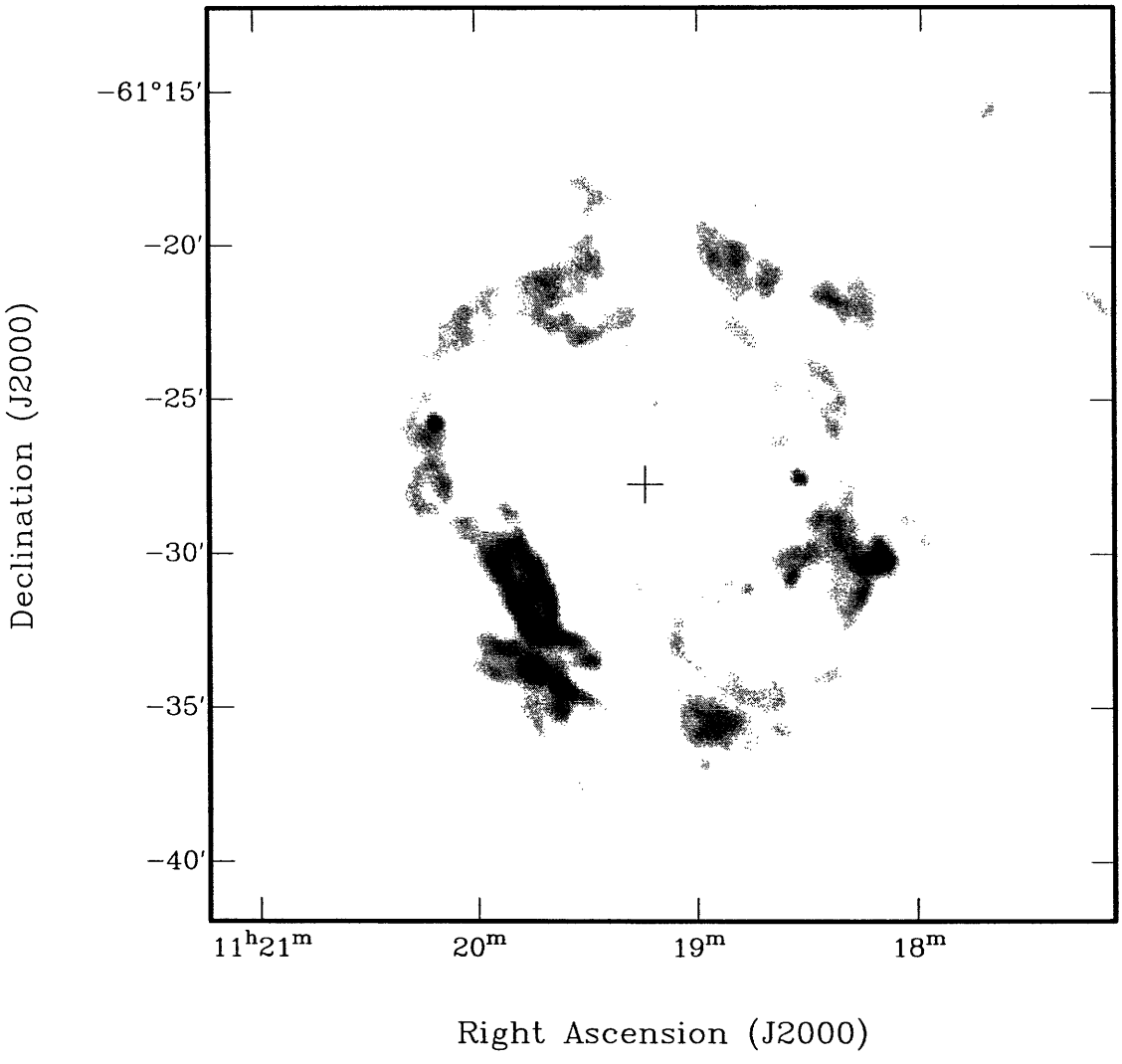

Figure 6-3 2.5-GHz ATCA total intensity map of the shell G292.2−0.5 made using u-v spacings between 0.5 kλ and 7.5 kλ from all array configurations. The beam size in the map is $21'' \times 20''$ and the rms noise level is $\sim$ 0.5 mJy. The position of PSR J1119−6127 determined from pulsar gating is indicated by the cross.

parameters as were used with the 2.5-GHz data to make the original 2.5-GHz map. Both this resulting map and the original 2.5-GHz map were then convolved with a Gaussian beam to yield a final beam resolution of 30″ in each case.

We then used a tomographic method (Katz-Stone & Rudnick 1997) to compare the brightest part of the shell G292.2−0.5 at the two frequencies to determine its spectral index. Specifically, a difference intensity map $I_{\rm tom}(\alpha_t)$ is made from the 1.4-GHz and 2.5-GHz maps ($I_{1.4}$ and $I_{2.5}$) assuming a trial spectral index α_t:

$$I_{\rm tom}(\alpha_t) = I_{1.4} - \left(\frac{\nu_{1.4}}{\nu_{2.5}}\right)^{\alpha_t} I_{2.5}. \tag{6.1}$$

Here $\nu_{1.4}$ and $\nu_{2.5}$ are 1.384 and 2.496 (the 1.4-GHz and 2.5-GHz center observing frequencies in GHz, respectively). When the correct spectral index α_t is tried, the feature in question blends into the background. An uncertainty in the estimated spectral index is obtained by adjusting this best-fit α_t until the feature becomes visible in either direction.

Figure 6-4 shows a series of tomographic maps made with trial spectral indices. Maps made with α_t ranging from 0.0 to −1.1 with step size 0.1 are shown, where α is defined according to $S \sim \nu^{\alpha}$. Light portions of the map indicate a more negative (steeper) spectral index for the feature than the one tried. The light coloring of the brightest part of the shell in the $\alpha_t = 0$ map clearly indicates a negative spectral index. We have estimated the spectral index of the shell to be $\alpha = -0.6 \pm 0.2$ by considering the range of α_t in which the features make the transition from light to dark.

6.3.3 Shell Polarimetry

Although the ATCA observations recorded the full Stokes parameters at both 1.4 GHz and 2.5 GHz, we could obtain no polarization information for the shell G292.2−0.5. This was due to the presence of the two bright extended HII regions (NGC 3603 and NGC 3576) in the vicinity. These sources introduced instrumental polarization leakages, the sidelobes from which swamped any polarization from the shell. This

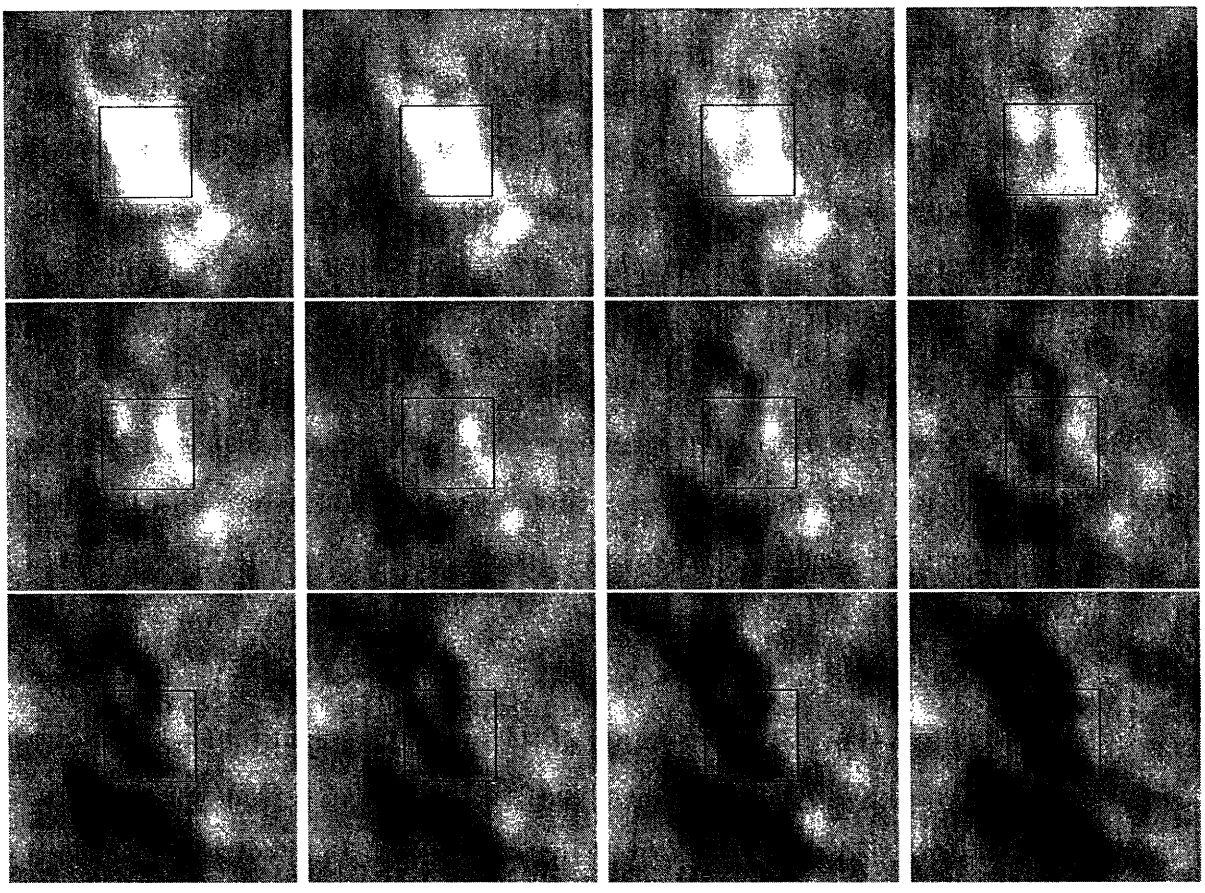

Figure 6-4 Tomographic spectral index maps for the shell SNR G292.2−0.5 made from 1.4-GHz and 2.5-GHz ATCA data. Only the brightest part of the shell is shown (located within the box) and is used to determine the spectral index. Trial spectral indices α_t ranging from 0.0 to −1.1, with step size 0.1, are shown going from top left to bottom right, where α is defined according to $S \sim \nu^{\alpha}$. Light and dark coloring indicate that a feature has a more negative (steeper) and more positive (more shallow) spectral indices, respectively, than the one tried in the difference map. The transition from light to dark within the box, which occurs around $\alpha_t \sim -0.6$, suggests a non-thermal synchrotron radiation mechanism, expected for a shell SNR.

polarization leakage could not be easily corrected for in the calibration since the contaminating sources were far from the pointing center of the observations.

6.3.4 Search for a Radio PWN in Off-pulse Maps

Using only the off-pulse data from the pulsar gating, we looked for an underlying PWN coincident with the position of PSR J1119−6127, which we have accurately established from pulsar gating (Chapter 5). Since there is a variety of spatial scales at which such emission could in principle be seen, we created a number of maps at both 1.4 GHz and 2.5 GHz with different spatial resolutions in order to search for a PWN with different sizes (Gaensler, Bock, & Stappers 2000).

For each data set, we subtracted a model of the radio emission (produced while making the total intensity maps) which included the emission external to the shell and emission from the shell itself. This reduced the interfering effects of sidelobes from bright extended sources and increased sensitivity to emission from within the shell near the location of the pulsar.

In order to adjust the spatial resolution of the maps, Gaussian tapers of variable size were applied to the u-v data by multiplying the data set by a Gaussian envelope. The taper size depended upon the spatial scale of interest, and corresponded to a convolution of the map with a Gaussian beam $\theta_{\rm taper}$ (which scaled inversely as the u-v taper size). All baselines were used in each case since there were no large gaps in the u-v coverage which would have resulted in pathological beam shapes. The modified u-v data sets were then inverted, deconvolved, and restored. We detected no obvious extended emission on any spatial scale in either the 1.4-GHz or 2.5-GHz data sets.

In order to quantify upper limits on the sensitivity from the non-detection of a PWN, we added model PWNe of varying sizes and flux densities to the u-v data at the pulsar location before mapping. Each model PWN consisted of a disk of diameter $\theta_{\rm PWN}$, which determined the Gaussian taper size $\theta_{\rm taper}$ (and hence the spatial resolution of the map) according to

$$\theta_{\rm taper} = \frac{2}{3}\theta_{\rm PWN}. \tag{6.2}$$

The beam size $\theta_{\rm beam}$ in the resulting map was determined by the beam size of the untapered u-v data $\theta_{\rm untapered}$ and $\theta_{\rm taper}$:

$$\theta^2_{\rm beam} \sim \theta^2_{\rm untapered} + \theta^2_{\rm taper}. \tag{6.3}$$

In most cases, the model PWN was slightly resolved in the image. However, in cases where $\theta_{\rm PWN} \lesssim \theta_{\rm beam}$, the PWN was unresolved. $\theta_{\rm untapered}$ was $\sim 6''$ and $\sim 4''$ for the 1.4-GHz and 2.5-GHz data sets respectively. By replacing $\theta_{\rm beam}$ in the inequality using Equations 6.2 and 6.3, and solving for $\theta_{\rm PWN}$, one can see that model PWNe smaller than $\sim 8''$ and $\sim 5''$ were unresolved in the images. The limit on the largest PWN size in the models was dictated by the smallest baseline used to make the maps (31 m). For each trial PWN size, the flux density of the model PWN was increased in steps until the PWN became plainly visible in the corresponding images. Each of these thresholds was then doubled in order to obtain a conservative upper limit on the flux density of any true PWN present.

Figure 6-5 shows a plot of the 1.4-GHz and 2.5-GHz surface brightness upper limits from our observations scaled to 1 GHz assuming a spectral index $\alpha = -0.3$, the canonical value measured for the Crab (Bietenholz et al. 1997). We obtained these limits using the modeling method described above. The observed size of the shell SNR G292.2−0.5 of $\sim 7'$ is indicated by the vertical line in Figure 6-5 and serves as a hard upper limit for the PWN size, since we do not expect a PWN to be larger than its associated shell.

6.4 G292.2−0.5: a New Shell Supernova Remnant

6.4.1 Shell Spectral Index

An important piece of evidence used to determine the nature of G292.2−0.5 as a shell SNR is its spectral index. Since the radio emission from a shell SNR stems from a

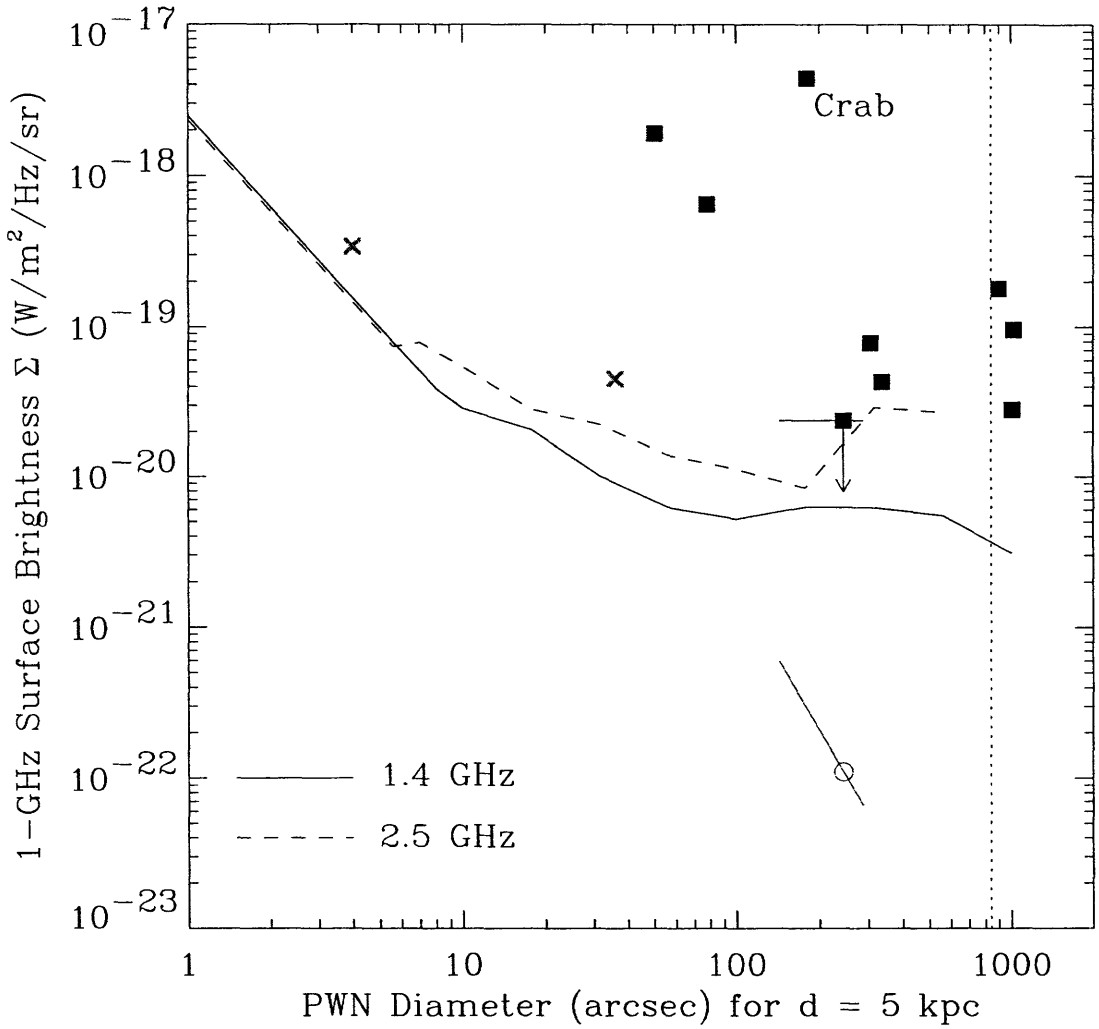

Figure 6-5 PWN surface brightness upper limits vs. PWN angular size for PSR J1119−6127 from 1.4 GHz and 2.5 GHz ATCA observations (solid and dashed lines respectively). Limits have been scaled to 1 GHz in both cases assuming a spectral index $\alpha = -0.3$, where α is defined according to $S \sim \nu^{\alpha}$. The dotted line represents the diameter of the shell SNR G292.2−0.5 and is a hard upper limit for the PWN size. The surface brightness value predicted for PSR J1119−6127 in the model (scaled using the Crab parameters in Table 6-4) is indicated by the open circle, with the error bar indicating sizes and surface brightnesses for the PWN for a range of expansion velocities between 1000 km/s and 2000 km/s (see text for details). Also plotted are the surface brightnesses for observed bow-shock and static PWNe (crosses and squares respectively), with all sizes scaled to a distance of 5 kpc. An observed surface brightness upper limit and a range of possible PWN sizes are also shown for MSH 15−52. The error bar here also assumes the same expansion velocity range as was assumed for PSR J1119−6127.

non-thermal synchrotron process, the emission is expected to have a negative spectral index close to $\alpha \sim -0.5$, where α is defined according to $S \sim \nu^{\alpha}$. On the other hand, an HII region or other thermal source has $\alpha \gtrsim 0$.

The results from the tomographic imaging of G292.2−0.5 clearly indicate a negative spectral index for all parts of the shell (Figure 6-4). We obtained an estimate of $\alpha = -0.6 \pm 0.2$ for the spectral index of the brightest part of the shell. This strongly suggests a non-thermal origin for the radio emission, as expected for a shell SNR.

Table 6-2 lists other known shell SNRs and their measured spectral indices (Green 1998 and references therein). The spectral index obtained for G292.2−0.5 is consistent with these other values. The youngest known SNR, SNR 1987A, has the steepest observed spectral index for any known SNR shell, with $\alpha = -0.95 \pm 0.04$ (Gaensler et al. 1997). The older SNRs in the list ($\tau > 1$ kyr) tend toward flatter values of $\alpha \sim -0.5$. The spectral index value obtained for G292.2−0.5 is consistent with these values.

6.4.2 Infrared Emission

An IRAS 60-μm map of the region[5] (shown in Figure 6-6) shows that there is no significant infrared emission coincident with the 1.4-GHz radio emission from G292.2−0.5, which is indicated by contours. The two HII regions, NGC 3603 and NGC 3576, which are located to the west of G292.2−0.5 have significant infrared emission, which is hinted at in Figure 6-6. There is a weak infrared source interior to the shell G292.2−0.5 which is close to (but not coincident with) PSR J1119−6127. This source has been identified as IRAS J11169−6111 (Pivovaroff 2000) and is not believed to be associated with the pulsar (Pivovaroff et al. 2000).

The lack of infrared emission coincident with G292.2−0.5 and the measured spectral index indicate that the emission from the shell G292.2−0.5 is non-thermal and that the emission mechanism is a synchrotron process. This is clear evidence that G292.2−0.5 is a previously undetected shell SNR.

[5]http://www.ipac.caltech.edu.

Table 6-2. Parameters of Young Shell SNRs from Type II SNe

SNR	Other Name	τ (kyr)	$R_{\rm shell}$[a] (pc)	$v_{\rm shell}$[b] (km/s)	α[c]	Ref.
1987A		0.01	~ 0.2	~ 18000	-0.95	1
G111.7−2.1	Cas A	0.3	2.04	6700	-0.77	2
G4.5+6.8	Kepler	0.4	1.92	4700	-0.64	2
0540−69.3		0.8	7.27	9100	-0.41	3
G320.4−1.2	MSH 15−5*2*	1.7	~ 20	~ 11500	-0.5	4
G292.2−0.5		1.7	10	5900	-0.6	5
G332.4−0.4	RCW 103	~ 2	~ 5	~ 2500	-0.5	2
G260.4−3.4	Puppis A	3.7	35.2	9300	-0.5	2

Entries ranked by age.

(1) Gaensler et al. (1997)

(2) Green (1998)

(3) Manchester, Staveley-Smith, & Kesteven (1993)

(4) Gaensler et al. (1999)

(5) This work

[a]Shell radius derived from shell angular diameter and estimated distance.

[b]Mean expansion velocity, obtained from $v_{\rm shell} = R_{\rm shell}/\tau$.

[c]Radio spectral index α of shell, defined according to $S \sim \nu^{\alpha}$.

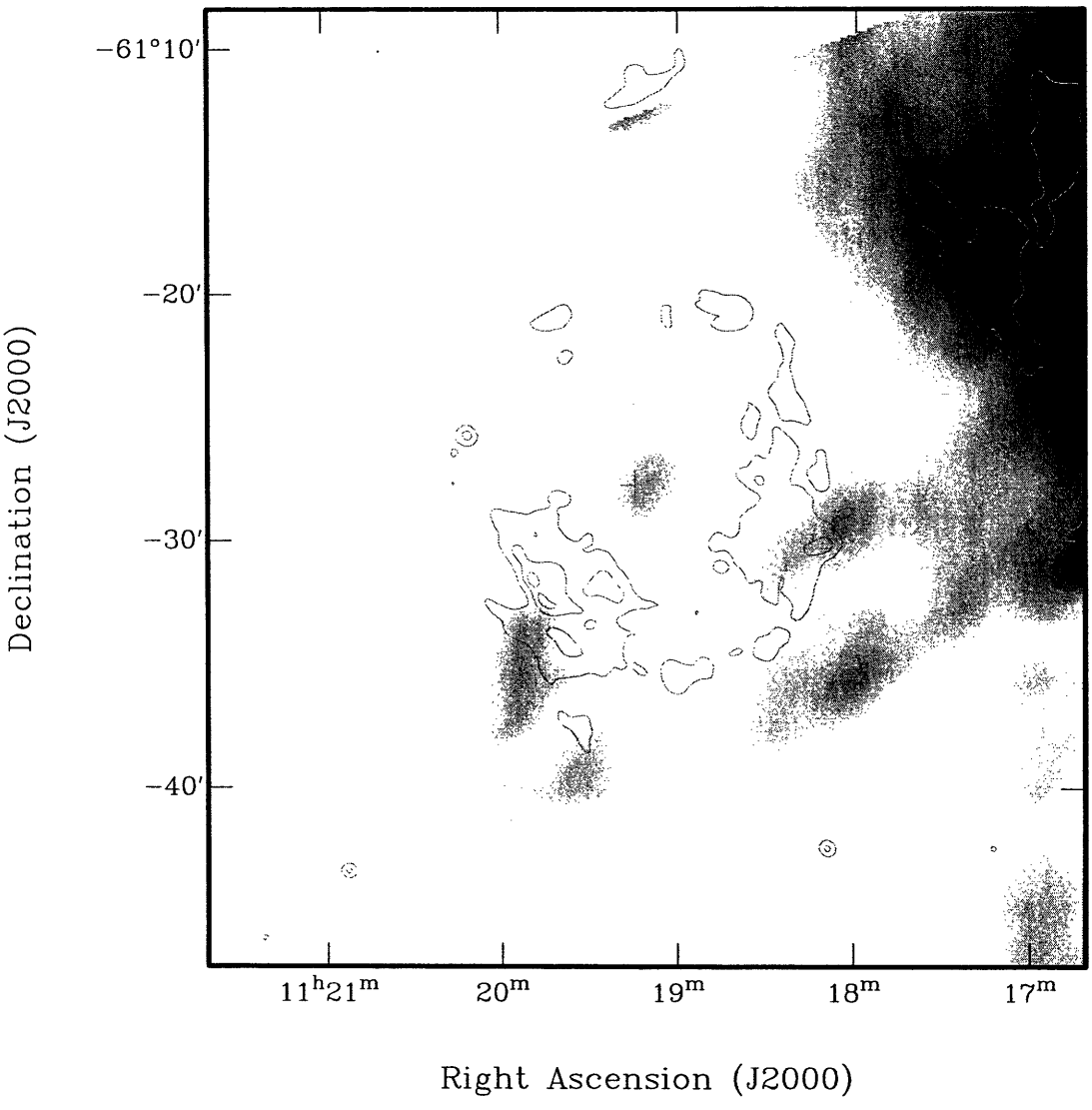

Figure 6-6 An IRAS 60-μm map of the region containing SNR G292.2−0.5 and PSR J1119−6127 (in grayscale) with 1.4-GHz ATCA radio emission overlaid in contours. There is negligible infrared emission associated with the radio shell, suggesting that the shell is a SNR and not a star-forming region. Significant infrared emission associated with the HII regions NGC 3603 and NGC 3576 is hinted at in the western part of the image. The infrared emission seen near the position of PSR J1119−6127 (which is indicated by the cross) has been identified as IRAS J11169−6111, and is not associated with the pulsar. The cutoff in the IRAS grayscale emission in the upper-left part of the image is the border of the IRAS map.

6.5 Evidence for Association with PSR J1119−6127

6.5.1 Shell Morphology and Pulsar Location

Figures 6-2 and 6-3 show that SNR G292.2−0.5 has a circular morphology with a radius $\sim 7'$. This circular morphology is what is expected for a young shell SNR which has not yet become significantly deformed by the clumpy interstellar medium (ISM). Other young SNR shells (e.g., Cas A, Kepler) also show this morphology. The location of PSR J1119−6127, determined from gating, indicates that the pulsar lies at the projected center of SNR G292.2−0.5. This spatial coincidence and the young age of both objects suggest that the two are associated.

6.5.2 Shell Size and Inferred Expansion Velocity

Next we consider whether the shell size is consistent with its being a SNR. For PSR J1119−6127, the implied distance from the DM-distance model of the Galactic electron distribution is $d > 30$ kpc (Taylor & Cordes 1993). However, this model does not account for individual HII regions, and, because the pulsar lies in the direction of the Carina spiral arm with the likely presence of nearby ionizing population I stars, this distance is assuredly a gross overestimate. It is more likely that the pulsar is located between the two crossings of the line of sight to the pulsar with the Carina spiral arm at Galactic longitude $l = 292°$ (Figure 6-7). These crossings are located at distances of 2.4 kpc and 8 kpc, and the Carina arm remains close to the line of sight between these points. We therefore assume that a realistic distance to SNR G292.2−0.5 is 2.4 kpc $< d_{\rm shell} <$ 8 kpc, assuming that it is associated with PSR J1119−6127. We use a distance of 5 kpc in subsequent parameterized expressions. From this distance estimate and the measured angular size of the shell, we obtain a shell radius $R_{\rm shell}$ of

$$R_{\rm shell} \sim 10.2 \left(\frac{d_{\rm shell}}{5 \text{ kpc}} \right) \text{pc}. \tag{6.4}$$

For a lifetime of 1.7 kyr (the estimated age of the pulsar), the shell expansion velocity (assuming free expansion) is

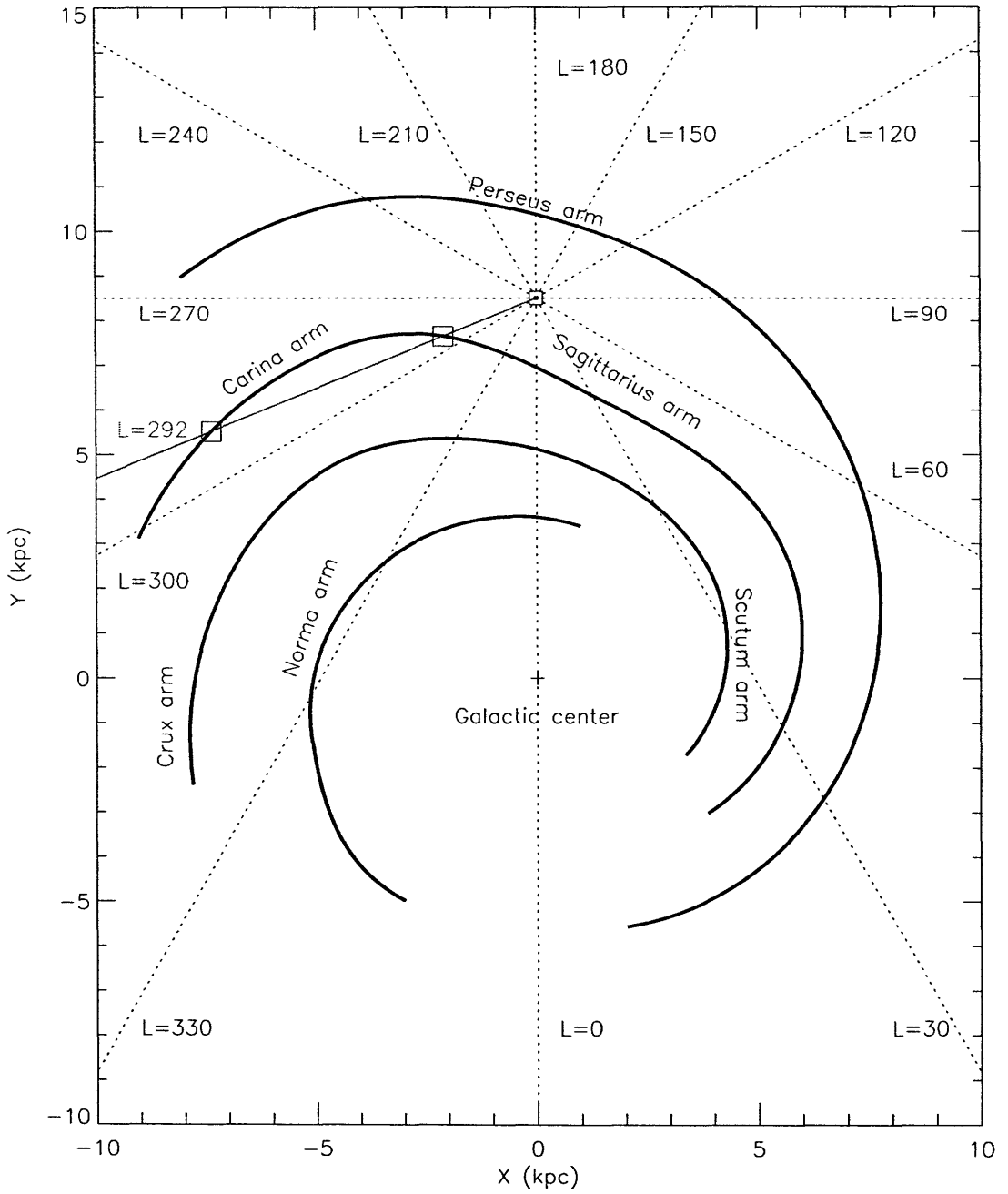

Figure 6-7 Locations of the spiral arms in the Galaxy (dark lines). The line of sight from Earth to PSR J1119−6127 is shown by the $l = 292°$ line. The two crossing points of this line with the Carina spiral arm at a distance of 2.4 kpc and 8 kpc are indicated by the open squares.

$$v_{\rm shell} \sim 5900 \left(\frac{d_{\rm shell}}{5 \text{ kpc}}\right) \left(\frac{1.7 \text{ kyr}}{\tau}\right) \text{km/s}. \quad (6.5)$$

This radius and velocity estimate for SNR G292.2−0.5 is comparable to estimates for other shell SNRs of a similar age which originated in Type II SNe (Table 6-2). Thus, the size estimate and inferred expansion velocity for the shell SNR G292.2−0.5 are consistent with the interpretation that it is associated with PSR J1119−6127.

6.5.3 Summary

The measured spectral index for the shell G292.2−0.5 from our observations is $\alpha = -0.6 \pm 0.2$ and implies that the radio emission mechanism is non-thermal. This is expected for a shell SNR, and the spectral index is consistent with that observed for other young SNRs. The spectral index, combined with the absence of infrared emission, indicates that the shell is a previously undiscovered radio SNR. The circular morphology of SNR G292.2−0.5 and the spatial location of PSR J1119−6127 at the center of the shell both suggest that the SNR is associated with the young pulsar. The size and inferred expansion velocity of the shell, if the two objects are associated, are both comparable to other young shell SNRs, supporting the association. We conclude that G292.2−0.5 is a previously undiscovered shell SNR associated with the young pulsar PSR J1119−6127.

6.6 Implications of the Absence of an Observable PWN

6.6.1 The Crab Paradigm

The Crab pulsar and its nebula have been traditionally considered to be the prototypical young pulsar system. In this paradigm, young pulsars with $\tau < 2$ kyr are believed to be rapidly spinning ($P \lesssim 50$ ms) and powering radio PWNe through the interaction of the pulsar wind with the ambient medium. This is the case for the

Crab, PSR J0540−6919, and PSR J0537−6910, three of the young pulsars listed in Table 6-1 which are rapidly spinning and which power observable PWNe.

However, two other young pulsars, PSRs J1513−5908 and J1119−6127, are of a comparable age ($\tau < 2$ kyr) but spin much more slowly ($P \sim 150$ ms and 408 ms respectively). These pulsars have much higher magnetic field strengths than the others (see Table 6-1), and therefore have undergone significant slowdown to long periods from magnetic braking early in their lives. Given that these two long-period, high-magnetic-field pulsars have different evolutionary histories than the three Crab-like pulsars mentioned above, it is not clear that the Crab paradigm is correct or is even the most common kind of young pulsar system. In fact, no obvious radio PWN has been detected around PSR J1513−5908 (Gaensler et al. 1999), though upper limits from these observations are poor due to the complicated nature of the region. PSR J1119−6127 is in a less complicated field and has a larger magnetic field than PSR J1513−5908, and therefore is potentially a better system with which to test the predictions of physical models of the evolutionary history of high-magnetic-field pulsars and their associated PWNe.

6.6.2 Observed Upper Limits and Known Radio PWNe

From our ATCA observations at 1.4 GHz and 2.5 GHz, we detected no PWN around PSR J1119−6127 on any angular scale. The upper limits for the PWN surface brightness for both the 1.4-GHz and 2.5-GHz data are shown in Figure 6-5. These limits have been scaled to a 1-GHz surface brightness assuming a spectral index of $\alpha = -0.3$. Also plotted in Figure 6-5 is the 1-GHz surface brightness for a representative sample of observed radio PWNe, including two bow-shock PWNe. Bow-shock nebulae arise when the velocity of the pulsar exceeds the expansion velocity of the PWN and a shock front is formed (Frail & Scharringhausen 1997). Otherwise the PWN is called static. In Figure 6-5, the angular size of each PWN has been scaled to a distance of 5 kpc, the nominal distance assumed for PSR J1119−6127. Each of the PWNe plotted in Figure 6-5 would have been easily detectable in our observations at the 5 kpc distance we have estimated for SNR G292.2−0.5. In the case of PSR J1513−5908, the

other young high-magnetic-field pulsar listed in Table 6-1, only an upper limit is plotted, which was derived from surface brightness limits presented elsewhere (Gaensler et al. 1999). An error bar in the angular size for this PWN accounts for the unknown expansion velocity of the PWN, which we assume to range between 1000 km/s and 2000 km/s, with a nominal value equal to that of the Crab, $v \sim 1700$ km/s (Trimble 1968). The upper limits on this PWN are not particularly stringent. The surface brightness limits obtained here for PSR J1119−6127 are significantly better and can be used to test models of PWN evolution.

6.6.3 An Evolutionary Model of PWNe

This apparent discrepancy between Crab-like and long-period, high-magnetic-field young pulsars can be reconciled in a model of pulsar and PWN evolution proposed by Bhattacharya (1990). Qualitatively, this model suggests that a high-magnetic-field pulsar is born spinning rapidly, but quickly slows down to a much larger period due to strong magnetic braking. This effectively injects a large amount of the pulsar's spin-down energy into the PWN at the very early stages of its evolution, at which time the PWN is very small and bright. As the nebula expands and the pulsar can no longer inject energy into it, the PWN experiences significant losses from expansion into the ambient medium. The nebula undergoes a rapid decay in luminosity and becomes undetectable early in its lifetime. The net energy loss rate of the nebula $\dot{E}_{\rm PWN}$ can be modeled as the difference between the energy injection rate from the pulsar $\dot{E}_{\rm psr}$ and the energy loss rate from expansion $\dot{E}_{\rm expansion}$.

The rate of energy loss from the pulsar as a function of time t, assuming magnetic dipole radiation, is (Pacini & Salvati 1973; Weiler & Panagia 1980)

$$\dot{E}_{\rm psr} = \frac{L_0}{(1 + t/\tau_0)^2}, \tag{6.6}$$

where $L_0 \equiv 4\pi^2 I \dot{P}_0 / P_0^3$ is the initial energy loss rate of the pulsar and $\tau_0 \equiv P_0/2\dot{P}_0$. Here P_0 and $\dot{P}_0$ are the period and period derivative of the pulsar at birth. The energy loss rate $\dot{E}_{\rm expansion}$ from the expansion of the nebula as a function of time t (assuming

uniform expansion in time) is

$$\dot{E}_{\rm expansion} = -\frac{E_{\rm PWN}}{t}, \tag{6.7}$$

where $E_{\rm PWN}$ is the energy contained in the PWN. These equations can be combined to obtain an expression for the evolution of the energy of the PWN as a function of time:

$$\dot{E}_{\rm PWN} = -\frac{E_{\rm PWN}}{t} + \frac{L_0}{(1+t/\tau_0)^2}. \tag{6.8}$$

With the assumption that the particles in the nebula have an energy distribution described by a power law γ and by assuming equipartition between the energy contained in the magnetic field and the energy contained in particles, the evolution of the synchrotron luminosity can be calculated.

The luminosity evolution at a given frequency is divided into two stages. In the first stage ($t < \tau_0$), the pulsar continues to power the nebula as it expands. In this stage the luminosity decreases with time t as $L \sim t^{\alpha}$, where α is related to the power law γ of particle energies according to $\gamma = 1 - 2\alpha$ (Reynolds & Chevalier 1984). The decrease in luminosity is from the expansion, despite the fact that the pulsar continues to inject energy into the nebula. In the second stage ($t > \tau_0$), the pulsar has transferred the bulk of its energy into the nebula and can no longer inject energy and power it. In this stage, the nebular luminosity decreases more steeply as the pulsar expands, with $L \sim t^{-2\gamma}$.

These equations for the luminosity evolution of the nebula in time can be combined to obtain the luminosity at a given frequency for any age $t > \tau_0$:

$$L = L^i \tau_0^{\alpha} \left(\frac{t}{\tau_0}\right)^{-2\gamma}, \tag{6.9}$$

where L^i is the luminosity of the pulsar at a given radio frequency at birth.

The pulsars which are of interest here are in the second phase of luminosity evolution ($t > \tau_0$). The ratio of the luminosities L_1 and L_2 of pulsars with ages t_1 and t_2 respectively at a given radio frequency is then given by

$$\frac{L_1}{L_2} = \frac{L_1^i}{L_2^i}\left(\frac{\tau_1}{\tau_2}\right)^{2\gamma+\alpha}\left(\frac{t_1}{t_2}\right)^{-2\gamma}, \tag{6.10}$$

where τ_1 and τ_2 are the transition times τ_0 for the two systems.

Using the definition of τ_0 and the relation for the initial surface magnetic field, $B_0 \sim \sqrt{P_0\dot{P}_0}$, we rewrite the τ_0 dependence as $\tau_0 \sim P_0^2/B_0^2$. Substituting for α using $\gamma = 1 - 2\alpha$ in the luminosity ratio yields

$$\frac{L_1}{L_2} = \frac{L_1^i}{L_2^i}\left(\frac{P_1}{P_2}\right)^{3\gamma+1}\left(\frac{B_1}{B_2}\right)^{-3\gamma-1}\left(\frac{t_1}{t_2}\right)^{-2\gamma}, \tag{6.11}$$

where P and B are the initial period and magnetic field for the two pulsars.

In the model of the luminosity evolution described here, there are two components to the expanding ejecta from the supernova (SN). The fast-moving ejecta are responsible for the shell emission (which is not discussed here). The more slowly moving component of the ejecta affects the luminosity evolution of the PWN. The initial luminosity L^i of a PWN scales as a factor involving L_0 and the expansion velocity v of the slowly moving ejecta. This scale factor is (Reynolds & Chevalier 1984)

$$L^i \sim L_0^{(\gamma+11)/10} v^{-9(\gamma+1)/20}. \tag{6.12}$$

There is also a dependence for L^i on the mass of the ejecta. However, this is unknown and is assumed to be equal. Other constants have also been ignored since we are only considering the ratio of the luminosities. We rewrite the expression for L_0 in terms of B_0 to obtain $L_0 \sim B_0^2/P_0^4$ and get

$$L^i \sim P_0^{-2(\gamma+11)/5} B_0^{(\gamma+11)/5} v^{-9(\gamma+1)/20}. \tag{6.13}$$

The ratio of the PWN luminosities can then be written as

$$\frac{L_1}{L_2} = \left(\frac{P_1}{P_2}\right)^{(13\gamma-17)/5}\left(\frac{B_1}{B_2}\right)^{(-14\gamma+6)/5}\left(\frac{v_1}{v_2}\right)^{-9(\gamma+1)/20}\left(\frac{t_1}{t_2}\right)^{-2\gamma}. \tag{6.14}$$

The surface brightness Σ scales inversely as the projected area of the PWN, or equivalently as the inverse square of the radius of the PWN:

$$\Sigma \sim \frac{L}{R_{\rm PWN}^2}. \tag{6.15}$$

We can substitute for $R_{\rm PWN}$ using the relation $R_{\rm PWN} = vt$. This reasonably assumes that the PWN ejecta are still freely expanding. Substituting in a value of $\gamma = 1.6$ (from the canonical value of $\alpha = -0.3$), the ratio of surface brightnesses for two PWNe with different ages can be written

$$\frac{\Sigma_1}{\Sigma_2} = \left(\frac{P_1}{P_2}\right)^{+0.76} \left(\frac{B_1}{B_2}\right)^{-3.28} \left(\frac{v_1}{v_2}\right)^{-3.17} \left(\frac{t_1}{t_2}\right)^{-5.2}. \tag{6.16}$$

We use this expression to predict the expected surface brightness for PSR J1119−6127 by scaling from the parameters for the Crab nebula.

6.6.4 Model Prediction for PSR J1119−6127

Since the parameters for the Crab nebula are the best-known for any PWN observed, we scale the observed surface brightness of the Crab (listed in Table 6-3) using parameters for the Crab pulsar and PSR J1119−6127 (listed in Table 6-4) and Equation 6.16. Note that the weak dependence in Equation 6.16 on the initial period means that it is not as critical a parameter as, e.g., the initial surface magnetic field strength. Varying P_0 by an order of magnitude in the model while holding everything else constant only changes the ratio by a factor of a few.

From this scaling we obtain a predicted model surface brightness which we compare with our observed upper limits and with the surface brightness of observed PWNe. We find that the 1-GHz surface brightness predicted for a PWN powered by PSR J1119−6127 is $\Sigma \simeq 1.1 \times 10^{-22}$ W/m^2/Hz/sr. The predicted size of the PWN is determined by the PWN expansion velocity v and the distance to the system. Figure 6-5 shows this predicted surface brightness with an error bar corresponding to velocities between 1000 km/s and 2000 km/s. We have assumed a nominal expansion velocity for the PWN of $v \sim 1700$ km/s, the value observed for the Crab (Trimble 1968). The expansion velocity of the PWN not only affects the initial luminosity of the PWN, but also affects the PWN size. These two effects lead to a strong dependence

Table 6-3. Sizes and Surface Brightnesses of Known PWNe

SNR	Other Name	$d_{\rm PWN}$ (kpc)	$\theta_{\rm PWN}$ (arcmin)	$S^{\rm a}$ (Jy)	$\log \Sigma^{\rm b}$
G184.6−5.8	Crab	2.5	6	1040	−17.4
0540−69.3		50	0.084	0.09	−17.7
G21.5−0.9		5.5	1.2	6	−18.2
G5.4−1.2[c]	Duck	5	0.067	0.01	−18.5
0538−69.1	N157B	50	1.5	2.75	−18.7
G328.4+0.2	MSH 15−57	17	5	16	−19.0
G130.7+3.1	3C58	3.2	8	33	−19.1
G34.7−0.4[c]	W44	3	1	0.3	−19.4
G326.3−1.8	MSH 15−56	4	7	14	−19.4
G74.9+1.2	CTB87	12	7	9	−19.6
G320.4−1.2	MSH 15−52	5.2	3.9[d]		< -19.6[e]
G292.2−0.5		5	4.07[d]		−22.0[f]

Data from Green (1998) and references therein.

[a]1-GHz flux density of PWN.

[b]1-GHz surface brightness of PWN in units of W/m^2/Hz/sr.

[c]Bow-shock nebula.

[d]Assumes Crab expansion velocity ($v \sim 1700$ km/s) and age $\tau \sim 1.7$ kyr (PWN not observed).

[e]Upper limits from Gaensler et al. (1999) (PWN not observed).

[f]Model prediction, scaled using Crab parameters (PWN not observed).

of the surface brightness dependence in the model on the expansion velocity (Equation 6.16). A velocity of $v \lesssim 500$ km/s would be required for the model prediction to contradict the observed upper limits.

6.6.5 Comparison with Observations

Figure 6-5 clearly shows that the predicted surface brightness for a PWN powered by PSR J1119−6127 is significantly lower than that observed for any of the PWNe plotted and that our upper limits on the emission are consistent with this model prediction. The surface brightness upper limits we have set for PSR J1119−6127 are much better than those for PSR J1513−5908, the other young high-magnetic-field pulsar. Until the discovery of PSR J1119−6127, PSR J1513−5908 was the best known example of such a pulsar and was the best example with which to test the evolutionary model outlined here. The fact that neither of these young, high-magnetic-field pulsars powers an observable radio PWNe supports the model of Bhattacharya (1990), which predicts that these PWNe should be significantly fainter than other observed PWNe.

6.7 Conclusions

From ATCA radio imaging observations taken at 1.4 GHz and 2.5 GHz, we have discovered a new radio shell, G292.2−0.5, and have determined that it is a shell SNR associated with the 1.7 kyr-old high-magnetic-field pulsar PSR J1119−6127. The measured spectral index for the brightest part of the shell, $\alpha = -0.6 \pm 0.2$, where α is defined according to $S \sim \nu^{\alpha}$, suggests a non-thermal origin for the radio emission (expected for a SNR) and is close to observed values for other shell SNRs. The shell morphology, size, and pulsar location all suggest that the SNR is associated with the pulsar.

No pulsar-powered PWN was detected in our observations, and we have established upper limits for the surface brightness of a PWN powered by PSR J1119−6127. The presence of a 1.7 kyr-old high-magnetic-field pulsar with no observable PWN can be accounted for in a model in which the pulsar spins down rapidly to long periods

and dumps the bulk of its energy into the PWN at early times. The energy losses from expansion after the energy has been injected from the pulsar cause the nebula to fade quickly. Our observations would have detected other known radio PWNe at a distance of 5 kpc, the distance we have assumed for PSR J1119−6127. Our upper limits support a model of PWN luminosity evolution (Bhattacharya 1990) which predicts a low surface brightness for the PWN associated with PSR J1119−6127.

It has been estimated that $\sim$ 85% of SNe come from massive progenitors (Tammann, Löffler, & Schröder 1994), and that a large fraction of these should produce pulsars. However, few associations between pulsars and SNRs have been convincingly established (Kaspi 1998). The fact that neither PSR J1513−5908 nor PSR J1119−6127, the two young ($\tau < 2$ kyr) high-magnetic-field radio pulsars which are currently known, powers an observable radio PWN may help explain the apparent absence of pulsars associated with young shell SNRs. In some of these cases, a PWN powered by a high-magnetic-field radio pulsar could be too faint to be detected. Such a pulsar would not be indirectly observable through radio imaging. If the radio beam from such a pulsar were too faint to be detected or did not intersect our line of sight, X-ray observations could be the only way to detect its presence.

Although this explanation may well account for the absence of PWNe in young shell SNRs, whether it can account for all of them can only be answered by detailed population synthesis modeling to determine whether the properties of the entire pulsar population are consistent with the existence of a much larger population of young high-magnetic-field pulsars than has been previously supposed. This modeling is beyond the scope of this thesis and is future work to be done by others.

Table 6-4. PWN Brightness Scaling Parameters

Parameter	Crab	PSR J1119−6127
Initial pulsar spin period, P_0	16 ms[a]	16 ms[a]
Initial surface magnetic field, B_0	3.8 $\times 10^{12}$ G[b]	4.1 $\times 10^{13}$ G[b]
Pulsar age, t	1.0 kyr[b]	1.7 kyr[b]
PWN expansion velocity, v	1700 km/s[b]	1700 km/s[a]

[a]Assumed model parameter.

[b]Observed parameter.

Appendix A

A Search for Sub-millisecond Pulsations from Unidentified FIRST and NVSS Radio Sources

This chapter is a modified self-contained paper titled, "A Search for Sub-millisecond Pulsations from Unidentified FIRST and NVSS Radio Sources," which has been published in the *Astronomical Journal* (Crawford, Kaspi, & Bell 2000).

We have searched 92 unidentified sources from the FIRST and NVSS 1400-MHz radio survey catalogs for radio pulsations at 610 MHz. The selected radio sources are bright, have no identification with extragalactic objects, are point-like and are more than 5% linearly polarized. Our search was sensitive to sub-millisecond pulsations from pulsars with dispersion measures (DMs) less than ~ 500 pc cm^{-3} in the absence of scattering. We have detected no pulsations from these sources and consider possible effects which might prevent detection. We conclude that as a population, these sources are unlikely to be pulsars.

A.1 Introduction

The FIRST survey (Faint Images of the Radio Sky at Twenty Centimeters) and NVSS survey (NRAO VLA Sky Survey) are recent 1400-MHz VLA radio surveys of

the Northern sky. The FIRST survey is an ongoing survey of the North and South Galactic caps using the VLA in B-configuration with a synthesized beam size of 5.4″ (Becker, White, & Helfand 1995). In the published FIRST catalog of radio sources from the first two observing sessions in 1993 and 1994 (White et al. 1997), 1550 square degrees of the North Galactic cap were covered spanning $7^h < \alpha(\mathrm{J2000}) < 18^h$ and $+28° < \delta(\mathrm{J2000}) < +42°$. The positions and flux densities of $\sim 1.4 \times 10^5$ discrete radio sources[1] are complete down to a flux density of ~ 1 mJy. The NVSS survey (Condon et al. 1998) covers $\delta > -40°$ (covering 82% of the celestial sphere) and catalogs more than 1.8×10^6 sources complete down to a flux density of ~ 2.5 mJy. The NVSS survey was conducted with the VLA in D and DnC configurations with a synthesized beam size of 45″. The NVSS survey also preserves polarization information.

Several large-scale pulsar surveys have previously been conducted at high Galactic latitudes (see Camilo 1997 and references therein). However, the rates at which the received analog power was sampled and digitized in these surveys, typically 3-4 kHz, and the low observing radio frequencies ($\sim$ 400 MHz), combined with relatively large radio frequency channel bandwidths of between 125 kHz and 1 MHz, restricted their sensitivity to sub-millisecond pulsars to very small dispersion measures (DMs) (DM $\lesssim$ 10 pc cm^{-3}). Large-scale surveys that maintain sensitivity to sub-millisecond periodicities over a wide range of DMs are difficult: the fast sampling rate and small radio frequency channel bandwidth required make large total bandwidths and long integration times currently impractical. However, a targeted search for sub-millisecond pulsations is possible using narrow frequency channels and a fast sampling rate. Such a survey is of course also sensitive to long-period pulsars which may have been missed in previous surveys due to radio frequency interference (RFI) or scintillation.

Consideration of the properties of known recycled pulsars and representative models of magnetic field decay and equations of state suggests that a significant population of sub-millisecond pulsars could be present in the Galaxy (e.g., Possenti et al.

[1]The online catalog is updated regularly as observing proceeds and currently contains more than 5.4×10^5 sources derived from data taken from 1993 to 1998 (99Jul21 catalog version, http://sundog.stsci.edu/first/catalogs.html).

1998). It is possible, therefore, that some of the sources which remain unidentified in radio survey catalogs could be bright sub-millisecond radio pulsars which have previously escaped detection in high-latitude pulsar surveys. To date, no pulsar has been found with a period shorter than that of the first millisecond pulsar discovered, PSR J1939+2134 (B1937+21), which has a 1.56-ms period (Backer et al. 1982). The discovery of a sub-millisecond pulsar would place important constraints on the equation of state of neutron star matter at high densities (e.g., Kulkarni 1992).

A.2 Target Choice and Observations

The FIRST and NVSS surveys contain a number of bright sources which are unresolved and have no identification in other wavebands. Although over 99% of bright sources ($S_{1400} > 60$ mJy) found in previous large-scale surveys are believed to be active galactic nuclei (AGN) (Condon et al. 1998), many sources in the FIRST and NVSS catalogs remain unidentified. One possibility is that they are previously unrecognized radio pulsars. Since pulsars often have a high degree of linear polarization (Lyne & Manchester 1988), polarized sources are good targets for pulsar searches. Han & Tian (1999) have identified 97 objects in the NVSS catalog which are coincident with known pulsars. Of the 89 redetected pulsars in Table 1 of their paper for which the degree of linear polarization could be determined from the NVSS observations, only 8 had an observed nominal fractional linear polarization less than 5%. The intrinsic degree of polarization of these pulsars may even be higher if bandwidth depolarization effects are significant, in which case an even higher fraction of the pulsar sample is more than 5% linearly polarized. Figure 2 of Han & Tian (1999) shows that only $\sim$ 10% of identified quasars and $\sim$ 10% of BL-Lac objects are more than 5% linearly polarized. Thus, although there is not a clear polarization cutoff separating the pulsar and extragalactic populations, a polarization threshold of 5% excludes most ($\sim$ 90%) of the identified non-pulsar population while retaining the majority ($\sim$ 90%) of the identified pulsar population.

We have searched for radio pulsations in bright ($S_{1400} \geq 15$ mJy) point-like uniden-

tified sources from the FIRST and NVSS survey catalogs which are more than 5% linearly polarized at 1400 MHz. Sources were selected directly from the catalogs if they met certain criteria.

Unidentified FIRST sources had their flux densities checked against their corresponding NVSS flux densities. If a source was extended, the better resolution of the FIRST survey would be expected to yield a lower flux density for the source than the NVSS survey. Therefore, in order to eliminate extended objects, sources were only included if their FIRST and NVSS flux densities agreed to within a few percent (indicating an unresolved non-variable source) or if the FIRST flux density exceeded the NVSS flux density (indicating an unresolved scintillating source). The large number of extended sources in the catalogs makes this filter necessary, though it does unfortunately eliminate scintillating sources which happen to be fainter in the FIRST survey.

For unresolved NVSS sources outside of the FIRST survey region, pointed VLA observations were undertaken in October 1995 in B-configuration in order to obtain the same angular resolution (5.4″) as the FIRST survey (R. Becker & D. Helfand, unpublished work). Sources in these observations were then subjected to the selection criteria described above. A total of 92 objects from the catalogs (39 appearing in both FIRST and NVSS, and 53 appearing only in NVSS) fit our selection criteria and were sufficiently far north to be observed in our search. The positions, NVSS total intensity peak flux densities, and fractional linear polarization from the NVSS peak flux density values are listed for the selected sources in Tables A-1 and A-2.

Each of the 92 unidentified sources was observed at a center frequency of 610 MHz in two orthogonal linear polarizations for 420 s with the Lovell 76-meter telescope at Jodrell Bank, UK. A total bandwidth of 1 MHz was split into 32 frequency channels with detected signals from each channel added in polarization pairs and recorded on Exabyte tape as a continuous one-bit digitized time series sampled at 50 μs. The minimum detectable flux density of periodicities in a pulsar search depends upon the raw sensitivity of the system and a number of propagation and instrumental effects (Chapter 2; see also, e.g., Dewey et al. 1985). Interstellar dispersion contributes to

Table A-1. Positions of Observed FIRST/NVSS Sources

Source	α (J2000) (hh:mm:ss.sss)	δ (J2000) (dd:mm:ss.ss)	Source	α (J2000) (hh:mm:ss.sss)	δ (J2000) (dd:mm:ss.ss)
0002−1952	00:02:40.965	−19:52:52.43	0755+3013	07:55:01.887	+30:13:46.68
0004−1148	00:04:04.905	−11:48:58.52	0755+3341	07:55:36.599	+33:41:56.27
0011−2254	00:11:09.912	−22:54:58.64	0757+2721	07:57:52.648	+27:21:07.62
0014−2800	00:14:44.065	−28:00:47.39	0758+3929	07:58:08.846	+39:29:28.61
0023−2155	00:23:30.215	−21:55:37.73	0802+3122	08:02:12.783	+31:22:40.56
0024+0308	00:24:49.369	+03:08:34.65	0805+2737	08:05:19.023	+27:37:35.99
0026−1112	00:26:51.454	−11:12:52.57	0806+3310	08:06:01.704	+33:10:10.16
0027−3030	00:27:02.074	−30:30:32.16	0810+3034	08:10:40.249	+30:34:32.99
0032−2649	00:32:33.032	−26:49:17.70	0840+2923	08:40:30.750	+29:23:32.57
0037−2323	00:37:08.808	−23:23:40.65	0843+3738	08:43:08.663	+37:38:16.42
0040+1329	00:40:21.805	+13:29:37.72	0844+3629	08:44:56.087	+36:29:27.64
0051+0229	00:51:51.304	+02:29:44.11	0846+3746	08:46:47.432	+37:46:14.97
0054−1754	00:54:10.786	−17:54:13.32	0903+3523	09:03:05.211	+35:23:18.91
0057+1341	00:57:36.448	+13:41:45.24	0911+3349	09:11:47.745	+33:49:16.60
0107−1211	01:07:11.786	−12:11:23.96	0923+3011	09:23:30.450	+30:11:10.92
0114−3219	01:14:48.887	−32:19:51.76	0928+4142	09:28:22.186	+41:42:21.77
0138−2954	01:38:40.505	−29:54:46.04	0944+3803	09:44:59.202	+38:03:17.34
0146+0222	01:46:14.619	+02:22:08.16	1000+3718	10:00:21.815	+37:18:44.99
0147+0715	01:47:27.777	+07:15:02.82	1003+3244	10:03:57.560	+32:44:02.87
0154−2422	01:54:56.898	−24:22:33.61	1013+3445	10:13:49.574	+34:45:50.74
0214+1027	02:14:59.232	+10:27:48.65	1033+2851	10:33:19.483	+28:51:22.16
0217−2354	02:17:50.767	−23:54:56.42	1126+3418	11:26:12.536	+34:18:20.67
0223+0732	02:23:33.975	+07:32:18.99	1129+3622	11:29:51.387	+36:22:15.70
0223+1159	02:23:40.829	+11:59:10.11	1145+3145	11:45:23.236	+31:45:17.24
0224+1357	02:24:41.842	+13:57:33.00	1146+2601	11:46:08.554	+26:01:05.58
0238−3032	02:38:55.197	−30:32:02.67	1150+3020	11:50:43.890	+30:20:17.66
0249+1237	02:49:44.482	+12:37:06.27	1201+2550	12:01:25.648	+25:50:04.55
0251−1742	02:51:06.234	−17:42:39.77	1201+3129	12:01:44.264	+31:29:03.22
0258−3146	02:58:05.951	−31:46:27.90	1220+3111	12:20:04.656	+31:11:45.04
0259+0747	02:59:27.067	+07:47:39.06	1234+2917	12:34:54.323	+29:17:43.93
0259+4708	02:59:04.207	+47:08:40.31	1236+3706	12:36:50.831	+37:06:02.01
0317+0606	03:17:26.849	+06:06:14.53	1242+2721	12:42:19.687	+27:21:57.32
0322−3458	03:22:13.098	−34:58:33.34	1251+3643	12:51:24.132	+36:43:57.27
0326−3243	03:26:15.123	−32:43:24.41	1334+3434	13:34:26.833	+34:34:25.11
0349+0354	03:49:14.315	+03:54:45.34	1343+2903	13:43:24.006	+29:03:57.55
0403+6445	04:03:42.805	+64:45:56.01	1414+4022	14:14:40.585	+40:22:25.75
0421+3511	04:21:19.710	+35:11:15.79	1426+4035	14:26:58.101	+40:35:38.36
0458+4953	04:58:28.750	+49:53:55.67	1434+3805	14:34:46.988	+38:05:14.87
0505+2606	05:05:54.171	+26:06:25.03	1458+3720	14:58:44.704	+37:20:22.15
0518+6439	05:18:43.662	+64:39:57.72	1508+2818	15:08:08.312	+28:18:13.51
0606+4401	06:06:50.206	+44:01:40.73	1547+3954	15:47:40.147	+39:54:38.48
0607+2915	06:07:18.949	+29:15:27.64	1606+2709	16:06:16.249	+27:09:28.69
0620+7334	06:20:52.108	+73:34:41.12	1609+2628	16:09:50.978	+26:28:38.72
0701+2631	07:01:20.742	+26:31:56.95	1618+2931	16:18:27.685	+29:31:17.99
0719+2935	07:19:22.188	+29:35:43.30	1635+3751	16:35:53.071	+37:51:54.59
0733+3331	07:33:13.289	+33:31:51.81	2321−1758	23:21:02.411	−17:58:22.09

Table A-2. Parameters of Observed FIRST/NVSS Sources

Source	FIRST Source?	S_{1400}[a] (mJy)	% poln[b]	Source	FIRST Source?	S_{1400}[a] (mJy)	% poln[b]
0002−1952	N	58	9	0755+3013	Y	51	11
0004−1148	N	450	6	0755+3341	Y	81	7
0011−2254	N	37	9	0757+2721	Y	44	7
0014−2800	N	52	14	0758+3929	N	530	8
0023−2155	N	135	8	0802+3122	N	84	10
0024+0308	N	68	9	0805+2737	N	41	9
0026−1112	N	166	7	0806+3310	N	44	6
0027−3030	N	24	13	0810+3034	Y	152	6
0032−2649	N	131	6	0840+2923	Y	17	13
0037−2323	N	66	5	0843+3738	Y	108	11
0040+1329	N	34	9	0844+3629	Y	49	6
0051+0229	N	15	20	0846+3746	N	21	15
0054−1754	N	29	11	0903+3523	Y	57	6
0057+1341	N	64	8	0911+3349	Y	370	7
0107−1211	N	56	6	0923+3011	Y	34	6
0114−3219	N	122	16	0928+4142	N	96	12
0138−2954	N	45	10	0944+3803	N	42	11
0146+0222	N	136	8	1000+3718	Y	35	9
0147+0715	N	237	6	1003+3244	Y	419	7
0154−2422	N	45	10	1013+3445	Y	350	6
0214+1027	N	27	12	1033+2851	Y	29	9
0217−2354	N	82	11	1126+3418	Y	39	7
0223+0732	N	128	12	1129+3622	Y	119	6
0223+1159	N	34	9	1145+3145	Y	77	10
0224+1357	N	93	9	1146+2601	Y	114	7
0238−3032	N	155	5	1150+3020	Y	31	13
0249+1237	N	255	6	1201+2550	Y	20	24
0251−1742	N	65	12	1201+3129	Y	87	6
0258−3146	N	242	8	1220+3111	Y	28	8
0259+0747	N	807	5	1234+2917	Y	434	9
0259+4708	N	107	9	1236+3706	Y	62	9
0317+0606	N	196	8	1242+2721	Y	69	10
0322−3458	N	49	7	1251+3643	Y	29	8
0326−3243	N	93	5	1334+3434	Y	48	7
0349+0354	N	147	8	1343+2903	Y	22	17
0403+6445	N	72	5	1414+4022	Y	43	6
0421+3511	N	68	9	1426+4035	Y	28	9
0458+4953	N	19	12	1434+3805	Y	149	9
0505+2606	N	23	9	1458+3720	Y	210	6
0518+6439	N	28	12	1508+2818	Y	76	7
0606+4401	N	145	8	1547+3954	Y	128	15
0607+2915	N	25	14	1606+2709	Y	29	7
0620+7334	N	84	9	1609+2628	Y	17	15
0701+2631	N	32	11	1618+2931	Y	29	8
0719+2935	Y	15	14	1635+3751	Y	47	6
0733+3331	N	19	13	2321−1758	N	17	13

[a]NVSS catalog total intensity 1400-MHz peak flux density.

[b]NVSS catalog percent linear polarization from 1400-MHz peak flux densities.

the broadening of the intrinsic pulse according to

$$\tau_{\rm DM} = \left(\frac{202}{\nu}\right)^3 {\rm DM}\,\Delta\nu. \qquad \text{(A.1)}$$

Here $\tau_{\rm DM}$ is in milliseconds, ν is the observing frequency in MHz, DM is the dispersion measure in pc cm^{-3}, and $\Delta\nu$ is the channel bandwidth in MHz. For our observing system, $\tau_{\rm DM}$ is 1.135 μs per pc cm^{-3} of DM. The fast sampling rate ($t_{\rm samp}$ = 50 μs) and small channel bandwidth ($\Delta\nu$ = 31.25 kHz) in our survey made it sensitive to sub-millisecond pulsars for a large range of DMs (DM $\lesssim$ 500 pc cm^{-3}) in the absence of pulse scattering effects. Our estimated sensitivity to pulsations for a range of periods and DMs is shown in Figure A-1. The method used to produce Figure A-1 follows the one described in Chapter 2 for the Parkes Multibeam Pulsar Survey.

A.3 Data Reduction

In each observation, the frequency channels were dedispersed at 91 trial DMs which ranged from 0 to 1400 pc cm^{-3} and were summed. We searched this large DM range in the unlikely event that a source could be a previously missed long-period pulsar with a high DM. For DM $\gtrsim$ 500 pc cm^{-3} the channel dispersion smearing is too great to maintain sensitivity to sub-millisecond pulsations from all our sources. However, the Taylor & Cordes (1993) model of the Galactic free electron distribution indicates that for all of our sources, with the exception of two that are within 5° of the Galactic plane, the DMs are expected to be less than 100 pc cm^{-3} regardless of distance. Each resulting dedispersed time series of 2^{23} samples was then coherently Fourier transformed to produce an amplitude modulation spectrum corresponding to a trial DM.

RFI produced many false peaks in certain narrow regions of the modulation spectra at low DMs. We therefore masked several frequency ranges and their harmonics in which RFI appeared regularly so that any true pulsar signals were not swamped by interference. Typically 1-2% of the modulation spectrum in each observation was lost in this way.

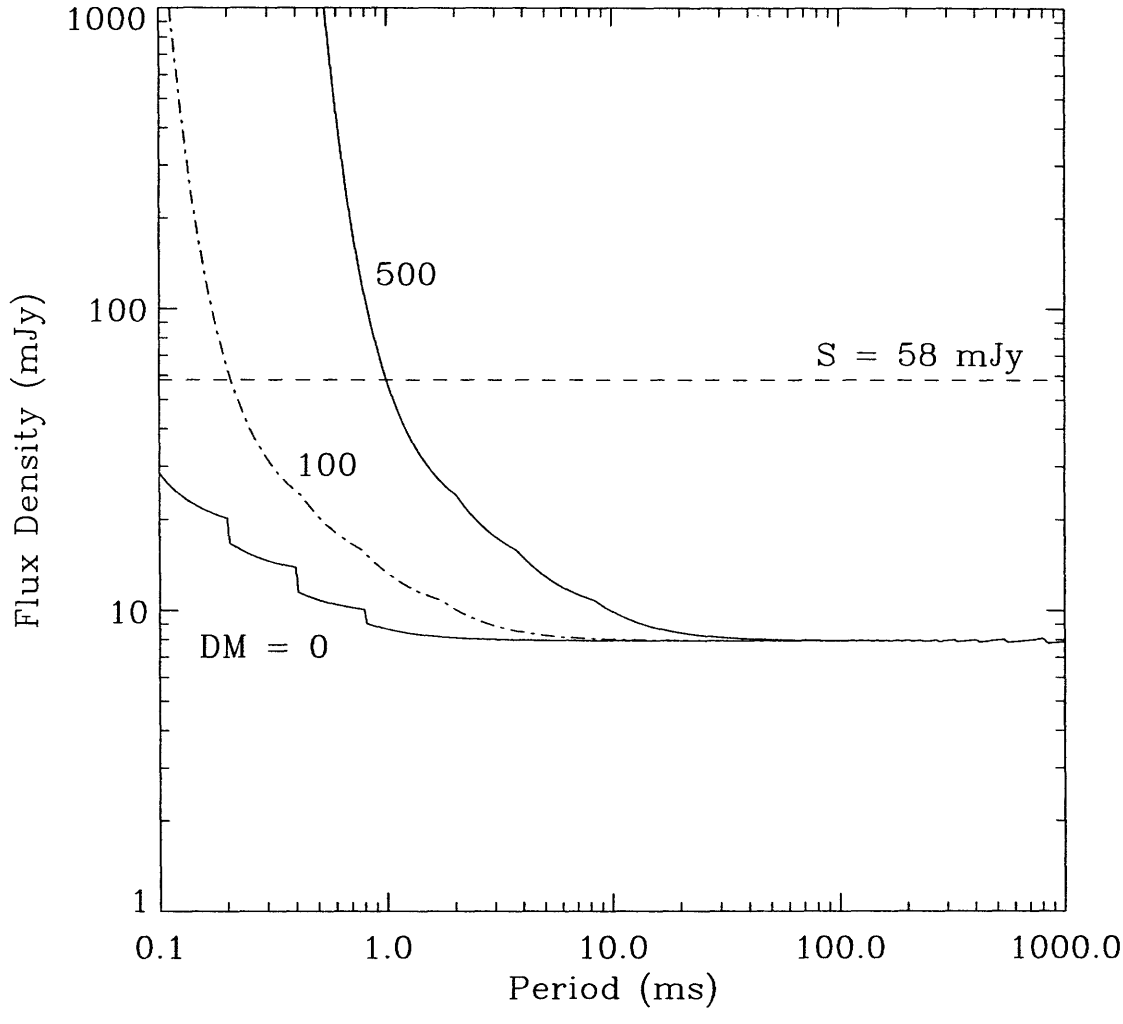

Figure A-1 Pulsar sensitivity curves for DMs of 0, 100, and 500 pc cm^{-3}, assuming a 5% intrinsic pulsed duty cycle. The dashed horizontal line at 58 mJy is the flux density of our weakest source at 600 MHz, assuming a typical pulsar spectral index of $\alpha = -1.6$. All of our sources are expected to have DM < 100 pc cm^{-3} (indicated by the dashed-dotted line).

We then looked for the strongest peaks in the spectra. First, each modulation spectrum was harmonically summed. In this process, integer harmonics in the modulation spectrum are summed, enhancing sensitivity to harmonic signals (e.g., Nice, Fruchter, & Taylor 1995). This is particularly useful for long-period pulsars, which have a large number of unaliased harmonics. After summing up to 16 harmonic signals, the highest candidate peaks in the modulation spectrum were recorded along with the period, DM, and the signal-to-noise ratio (S/N). Redundant harmonic candidates were then eliminated. Unique candidates were recorded if they had S/N > 7 and if the candidate period appeared in at least 10 DM trials. The final candidates for each beam were inspected by dedispersing the original data at DMs near the candidate DM and folding the data at periods near the candidate period in order to look for a broad-band, continuous pulsar-like signal.

This technique was tested by observing several known bright pulsars, PSR J1939+2134, PSR J0332+5434 (B0329+54), and PSR J2145−0750, throughout the survey. The results for these pulsars are listed in Table A-3. All three pulsars were detected with S/N consistent with our survey sensitivity, though scintillation affects the detection strengths.

A.4 Discussion

We did not detect any significant pulsations from the target sources. Here we consider possible effects which could prevent detection if they were pulsars.

A.4.1 Source Brightness

The selected sources were bright, with the weakest source having a 1400-MHz flux density of 15 mJy. Assuming a typical pulsar spectral index of $\alpha = -1.6$ (Lorimer et al. 1995), where α is defined according to $S \sim \nu^{\alpha}$, this source would have flux density 58 mJy at 600 MHz (the horizontal dashed line in Figure A-1). For expected DMs, this is about seven (four) times greater than our sensitivity limit for periods greater than (about equal to) 1 ms, as indicated in Figure A-1. All of our sources, therefore,

were bright enough (in the absence of scintillation) to be easily detectable with our observing system if they were pulsars.

A.4.2 Dispersion Smearing and Scattering

Dispersion smearing is not a factor preventing detection, since all but two of these sources have high Galactic latitudes ($|b| > 5°$) and should have DM < 100 pc cm^{-3} regardless of distance. This is well within our sensitivity limits to sub-millisecond pulsations (see Figure A-1). Interstellar scattering, which can be estimated from the Taylor & Cordes (1993) model of the Galactic electron distribution, is expected to be negligible at 610 MHz. Two of the sources (0458+4953 and 0607+2915) are within 5° of the Galactic plane; for an assumed DM of 100 pc cm^{-3}, their predicted pulse scatter-broadening times are ~ 140 μs at 610 MHz. This is small enough to maintain sensitivity to sub-millisecond pulsations, and is of the same order as the dispersion smearing (113 μs) at this DM.

A.4.3 Wide Beaming

An extremely wide beam would prevent modulation of the pulsed signal and could render a pulsar undetectable. However, this would likely occur only in an aligned rotator geometry in which both the spin and magnetic axes are pointing toward us. This is unlikely for our targets, since, if they were pulsars, the position angle of linear polarization is expected to follow the projected direction of the magnetic axis as the star rotates (Lyne & Manchester 1988). This geometry would significantly reduce the measured degree of linear polarization as the pulsar rotates, inconsistent with our choice of significantly polarized sources.

A.4.4 Scintillation

Scintillation is the modulation of a radio signal passing through a medium of variable index of refraction, such as an inhomogeneous interstellar plasma. In diffraction scintillation, the wave scattering causes interference which can enhance or suppress

the amplitude of the radio signal on the time scale of minutes (e.g., Manchester & Taylor 1977). These intensity fluctuations vary as a function of radio frequency at any given time and have a characteristic bandwidth $\Delta\nu$, where

$$\Delta\nu \simeq 11\,\nu^{22/5}\,d^{-11/5}. \tag{A.2}$$

Here $\Delta\nu$ is in MHz, ν is the observing frequency in GHz, and d is the distance to the source in kpc (Cordes, Weisberg, & Boriakoff 1985). For pulsars with $d < 1$ kpc, this characteristic bandwidth exceeds our 610 MHz observing bandwidth of 1 MHz. Indeed, of 28 nearby pulsars observed at 660 MHz by Johnston, Nicastro, & Koribalski (1998), 13 had scintillation bandwidths greater than our bandwidth of 1 MHz and had a characteristic fluctuation time-scale greater than our integration time of 420 s. More than half of these 13 pulsars had distances less than 1 kpc, and only one had $d > 2$ kpc. If the sources we surveyed were placed at a distance of 2 kpc and a spectral power law index of $\alpha = -1.6$ is assumed, their 400-MHz luminosities would all be at the upper end of the observed pulsar luminosity distribution ($L_{400} > 450$ mJy kpc^2). This suggests that if these sources were pulsars, they are likely to be closer than 2 kpc and therefore in the distance range where the scintillation bandwidth exceeds our observing bandwidth. In this case, scintillation causes the probability distribution of the observed intensity to be an exponential function with a maximum in the distribution at zero intensity (McLaughlin et al. 1999). The number of sources we expect to see in our sample is the sum of the probabilities that we will see each individual source (i.e., that the scintillated flux is above the minimum detectable flux). For the range $P > 1$ ms, we expect to see 88 of the 92 sources (5% missed). For the range $P \sim 1$ ms, we expect to see 85 of the 92 sources (8% missed). Thus, only a few of our sources are likely to have been missed due to scintillation. Therefore scintillation cannot account for the non-detection of the bulk of the sources in the survey.

A.4.5 Binary Orbital Motion

A pulsar in a binary orbit experiences an acceleration which changes the observed modulation frequency during the course of the observation. Sensitivity to pulsations is degraded if the frequency drift exceeds a single Fourier bin $\Delta f = 1/T_{\rm int}$, where $T_{\rm int}$ is the integration time. Assuming that the acceleration of the pulsar is constant during the observation, a critical acceleration can be defined, above which the change in frequency is greater than Δf and the sensitivity is reduced:

$$a_{\rm crit} = \frac{c}{f T_{\rm int}^2}. \tag{A.3}$$

Since the Fourier drift scales linearly with acceleration, the reduction in sensitivity scales linearly with acceleration. For our integration time of 420 s, the critical acceleration is $a_{\rm crit}/P \sim 1.7$ (where $a_{\rm crit}$ is in units of m s^{-2} and P is the pulsar period in ms). Our weakest source is several times brighter than our detection limit (Figure A-1), so a reduction in sensitivity by a factor of several should still maintain detectability to pulsations. Thus, a more appropriate critical acceleration for the weakest source in our list is $a_{\rm crit}/P \sim 12$ (for $P > 1$ ms) and $a_{\rm crit}/P \sim 7$ (for $P \sim 1$ ms).

Orbits containing millisecond or sub-millisecond pulsars that have been spun up from mass transfer from a low-mass donor would be expected to be circular. Of the 40 known pulsars in circular ($e < 0.01$) binary orbits, the largest projected mean acceleration to our line of sight (assuming $i = 60°$) is $a_{\rm mean}/P \sim 3.6$ for PSR J1808−3658, an X-ray millisecond pulsar with a 2.5-ms period in a 2-h binary orbit around a 0.05 $M_\odot$ companion (Chakrabarty & Morgan 1998). This acceleration is well below the critical acceleration $a_{\rm crit}/P$ even for our weakest source.

The mean flux density of the sources on our list, however, is much higher ($S_{610} \sim$ 400 mJy, assuming $\alpha = -1.6$) than our weakest source, which raises the critical acceleration for our typical source. Only very large accelerations ($a_{\rm mean}/P \gtrsim 85$ for $P > 1$ ms and $a_{\rm mean}/P \gtrsim 40$ for $P \lesssim 1$ ms) would prevent detection of pulsations for our typical source. A system such as PSR J1808−3658 with $S_{610} \sim 400$ mJy would still be detectable if it had $P \sim 0.3$ ms or if it had an orbital period $P_b \sim 15$

minutes (but not both). Thus it is unlikely that binary motion in a sub-millisecond or millisecond pulsar system would be a significant source of non-detections for most of our sources.

A.4.6 Likelihood of Serendipitous Detection

We have also estimated the likelihood of serendipitously detecting a pulsar not associated with these sources using the observed surface density of both normal and millisecond pulsars in the Galactic plane (Lyne et al. 1998). With standard assumptions for a spectral power law index and luminosity distribution (Lorimer et al. 1993), we find that it is unlikely ($< 2\%$ probability) that we would detect any pulsars from the chance placement of our 92 beams.

A.5 Conclusions

No pulsations were detected at 610 MHz from the 92 polarized, point-like sources that we searched from the FIRST and NVSS radio surveys. Sensitivity to sub-millisecond pulsations was maintained for DMs less than about 500 pc cm^{-3} (in the absence of scattering effects), which encompasses the expected DM range for all of these sources. We find that several effects which could prevent detection (brightness, dispersion smearing, scattering, and beaming) are not significant factors here. Scintillation is expected to account for only a few of our non-detections and therefore cannot be the cause of the majority of our non-detections. For a source with a typical flux density in our list, Doppler motion in a tight binary system would only prevent detection if the mean projected line-of-sight acceleration of the pulsar were at least an order of magnitude higher than those observed in the known population of circular binary pulsar systems. We conclude that as a population, these sources are unlikely to be pulsars. Given that $\sim 10\%$ of extragalactic sources in the NVSS survey were identified by Han & Tian (1999) as being at least 5% linearly polarized, it is possible that most of our target sources are unidentified extragalactic objects. However, the nature of these sources is still not certain.

Table A-3. Observed Test Pulsars

PSR	P (ms)	DM (pc cm^{-3})	S_{1400}[a] (mJy)	S_{600}[b] (mJy)	S/N
J0332+5434	714.52	26.8	203	785	725
J1939+2134	1.56	71.0	16	100	46
J2145−0750	16.05	9.0	10	30	36

[a]Catalog 1400-MHz flux density (Taylor, Manchester, & Lyne 1993).

[b]Catalog 600-MHz flux density (Taylor, Manchester, & Lyne 1993).

Appendix B

Polarization Properties of Nine Southern Radio Pulsars

This chapter is a modified self-contained paper titled, "Polarization Properties of Nine Southern Radio Pulsars," submitted for publication in the *Astronomical Journal* (Crawford, Kaspi, & Manchester 2000).

We report on radio polarimetry observations of nine southern pulsars. Six of the nine in the sample are young, with characteristic ages under 100 kyr and high spin-down luminosities. All six show a significant degree of linear polarization and exhibit characteristics of partial cone emission, supporting the hypothesis that radio emission from young pulsars is highly linearly polarized and emanates from conal beams. We also confirm a previously noticed trend in which the degree of linear polarization increases with spin-down luminosity. In several cases we have used the rotating-vector model of the pulsar emission geometry to fit the observed position angle data. Our fit for PSR J1513−5908 (B1509−58) in particular is useful for directly testing the magnetospheric model of Melatos (1997) in combination with further timing observations. For this pulsar we find that a magnetic inclination angle greater than or equal to 60° is excluded at the 3σ level, and that the geometry suggested by the morphology of an apparent bipolar X-ray outflow is marginally inconsistent with the Melatos model. We also report on polarimetry of three older pulsars: PSR J0045−7319, PSR J1627−4850, and PSR J1316−6232 (whose discovery we also report). Of these, only

PSR J0045−7319 shows significant polarization.

B.1 Introduction

Polarization observations of radio pulsars are a useful way to probe pulsar beam shapes, the radio emission process, and the properties of the interstellar medium (ISM). The emission geometry of a pulsar can be characterized by two angles: the angle between the spin and magnetic field axes (the magnetic inclination angle, α), and the angle between the spin axis and the observer's line of sight, ζ. The difference between these two angles is the impact parameter of the magnetic axis to the line of sight, β, defined according to $\beta = \zeta - \alpha$. In the rotating-vector model, the position angle (PA) of linearly polarized radiation follows the projected direction of the magnetic field axis as the pulsar rotates (Radhakrishnan & Cooke 1969). The PA, ψ, is expected to make a characteristic S-shape as the pulse swings across the profile, and changes as a function of the pulse phase ϕ according to

$$\tan(\psi - \psi_0) = \frac{\sin\alpha \sin(\phi - \phi_0)}{\sin\zeta\cos\alpha - \cos\zeta\sin\alpha\cos(\phi - \phi_0)}, \tag{B.1}$$

where ψ_0 is the projected direction of the rotation axis of the pulsar and ϕ_0 is the phase of maximum PA swing. By rewriting the equation in terms of the directly measured β rather than ζ and fitting the observed PA values to this model, one can attempt to constrain these angles and understand the orientation of the pulsar axes (Lyne & Manchester 1988).

In addition to elucidating pulsar magnetic and spin geometries, polarization observations are useful for a variety of other reasons. For example, Melatos (1997) has proposed a model of the pulsar magnetosphere in which the pulsar and inner magnetosphere are treated as a single perfectly conducting sphere rotating in a vacuum. With three observable parameters (P, $\dot{P}$, and α), the model predicts values for the first and second braking indices, n and m, which are defined as a function of the pulsar's rotation frequency $f \equiv 1/P$ and its time derivatives:

$$n = \frac{f\ddot{f}}{\dot{f}^2}, \tag{B.2}$$

$$m = \frac{f^2\dddot{f}}{\dot{f}^3}. \tag{B.3}$$

The model predicts values of n for the Crab, PSR J0540−6919 (B0540−69), and PSR J1513−5908 (B1509−58) which agree to 4% with observed values from timing data. To date, only the Crab pulsar (Lyne, Pritchard, & Smith 1993) and PSR J1513−5908 (Kaspi et al. 1994b) have had simultaneous measurements of n and m from a measured third period derivative, and PSR J1513−5908 is the only pulsar for which this has been done from absolute pulse numbering. Glitches and timing noise in the Crab pulsar may never allow a direct estimate of m for the Crab, though the Melatos (1997) prediction is consistent with current estimates obtained indirectly by Lyne, Pritchard, & Smith (1993). On the other hand, the accuracy of the spin parameters for PSR J1513−5908 should increase over time. Therefore PSR J1513−5908 is the best pulsar with which to test the Melatos model. An estimate of $\alpha \sim 60°$ was obtained by fitting the pulse profiles and the relative phase offsets of the peaks from radio, X-ray, and soft gamma-ray observations to an outer-gap emission model (Romani & Yadigaroglu 1995). Radio polarimetry can provide a more reliable and accurate way of measuring α.

Polarimetric observations of young radio pulsars in general indicate that they are typically more highly polarized than their older counterparts (Qiao et al. 1995). In addition, young pulsars seem to show characteristics consistent with their emission coming from partial conal beams, in contrast to emission from core beams that is often seen in older pulsars (Manchester 1996). In the conal emission scenario, the radiation is thought to come from one side of a hollow cone in the outer part of the radio beam, rather than emanating from a core beam centered on the magnetic axis. The hollow cone could arise because radiation is produced in only a restricted range of field line curvature. One consequence of this is that for a wide cone, a significant phase offset can be observed between the profile peak, which occurs at the edge of

the cone, and the point of maximum PA swing, which traces the magnetic axis. If no significant phase offset is seen, then a shallow PA swing would be present, implying a large impact parameter. Conal beams are typically more highly linearly polarized and have weak circular polarization, while core beams have weak linear polarization and a sign reversal in the circular polarization (Lyne & Manchester 1988). It is not known why young pulsars should exhibit strongly linearly polarized emission from conal beams and why the degree of linear polarization should increase with spin-down luminosity.

Polarization observations of pulsars also allow the determination of rotation measures (RMs) which probe the Galactic magnetic field at a variety of distances. The mean line-of-sight ISM magnetic field strength can be estimated from measurements of the RM and dispersion measure (DM) using

$$\langle B_{||} \rangle = 1.232 \frac{\mathrm{RM}}{\mathrm{DM}} \mu\mathrm{G}, \tag{B.4}$$

where RM is measured in units of rad m^{-2} and DM in units of pc cm^{-3} (Manchester & Taylor 1977). RM measurements can also help support associations between young pulsars and supernova remnants (SNRs). Traditionally this is done by measuring a consistent age and distance for the pulsar and remnant. In most cases, however, there are either significant discrepancies or large uncertainties in these estimates. If the RM of the pulsar and the RM of the SNR at the location of the pulsar are consistent with each other, then an association would be supported.

We report on radio polarization observations of six young southern radio pulsars. These pulsars all have characteristic ages $\tau_c < 100$ kyr and have spin-down luminosities $\dot{E} > 10^{34}$ erg s^{-1}. Polarization results for much of the rest of the young pulsar population can be found elsewhere (e.g., Qiao et al. 1995; Gould & Lyne 1998). We also report on polarimetry of three pulsars which are not particularly young, but are interesting for other reasons: PSR J0045−7319 is in a binary orbit with a non-degenerate companion, PSR J1316−6232, whose discovery we also report, is spatially coincident with a region of extended radio emission, and PSR J1627−4845 is spatially

coincident with SNR G335.2+0.1. The physical characteristics of the pulsars in our sample are listed in Table B-1.

B.2 Observations and Data Reduction

All pulsars in our sample were observed with the 64-m radio telescope[1] in Parkes, NSW, Australia from 17-24 February 1997 at 1350 MHz, except PSR J0045−7319 which was observed at 660 MHz. Follow-up observations were conducted on several pulsars on 15-16 January 1998 at 660 MHz and 2260 MHz. Table B-2 lists the parameters for the observations. The details of the hardware setup and observing technique are the same as those reported elsewhere (Navarro 1994; Navarro et al. 1997; Manchester, Han, & Qiao 1998).

In cases where we did not have an initial RM estimate, an improper RM correction to the data could cause the PAs from different frequency channels to wind by more than one rotation and add destructively. Therefore, we tried a large range of RMs, typically ± 100 DM rad m^{-2}, where DM is in units of pc cm^{-3}. In most cases one of the trial RMs yielded a significantly larger linear polarization magnitude than the others. We used this RM as the starting point for our RM convergence.

B.3 Results and Discussion

Seven of the nine pulsars (including all six of the young pulsars) show linear polarization significant enough to permit an RM estimate. The measured polarization parameters for the pulsars are listed in Table B-3, with L and V representing linearly and circularly polarized intensity respectively. The polarization profiles for the seven pulsars for which there was significant polarization appear in Figures B-1 through B-4. Position angles with more than 20° uncertainty were not plotted except in the case of PSR J0045−7319 which was weak and therefore had an imposed cutoff of

[1]http://www.parkes.atnf.csiro.au. The Parkes Observatory is part of the Australia Telescope, which is funded by the Commonwealth of Australia for operation as a National Facility managed by CSIRO.

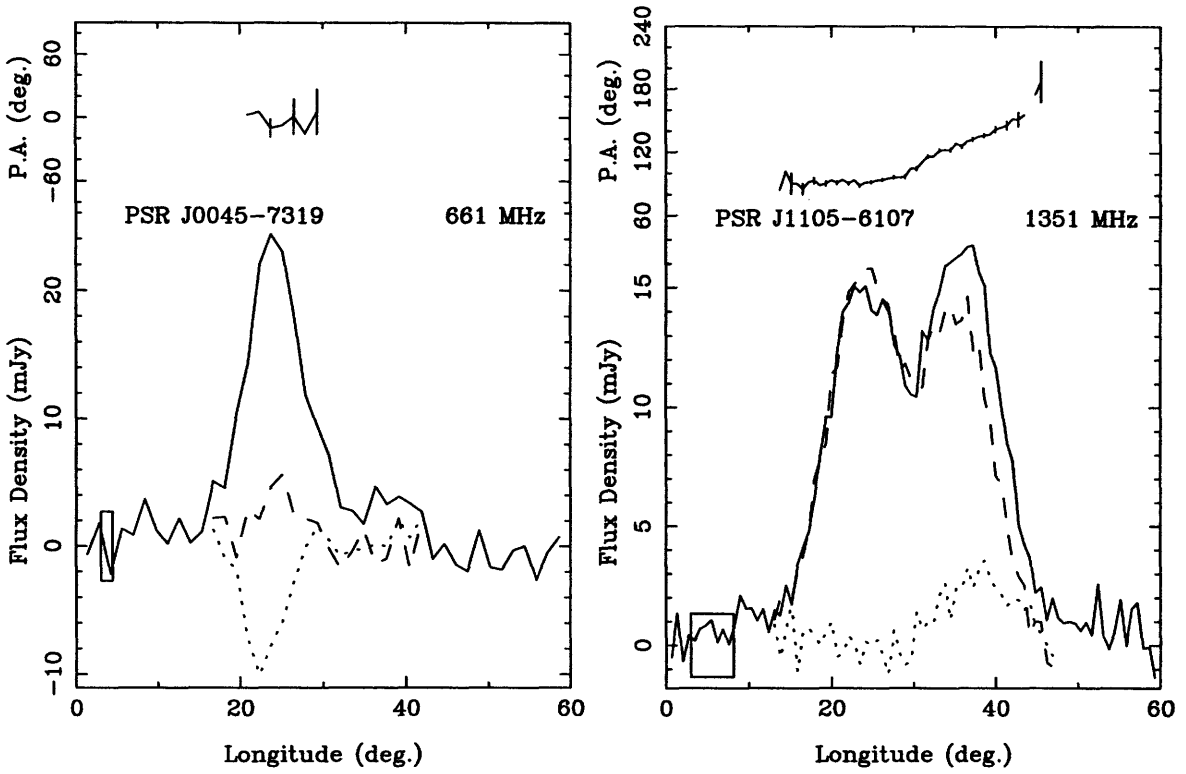

Figure B-1 Polarization profiles for PSRs J0045−7319 and J1105−6107. In the lower half of each plot, the solid line indicates total intensity as a function of pulse phase in degrees. The total intensity has been normalized to the mean flux density using observations of Hydra A. The dashed and dotted lines indicate linearly and circularly polarized intensity respectively. Positive values of circular polarization are left-circularly polarized. The height of the box in the lower left-hand corner is twice the root-mean-square (rms) scatter in the profile baseline. The upper half of each plot shows the position angle as a function of pulse phase. The pulsar name and center frequency of the observation are also indicated in each plot.

40° uncertainty. Table B-4 lists measured RMs and mean line-of-sight magnetic field strengths with 1σ uncertainties for each. Total intensity pulse widths are also included in Table B-4. In several cases the PA could be measured over a significant fraction of the 1350-MHz profile with good signal-to-noise. For these pulsars we attempted to fit the observed PA swing over the profile to the rotating-vector model. Below we outline the polarization results for each pulsar separately.

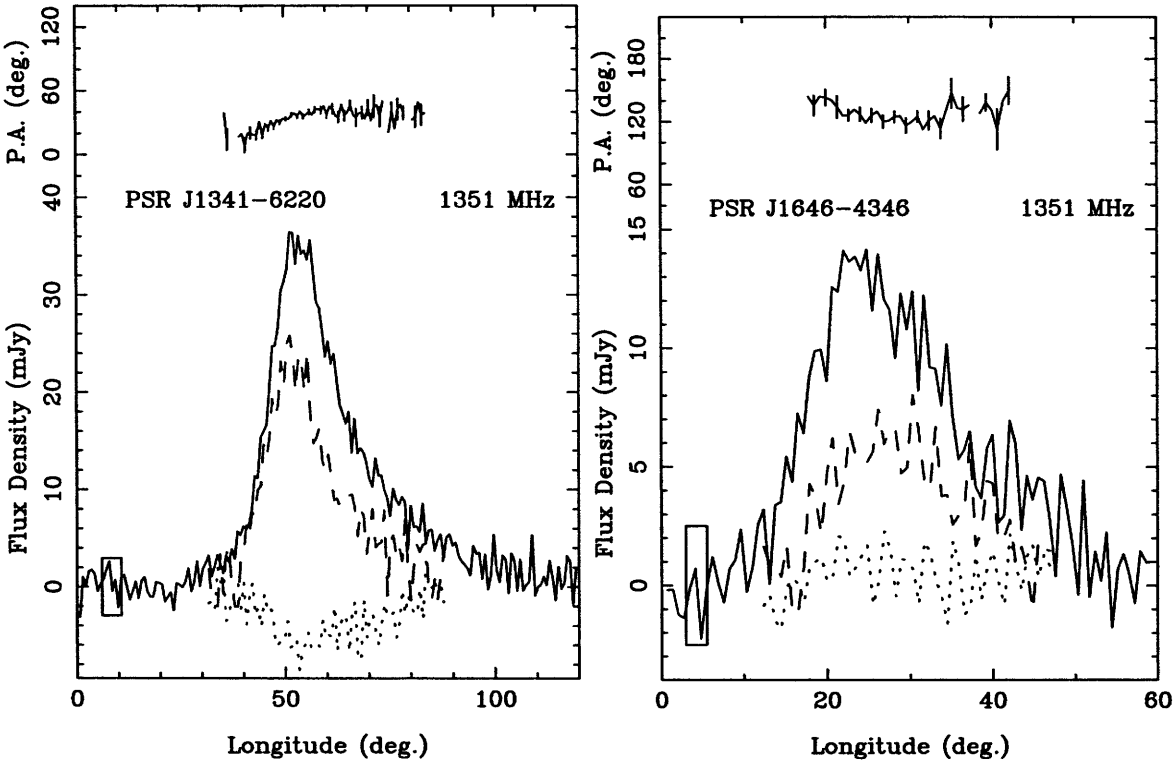

Figure B-2 Polarization profiles for PSRs J1341−6220 and J1646−4346. See caption of Figure B-1 for figure legend.

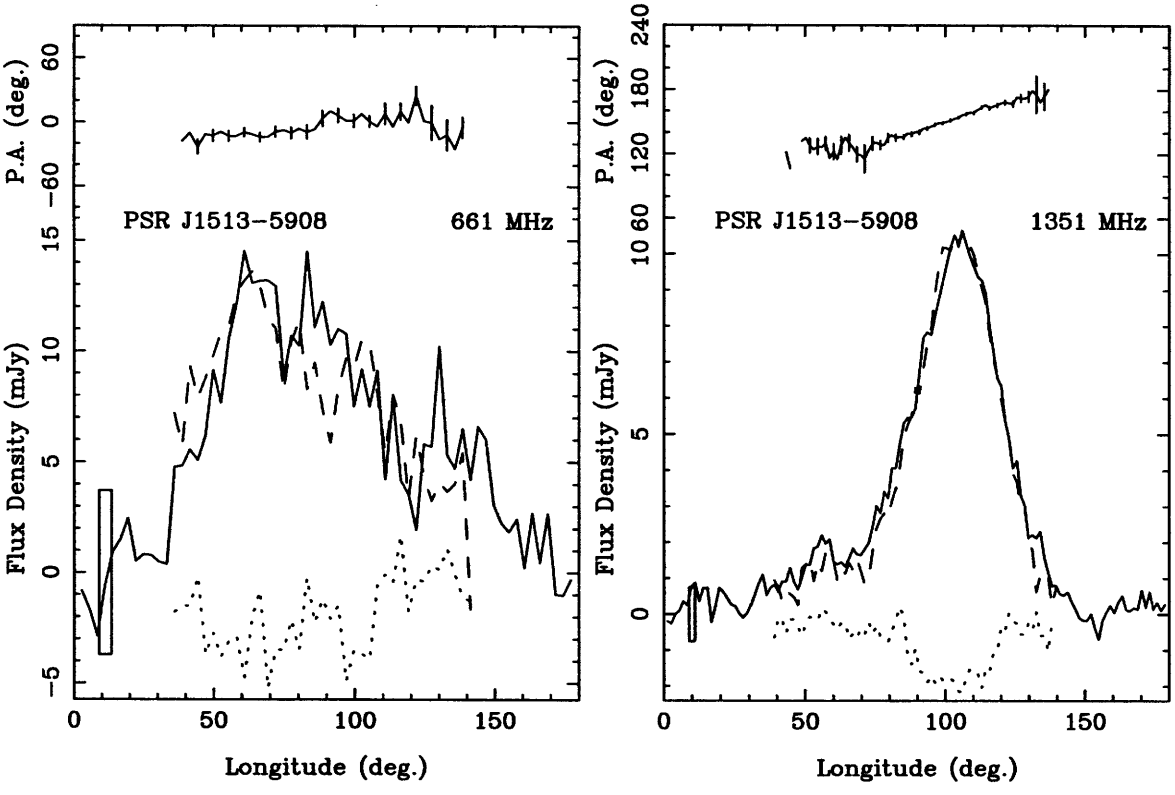

Figure B-3 Polarization profiles for PSR J1513−5908. See caption of Figure B-1 for figure legend.

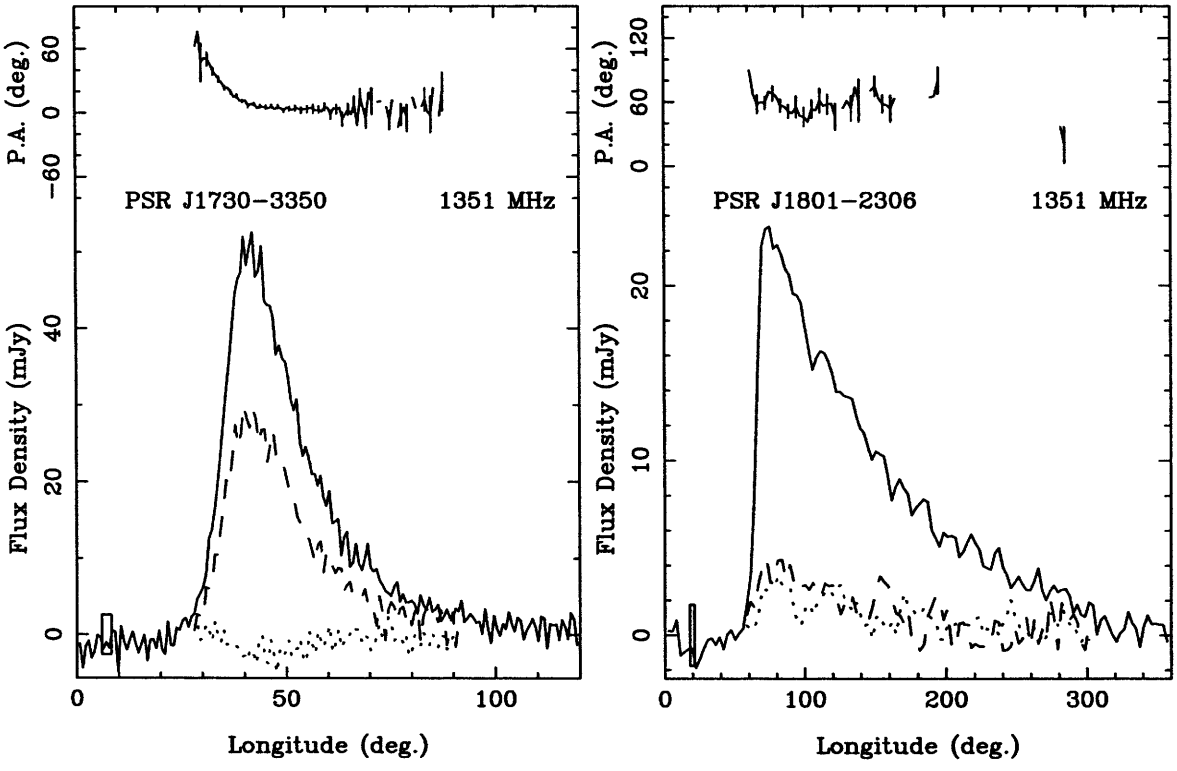

Figure B-4 Polarization profiles for PSRs J1730−3350 and J1801−2306. See caption of Figure B-1 for figure legend.

B.3.1 PSR J0045−7319

PSR J0045−7319 was the first pulsar discovered in the Small Magellanic Cloud (SMC) (McConnell et al. 1991) and is in a 51-day binary orbit around a B1 class V star (Kaspi et al. 1994a). The wind from the B star, however, is very tenuous and has been shown to contribute little to the DM (Kaspi, Tauris, & Manchester 1996). This is consistent with our results which indicate that during periastron passage (from 18 February 1997 to 23 February 1997) the RM remains small.

The 660-MHz polarization profile, compiled from a total of about 8 h of observations made over 6 days, shows slight linear and circular polarization with large uncertainties in each (Figure B-1). The pulsar flux density and polarization, however, are too weak to allow us to say anything meaningful about the PA swing and emission geometry. However, a secondary component to the right of the main peak is likely one of the outlying profile components which is clearly visible in higher frequency profiles. Since the majority of the contribution to the DM ($\sim 75\%$) is likely to be from the SMC itself, the measured RM (and mean line-of-sight magnetic field strength) is strongly weighted toward the ISM of the SMC. The very low value of -0.2 ± 0.3 μG for $\langle B_{||} \rangle$ indicates that this part of the SMC has magnetic fields which are either tangled or largely perpendicular to the line of sight.

B.3.2 PSR J1105−6107

PSR J1105−6107 is a young and energetic pulsar: its $\dot{E} = 2.5 \times 10^{36}$ erg s^{-1} is in the top 1% of those of all known pulsars and its characteristic age is 63 kyr (Kaspi et al. 1997). The 1350-MHz polarization profile shows two peaks separated by $\sim 40°$ (Figure B-1). The profile is $\sim 100\%$ and $\sim 80\%$ linearly polarized over the first and second peaks respectively. The second peak shows a slight increase in left-handed circular polarization, though it remains weak. The high degree of linear polarization, offset of the PA swing from the pulse peak, and the asymmetric sign change in the circular polarization all indicate that the emission is from the leading edge of a cone. The occurrence of the maximum PA swing after the double peak indicates that both

components are likely part of the leading edge of the conal beam (Manchester 1996). Our attempt to fit the PA data from PSR J1105−6107 to the rotating-vector model did not yield a reliable result and no formal constraints on the geometry of the pulsar could be made.

B.3.3 PSR J1316−6232

PSR J1316−6232 is a 343-ms pulsar with a large DM (983 pc cm^{-3}) that was serendipitously discovered in the same survey targeting O and B stars in which PSR J1105−6107 was discovered (Kaspi et al. 1997). However, neither pulsar is associated with a target star; we report the discovery of PSR J1316−6232 here. After its discovery, timing observations were carried out at Parkes using a hardware setup and analysis procedure which is described elsewhere (D'Amico et al. 1998). A total of 90 observations spanning 733 days were used at frequencies ranging from 1390 MHz to 2000 MHz. Arrival times for the observations were fitted using the TEMPO software package,[2] with an rms timing residual of $\sim$ 5 ms. The best-fit timing parameters for the pulsar can be found in Table B-5.

The profile at 1350 MHz has a large asymmetric tail due to multipath scattering with a time constant $\tau_s \sim 150$ ms. Scattering may be smearing any linearly polarized emission, but at 2260 MHz, the scattering is significantly reduced ($\tau_s \sim 55$ ms), and still no significant linearly polarized emission is seen. A 4.85-GHz map of the region from the Parkes-MIT-NRAO Southern Survey (Condon, Griffith, & Wright 1993) shows a region of extended radio emission coincident with the position of the pulsar. This may account for the large DM and scattering if this region is in front of the pulsar. However, this is unlikely that it would cause significant Faraday smearing since the RMs that would be necessary (RM $> 10^4$ rad m^{-2}) far exceed observed RM values in the ISM (Gray et al. 1999). It is more likely that PSR J1316−6232 is simply intrinsically unpolarized.

[2]http://pulsar.princeton.edu/tempo.

B.3.4 PSR J1341−6220

PSR J1341−6220 (B1338−62) is a young pulsar with $P = 193$ ms and an age of 12 kyr (Kaspi et al. 1992). At 1350 MHz, the pulsar shows significant linear polarization (56%) and right-handed circular polarization (21%) (Figure B-2). A previous estimate of the linear polarization at 1400 MHz (Qiao et al. 1995) was somewhat higher (80%) but had a significantly larger uncertainty ($\sim$ 10%) than the results quoted here. The high degree of linear polarization is consistent with conal emission characteristics. A scattering tail of length $\sim$ 8 ms is evident, not surprising considering the high DM (730 pc cm^{-3}). We had limited success in fitting the rotating-vector model to the PA data for PSR J1341−6220; the uncertainties in the best-fit parameters were large and no constraints could be made.

B.3.5 PSR J1513−5908

PSR J1513−5908 was first discovered as an X-ray source (Seward & Harnden 1982) and was subsequently found to be a radio pulsar (Manchester, Tuohy, & D'Amico 1982). Timing observations showed that it has a large $\dot{E} = 2 \times 10^{37}$ erg s^{-1} and a small characteristic age ($\tau_c \sim 1.5$ kyr). The pulsar is located near SNR G320.4−1.2; the two are almost certainly associated (Gaensler et al. 1999).

The polarization profiles for PSR J1513−5908 at both 660 MHz and 1350 MHz show that the emission is almost completely linearly polarized, with significant right-handed circular polarization as well (Figure B-3). The high degree of linear polarization, shallow PA swing, and absence of a sign change in the circular polarization over the profile all support the notion that the emission is from the grazing edge of a conal beam. In the 1350-MHz profile, there appears to be a possible secondary peak about 40° prior to the main peak which may be polarized.

There is no significant falloff in the degree of linear polarization between 660 MHz and 1350 MHz; if a falloff occurs, it is at higher frequencies (Manchester et al. 1973; Manchester & Taylor 1977). The unchanging linear polarization supports the observation that high-$\dot{E}$ pulsars do not suffer as significantly from depolarization

effects at high frequencies as do low-$\dot{E}$ pulsars (von Hoensbroech, Kijak, & Krawczyk 1998).

The RM estimates at the two frequencies ($+211 \pm 5$ rad m^{-2} at 660 MHz and $+215 \pm 2$ rad m^{-2} at 1350 MHz) are consistent with each other and are consistent with the measured RM of SNR G320.4−1.2 of $+210 \pm 30$ rad m^{-2} at the location of the pulsar (Gaensler et al. 1999). This supports the association between the pulsar and the remnant, considering that the RM in different parts of the SNR varies by hundreds of rad m^{-2}.

As mentioned in Section B.1, the magnetospheric model of Melatos (1997) can be tested with an accurate determination of the emission geometry of PSR J1513−5908. In particular, an estimate of α can be used along with P and $\dot{P}$ to make predictions for the braking indices n and m. These predictions can be compared to the measured values of n and m from pulsar timing (Kaspi et al. 1994b). From our fit of the 1350-MHz data to the rotating-vector model, values of $\alpha \geq 60°$ are excluded at the 3σ level. A previous estimate of $\alpha \sim 60°$ was suggested from a fit of the high-energy pulse profile to an outer-gap model (Romani & Yadigaroglu 1995). Our result suggests that this value is unlikely.

For an inclination angle range of $\alpha < 60°$, the Melatos (1997) model predicts that the first braking index should be $n < 2.92$ for PSR J1513−5908. The observed value of 2.837 ± 0.001 (Kaspi et al. 1994b) falls easily in this range. For $\alpha < 60°$, the second braking index is predicted by the model to be $m < 14.0$. Currently the best measured value for this parameter is $m = 14.5 \pm 3.6$ (Kaspi et al. 1994b), which partially overlaps the predicted range. Therefore the Melatos model cannot be directly checked given the estimates from current data, but it should be possible in the future.

The swing of the observed PA data is shallow, implying a large impact parameter. However, the angles β and ζ could not be significantly constrained in the fit given the large uncertainties. Therefore no direct check could be made in the fit with the estimate of $\zeta \gtrsim 70°$ from Brazier & Becker (1997), obtained by interpreting the X-ray morphology of the surrounding region as being the result of a bipolar outflow from the

pulsar with an equatorial torus. However, by imposing the restriction that $\zeta > 70°$ in our fit, we find that $\alpha > 30°$ at the 3σ level. Imposing $\alpha > 30°$ yields a prediction of $n > 2.86$ in the Melatos model. This is marginally inconsistent with the observed value of $n = 2.837 \pm 0.001$ (Kaspi et al. 1994b), and hence is similarly marginally inconsistent with the limit on ζ given by Brazier & Becker (1997).

B.3.6 PSR J1627−4845

PSR J1627−4845 was one of two new pulsars discovered in a targeted search of southern SNRs (Kaspi et al. 1996) and is spatially coincident with SNR G335.2+0.1. However, the discrepancy in the ages of the objects indicates that the association is only a chance superposition. We were unable to detect significant linear polarization or determine a rotation measure for this pulsar at 1350 MHz. It is likely that the intrinsic polarization is low as might be expected for an old pulsar.

B.3.7 PSR J1646−4346

PSR J1646−4346 (B1643−43) is a 232-ms pulsar with an age of 32 kyr (Johnston et al. 1995). The 1350-MHz polarization profile is noisy but shows significant linear polarization (45%) and negligible circular polarization (Figure B-2). There is also a slight profile asymmetry ($\tau_s \sim 11$ ms) probably from multipath scattering. This could mean that the intrinsic degree of linear polarization is higher than the measured value of 45%, and that it is being reduced by the scattering. The high degree of linear polarization is consistent with conal emission, and the estimated RM of -65 ± 17 rad m^{-2} implies $\langle B_{||} \rangle = -0.16 \pm 0.04$ μG, which is consistent with Galactic magnetic field strengths.

B.3.8 PSR J1730−3350

PSR J1730−3350 (B1727−33) has a period of 139 ms and is young, with a characteristic age of 26 kyr (Johnston et al. 1995). The polarization profile at 1350 MHz shows significant linear polarization (56%) with weak circular polarization (Figure

B-4). This is consistent with the results of Gould & Lyne (1998) who find the degree of linear polarization to be 48% at 1400 MHz. There is also a significant scattering tail ($\tau_s \sim 7$ ms) from multipath scattering, which could reduce the measured linear polarization in this part of the profile. The PA swing shows one side of a steep characteristic S-shape and indicates a small impact parameter. Our fit to the PA data preceding the profile peak (where scattering has little effect) is consistent with this and indicates that $|\beta| < 5°$ at the 3σ confidence level. The phase offset of the point of maximum swing, plus the strong linear polarization and weak circular polarization, argues that the radio emission is coming from the trailing edge of a cone (Manchester 1996). The RM of -142 ± 5 rad m^{-2} measured implies $\langle B_{||} \rangle = -0.68 \pm 0.02$ μG. The RM is consistent with RM measurements of other pulsars in the region with comparable DMs.

B.3.9 PSR J1801−2306

PSR J1801−2306 (B1758−23) was discovered in a search for pulsars directed at Galactic objects (Manchester, D'Amico, & Tuohy 1985). This pulsar was found to be near SNR W28, which led to speculation that the pulsar and remnant were associated (Manchester et al. 1991). The pulsar's characteristic age of 58 kyr is consistent with the estimated age of SNR W28 of between 35 and 150 kyr (Kaspi et al. 1993), but there is a discrepancy between the remnant distance of ~ 3 kpc (Frail, Kulkarni, & Vasisht 1993) and the pulsar distance, which is estimated from its DM to be ~ 13 kpc (Taylor & Cordes 1993). Attempts have been made to resolve this discrepancy by introducing an HII region in the line of sight which could contribute to the bulk of the dispersion (Frail, Kulkarni, & Vasisht 1993). However, there is no clear evidence for such an HII region (Kaspi et al. 1993).

The pulse profile at 1350 MHz (Figure B-4) shows a smaller degree of linear polarization (14%) than the other young pulsars we have observed, and is consistent with the estimate of Gould & Lyne (1998), who find that the linear polarization is 15% at both 1400 MHz and 1600 MHz. The relatively small degree of polarization could be due to depolarization from multipath scattering ($\tau_s \sim 100$ ms) in a region

of high magnetic field and electron density (such as an HII region or SNR). However, at 2260 MHz we find a decrease in linear polarization despite the significant decrease in the scattering ($\tau_s \sim 25$ ms). Using the RM estimate from the 1350-MHz data, we find that the measured linear polarization at 2260 MHz is no more than a few percent. We conclude that PSR J1801−2306 is intrinsically less polarized than the other young pulsars in our sample. This is consistent with the trend noted in Figure B-5 since PSR J1801−2306 has a lower $\dot{E}$ than the other young pulsars in our sample (see below).

B.3.10 Linear Polarization vs. Spin-down Luminosity

By comparing the measured degree of linear polarization of our young pulsars with their spin-down luminosities, $\dot{E}$, we confirm a trend previously noticed by several authors (Wu et al. 1993; Qiao et al. 1995; von Hoensbroech, Kijak, & Krawczyk 1998) in which linear polarization increases with spin-down luminosity. Figure B-5 shows measured linear polarization as a function of spin-down luminosity for our six young pulsars at 1350 MHz (open circles) and for 278 pulsars from Gould and Lyne (1998) at 1400 MHz (dots). The young pulsars in our sample are concentrated at the high-$\dot{E}$ end of the plot while the Gould and Lyne pulsars span an $\dot{E}$ range from 10^{30} to 10^{37} erg s^{-1}. The figure shows a trend in which pulsars with $\dot{E} > 10^{34}$ erg s^{-1} tend to have stronger linear polarization as $\dot{E}$ increases. The six young pulsars in our sample show this trend clearly.

von Hoensbroech, Kijak, & Krawczyk (1998) notice a stronger correlation in a sample of 32 pulsars at a much higher frequency (4.9 GHz). Their trend extends down to about 10^{32} erg s^{-1}. Gould & Lyne (1998) find no such correlation at 400 MHz for any $\dot{E}$ range, and von Hoensbroech, Kijak, & Krawczyk conclude that depolarization effects at high frequencies affect low-$\dot{E}$ pulsars much more strongly than they do high-$\dot{E}$ ones. Our 1350-MHz results confirm these trends.

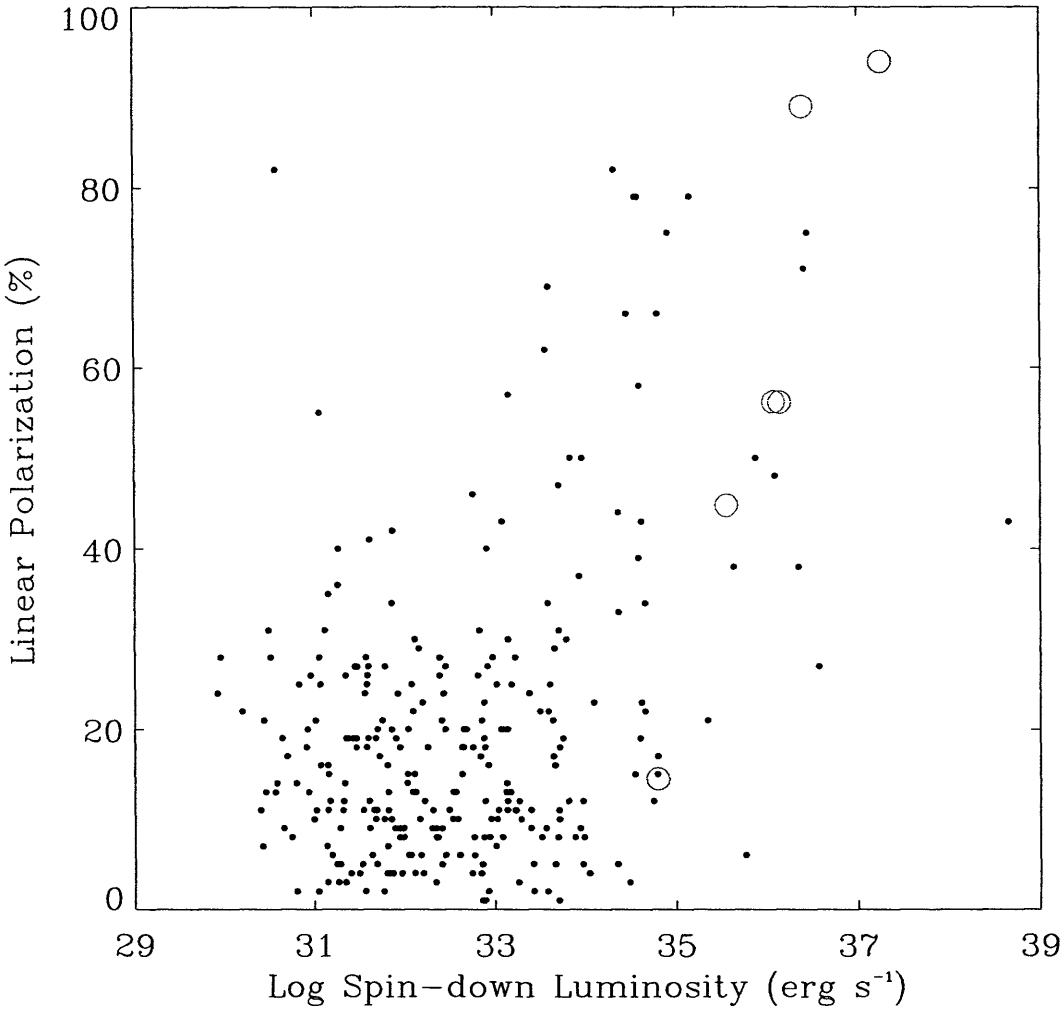

Figure B-5 Linear polarization as a function of log $\dot{E}$ for the six young pulsars in our sample at 1350 MHz (open circles) and 278 pulsars from the 1400-MHz data of Gould & Lyne (1998) (dots). There is a clear trend toward stronger linear polarization at high $\dot{E}$ in both samples.

B.4 Conclusions

We have reported on radio polarimetry observations of nine southern radio pulsars. Significant polarization was detected in seven of the nine, including all six of the young pulsars in the sample. The two pulsars with no detectable polarization (PSRs J1316−6232 and J1627−4845) are older, with $\tau_c > 1$ Myr. With the exception of PSR J1801−2306, all of our young pulsars exhibit a high degree of linear polarization and a degree of circular polarization which is less significant. This suggests that these pulsars are exhibiting partial conal emission (Manchester 1996). The rotating-vector model fit of the PSR J1513−5908 data indicates that a magnetic inclination angle of $\alpha \geq 60°$ is excluded at the 3σ confidence level. This suggests that the value of $\alpha \sim 60°$ estimated for this pulsar by Romani & Yadigaroglu (1995) is unlikely. Imposing the restriction that $\zeta > 70°$ from Brazier & Becker (1997) implies that $\alpha > 30°$ at the 3σ level in our fit. For $\alpha > 30°$, the predicted braking index $n > 2.86$ from the Melatos (1997) model is marginally inconsistent with the observed value of $n = 2.837 \pm 0.001$ (Kaspi et al. 1994b). Thus the predictions of the Melatos model and the geometry of $\zeta \gtrsim 70°$ implied by Brazier & Becker (1997) are inconsistent with each other. We confirm at 1350 MHz a positive correlation between degree of linear polarization and spin-down luminosity.

Table B-1. Physical Characteristics of the Pulsar Sample

PSR	P (s)	DM (pc cm^{-3})	$\log \tau_c$[a] (yr)	$\log B$[b] (G)	$\log \dot{E}$[c] (erg s^{-1})
J0045−7319	0.926	105	6.5	12.3	32.3
J1105−6107	0.063	271	4.8	12.0	36.4
J1316−6232	0.343	983	6.0	12.2	33.7
J1341−6220	0.193	730	4.1	12.9	36.2
J1513−5908	0.151	255	3.2	13.2	37.3
J1627−4845	0.612	557	6.4	12.2	32.8
J1646−4346	0.232	490	4.5	12.7	35.6
J1730−3350	0.139	257	4.4	12.5	36.1
J1801−2306	0.415	1074	4.8	12.8	34.8

[a]Characteristic age.

[b]Surface magnetic field.

[c]Spin-down luminosity.

Table B-2. Observing Parameters

PSR	Date	Freq (MHz)	$T_{\rm int}$[a] (min)	$N_{\rm bins}$[b]	BW[c] (MHz)	$N_{\rm chan}$[d]
J0045−7319	Feb 1997	660	464	256	32	8
J1105−6107	Feb 1997	1350	66	512	128	16
J1316−6232	Feb 1997	1350	72	128	128	64
	Jan 1998	2264	177	256	128	8
J1341−6220	Feb 1997	1350	24	512	128	32
J1513−5908	Jan 1998	660	372	128	32	8
	Feb 1997	1350	192	256	128	32
J1627−4845	Feb 1997	1350	24	512	128	32
J1646−4346	Feb 1997	1350	27	512	128	32
J1730−3350	Feb 1997	1350	30	512	128	16
J1801−2306	Feb 1997	1350	129	128	128	64
	Jan 1998	2264	372	256	128	8

[a]Total integration time.

[b]Number of bins in profile.

[c]Observing bandwidth.

[d]Number of frequency channels.

Table B-3. Measured Polarization Parameters

PSR	Freq (MHz)	S (mJy)	$\langle L\rangle/S$[a] (%)	$\langle V\rangle/S$[b] (%)	$\langle\|V\|\rangle/S$[c] (%)	error[d] (%)
J0045−7319	660	0.7	11	−17	27	7
J1105−6107	1350	1.0	89	+9	12	2
J1316−6232	1350	1.8	–	–	–	–
	2264	0.6	–	–	–	–
J1341−6220	1350	2.3	56	−21	22	2
J1513−5908	660	2.6	97	−23	25	7
	1350	1.3	94	−18	18	2
J1627−4845	1350	0.5	–	–	–	–
J1646−4346	1350	0.8	45	+6	13	5
J1730−3350	1350	3.3	56	−5	7	1
J1801−2306	1350	6.2	14	+12	13	2
	2264	2.1	−2	+7	12	4

[a]Fractional linear polarization of on-pulse bins.

[b]Fractional circular polarization of on-pulse bins. Positive values are left-circularly polarized.

[c]Fractional absolute value of circular polarization of on-pulse bins.

[d]2σ uncertainty in measured polarization values. The uncertainty from instrumental effects is less than 5%.

Table B-4. Measured Pulse Widths and Rotation Measures

PSR	Freq (MHz)	W_{50}[a] (ms)	W_{10}[b] (ms)	RM (rad m^{-2})	$\langle B_{\|\|} \rangle$[c] (μG)
J0045−7319	660	20	220	−14 ± 27	−0.2 ± 0.3
J1105−6107	1350	4	10	+166 ± 3	+0.76 ± 0.01
J1316−6232	1350	119	180	–	–
	2264	81	115	–	–
J1341−6220	1350	10	45	−946 ± 7	−1.60 ± 0.01
J1513−5908	660	36	75	+211 ± 5	+1.02 ± 0.03
	1350	14	40	+215 ± 2	+1.046 ± 0.008
J1627−4845	1350	32	170	–	–
J1646−4346	1350	12	70	−65 ± 17	−0.16 ± 0.04
J1730−3350	1350	7	20	−142 ± 5	−0.68 ± 0.02
J1801−2306	1350	88	265	−1156 ± 19	−1.33 ± 0.02
	2264	19	80	–	–

[a]Width at which the measured pulse reaches 50% of its peak (FWHM), with uncertainty 1 ms.

[b]Width at which the measured pulse reaches 10% of its peak, with uncertainty 5 ms.

[c]Negative values correspond to the magnetic field pointing away from the observer.

Table B-5. Astrometric and Spin Parameters for PSR J1316−6232

Parameter	Value[a]
Right Ascension, α (J2000)	$13^h16^m46^s.3(2)$
Declination, δ (J2000)	$-62°32'12''.2(5)$
Galactic Latitude, l	$305°.85$
Galactic Longitude, b	$+0°.19$
Period, P (s)	0.34282539844(6)
Period Derivative, $\dot{P}$	$5.297(2) \times 10^{-15}$
Dispersion Measure, DM (pc cm^{-3})	983(2)
Epoch of Period (MJD)	49800.0

[a]Figures in parentheses represent 1σ uncertainties in the least-significant digit quoted.

Bibliography

Arons, J. 1992, in The Magnetospheric Structure and Emission Mechanisms of Radio Pulsars, IAU Colloquium 128, ed. T. H. Hankins, J. R. Rankin, & J. Gil, (Zielona Góra, Poland: Pedagogical University Press), 56

Arzoumanian, Z., Nice, D. J., Taylor, J. H., & Thorsett, S. E. 1994, ApJ, 422, 671

Azzopardi, M. 1987, A&AS, 69, 421

Baade, W. & Zwicky, F. 1934, Phys. Rev., 45, 138

Backer, D. C., Kulkarni, S. R., Heiles, C., Davis, M. M., & Goss, W. M. 1982, Nature, 300, 615

Becker, R. H., White, R. L., & Helfand, D. J. 1995, ApJ, 450, 559

Bhattacharya, D. 1990, J. Astrophys. Astr., 11, 125

Bietenholz, M. F., Kassim, N., Frail, D. A., Perley, R. A., Erickson, W. C., & Hajian, A. R. 1997, ApJ, 490, 291

Biggs, J. D. 1990, MNRAS, 245, 514

Blandford, R. D. & Romani, R. W. 1988, MNRAS, 234, 57P

Brazier, K. T. S. & Becker, W. 1997, MNRAS, 284, 335

Camilo, F. 1997, in High Sensitivity Radio Astronomy, ed. N. Jackson & R. J. Davis, Cambridge University Press, 14

Camilo, F. & Nice, D. J. 1995, ApJ, 445, 756

Camilo, F. M., Kaspi, V. M., Lyne, A. G., Manchester, R. N., Bell, J. F., D'Amico, N., McKay, N. P. F., & Crawford, F. 2000, ApJ. accepted (astro-ph/0004330)

Chakrabarty, D. & Morgan, E. H. 1998, Nature, 394, 346

Clark, B. G. 1989, in Synthesis Imaging In Radio Astronomy, ed. R. A. Perley, F. R. Schwab, & A. H. Bridle, (San Francisco: ASP Conference Series, Volume 6), 1

Clifton, T. R., Lyne, A. G., Jones, A. W., McKenna, J., & Ashworth, M. 1992, MNRAS, 254, 177

Cole, A. A. 1998, ApJ, 500, L137

Condon, J. J., Cotton, W. D., Greisen, E. W., Yin, Q. F., Perley, R. A., Taylor, G. B., & Broderick, J. J. 1998, AJ, 115, 1693

Condon, J. J., Griffith, M. R., & Wright, A. E. 1993, AJ, 106, 1095

Cordes, J. M., Weisberg, J. M., & Boriakoff, V. 1985, ApJ, 288, 221

Cornwell, T. J. & Evans, K. F. 1985, A&A, 143, 77

Crawford, F., Gaensler, B. M., Manchester, R. N., Kaspi, V. M., Camilo, F., Lyne, A. G., & Pivovaroff, M. J. 2000a, ApJ. in preparation

Crawford, F., Kaspi, V. M., & Bell, J. F. 2000, AJ, 119, 2376

Crawford, F., Kaspi, V. M., & Manchester, R. N. 2000, AJ. submitted

Crawford, F., Kaspi, V. M., Manchester, R. N., Camilo, F., Lyne, A. G., & D'Amico, N. 1998, Memorie della Societa' Astronomica Italiana, 69, 951

Crawford, F., Kaspi, V. M., Manchester, R. N., Lyne, A. G., Camilo, F., & D'Amico, N. 2000b, ApJ. in preparation

D'Amico, N. et al. 2000, ApJ. in preparation

D'Amico, N., Stappers, B. W., Bailes, M., Martin, C. E., Bell, J. F., Lyne, A. G., & Manchester, R. N. 1998, MNRAS, 297, 28

Dewey, R. J., Taylor, J. H., Weisberg, J. M., & Stokes, G. H. 1985, ApJ, 294, L25

Filipovic, M. D. et al. 1998, A&AS, 127, 119

Frail, D. A., Kulkarni, S. R., & Vasisht, G. 1993, Nature, 365, 136

Frail, D. A. & Scharringhausen, B. R. 1997, ApJ, 480, 364

Frater, R. H., Brooks, J. W., & Whiteoak, J. B. 1992, Journal of Electrical and Electronics Engineering Australia, 12, 103

Gaensler, B. M., Bock, D. C., & Stappers, B. W. 2000, ApJ, 537, L35

Gaensler, B. M., Brazier, K. T. S., Manchester, R. N., Johnston, S., & Green, A. J. 1999, MNRAS, 305, 724

Gaensler, B. M., Manchester, R. N., Staveley-Smith, L., Tzioumis, A. K., Reynolds, J. E., & Kesteven, M. J. 1997, ApJ, 479, 845

Gold, T. 1969, Nature, 221, 25

Goldreich, P. & Julian, W. H. 1969, ApJ, 157, 869

Gould, D. M. & Lyne, A. G. 1998, MNRAS, 301, 235

Gray, A. D., Landecker, T. L., Dewdney, P. E., Taylor, A. R., Willis, A. G., & Normandeau, M. 1999, ApJ, 514, 221

Green, A. J., Cram, L. E., Large, M. I., & Ye, T. 1999, ApJS, 122, 207

Green, D. A. 1998, A Catalogue of Galactic Supernova Remnants (1998 September Version), (Cambridge: Mullard Radio Astronomy Observatory)

Han, J. L. & Tian, W. W. 1999, A&AS, 136, 571

Hewish, A., Bell, S. J., Pilkington, J. D. H., Scott, P. F., & Collins, R. A. 1968, Nature, 217, 709

Horowitz, P. & Hill, W. 1989, The Art of Electronics, (Cambridge: Cambridge University Press)

Jackson, J. D. 1962, Classical Electrodynamics, (New York: Wiley)

Johnston, S., Lyne, A. G., Manchester, R. N., Kniffen, D. A., D'Amico, N., Lim, J., & Ashworth, M. 1992a, MNRAS, 255, 401

Johnston, S., Manchester, R. N., Lyne, A. G., Bailes, M., Kaspi, V. M., Qiao, G., & D'Amico, N. 1992b, ApJ, 387, L37

Johnston, S., Manchester, R. N., Lyne, A. G., Kaspi, V. M., & D'Amico, N. 1995, A&A, 293, 795

Johnston, S., Nicastro, L., & Koribalski, B. 1998, MNRAS, 297, 108

Kaspi, V. M. 1994. PhD thesis, Princeton University

Kaspi, V. M. 1998, in Neutron Stars and Pulsars: Thirty Years after the Discovery, ed. N. Shibazaki, N. Kawai, S. Shibata, & T. Kifune, (Tokyo: Universal Academy Press), 401

Kaspi, V. M., Bailes, M., Manchester, R. N., Stappers, B. W., Sandhu, J. S., Navarro, J., & D'Amico, N. 1997, ApJ, 485, 820

Kaspi, V. M., Crawford, F., Manchester, R. N., Lyne, A. G., Camilo, F., D'Amico, N., & Gaensler, B. M. 1998, ApJ, 503, L161

Kaspi, V. M., Johnston, S., Bell, J. F., Manchester, R. N., Bailes, M., Bessell, M.,

Lyne, A. G., & D'Amico, N. 1994a, ApJ, 423, L43

Kaspi, V. M., Lyne, A. G., Manchester, R. N., Johnston, S., D'Amico, N., & Shemar, S. L. 1993, ApJ, 409, L57

Kaspi, V. M., Manchester, R. N., Johnston, S., Lyne, A. G., & D'Amico, N. 1992, ApJ, 399, L155

Kaspi, V. M., Manchester, R. N., Johnston, S., Lyne, A. G., & D'Amico, N. 1996, AJ, 111, 2028

Kaspi, V. M., Manchester, R. N., Siegman, B., Johnston, S., & Lyne, A. G. 1994b, ApJ, 422, L83

Kaspi, V. M., Tauris, T., & Manchester, R. N. 1996, ApJ, 459, 717

Katz-Stone, D. M. & Rudnick, L. 1997, ApJ, 488, 146

Kulkarni, S. R. 1992, Phil. Trans. Roy. Soc. A, 341, 77

Large, M. I., Vaughan, A. E., & Mills, B. Y. 1968, Nature, 220, 340

Lequeux, J. 1984, in Structure and Evolution of the Magellanic Clouds, IAU Symposium 108, ed. S. van den Bergh & K. S. de Boer, (Dordrecht, Holland: Reidel), 67

Lorimer, D. R., Bailes, M., Dewey, R. J., & Harrison, P. A. 1993, MNRAS, 263, 403

Lorimer, D. R., Yates, J. A., Lyne, A. G., & Gould, D. M. 1995, MNRAS, 273, 411

Lyne, A. G. et al. 2000, MNRAS, 312, 698

Lyne, A. G. & Manchester, R. N. 1988, MNRAS, 234, 477

Lyne, A. G. et al. 1998, MNRAS, 295, 743

Lyne, A. G., Manchester, R. N., & Taylor, J. H. 1985, MNRAS, 213, 613

Lyne, A. G., Pritchard, R. S., & Smith, F. G. 1993, MNRAS, 265, 1003

Lyne, A. G., Ritchings, R. T., & Smith, F. G. 1975, MNRAS, 171, 579

Manchester, R. N. 1996, in Pulsars: Problems and Progress, IAU Colloquium 160, ed. S. Johnston, M. A. Walker, & M. Bailes, (San Francisco: Astronomical Society of the Pacific), 193

Manchester, R. N., D'Amico, N., & Tuohy, I. R. 1985, MNRAS, 212, 975

Manchester, R. N., Han, J. L., & Qiao, G. J. 1998, MNRAS, 295, 280

Manchester, R. N., Kaspi, V. M., Johnston, S., Lyne, A. G., & D'Amico, N. 1991,

MNRAS, 253, 7P

Manchester, R. N. et al. 2000, MNRAS. in preparation

Manchester, R. N. et al. 1996, MNRAS, 279, 1235

Manchester, R. N., Mar, D., Lyne, A. G., Kaspi, V. M., & Johnston, S. 1993, ApJ, 403, L29

Manchester, R. N., Staveley-Smith, L., & Kesteven, M. J. 1993, ApJ, 411, 756

Manchester, R. N., Tademaru, E., Taylor, J. H., & Huguenin, G. R. 1973, ApJ, 185, 951

Manchester, R. N. & Taylor, J. H. 1977, Pulsars, (San Francisco: Freeman)

Manchester, R. N., Tuohy, I. R., & D'Amico, N. 1982, ApJ, 262, L31

Marshall, F. E., Gotthelf, E. V., Zhang, W., Middleditch, J., & Wang, Q. D. 1998, ApJ, 499, L179

Mathewson, D. S. 1985, Proc. Astr. Soc. Aust., 6, 104

McConnell, D., McCulloch, P. M., Hamilton, P. A., Ables, J. G., Hall, P. J., Jacka, C. E., & Hunt, A. J. 1991, MNRAS, 249, 654

McLaughlin, M. A., Cordes, J. M., Hankins, T. H., & Moffett, D. A. 1999, ApJ, 512, 929

Melatos, A. 1997, MNRAS, 288, 1049

Meyssonnier, N. & Azzopardi, M. 1993, A&AS, 102, 451

Narayan, R. & Nityananda, R. 1986, Ann. Rev. Astr. Ap., 24, 127

Navarro, J. 1994. PhD thesis, California Institute of Technology

Navarro, J., Manchester, R. N., Sandhu, J. S., Kulkarni, S. R., & Bailes, M. 1997, ApJ, 486, 1019

Nice, D. J., Fruchter, A. S., & Taylor, J. H. 1995, ApJ, 449, 156

Olszewski, E. W., Suntzeff, N. B., & Mateo, M. 1996, Ann. Rev. Astr. Ap., 34, 511

Pacini, F. 1967, Nature, 216, 567

Pacini, F. & Salvati, M. 1973, ApJ, 186, 249

Pivovaroff, M. J. 2000. PhD thesis, Massachusetts Institute of Technology

Pivovaroff, M. J., Kaspi, V. M., Gaensler, B. M., Crawford, F., & Camilo, F. 2000, ApJ. in preparation

Possenti, A., Colpi, M., D'Amico, N., & Burderi, L. 1998, ApJ, 497, L97

Press, W. H., Teukolsky, S. A., Vetterling, W. T., & Flannery, B. P. 1992, Numerical Recipes: The Art of Scientific Computing, 2^{nd} edition, (Cambridge: Cambridge University Press)

Qiao, G. J., Manchester, R. N., Lyne, A. G., & Gould, D. M. 1995, MNRAS, 274, 572

Radhakrishnan, V. & Cooke, D. J. 1969, Astrophys. Lett., 3, 225

Reynolds, S. P. & Chevalier, R. A. 1984, ApJ, 278, 630

Richards, D. W. & Comella, J. M. 1969, Nature, 222, 551

Roberts, M. S. E. & Romani, R. W. 1998, ApJ, 496, 827

Roberts, M. S. E., Romani, R. W., Johnston, S., & Green, A. J. 1999, ApJ, 515, 712

Romani, R. W. & Yadigaroglu, I.-A. 1995, ApJ, 438, 314

Sault, R. J. & Killeen, N. E. B. 1998, The Miriad User's Guide, (Sydney: Australia Telescope National Facility)

Scheuer, P. A. G. 1968, Nature, 218, 920

Seward, F. D. & Harnden, F. R. 1982, ApJ, 256, L45

Seward, F. D., Harnden, F. R., & Helfand, D. J. 1984, ApJ, 287, L19

Spitzer, L. 1978, Physical Processes in the Interstellar Medium, (New York: Wiley-Interscience)

Staelin, D. H. & Reifenstein, E. C. 1968, Science, 162, 1481

Standish, E. M. 1990, A&A, 233, 252

Stappers, B. W., Gaensler, B. M., & Johnston, S. 1999, MNRAS, 308, 609

Staveley-Smith, L. et al. 1996, Proc. Astr. Soc. Aust., 13, 243

Tammann, G. A., Löffler, W., & Schröder, A. 1994, ApJS, 92, 487

Taylor, J. H. 1974, A&AS, 15, 367

Taylor, J. H. & Cordes, J. M. 1993, ApJ, 411, 674

Taylor, J. H., Manchester, R. N., & Lyne, A. G. 1993, ApJS, 88, 529

Thompson, A. R., Moran, J. M., & Swenson, G. W. 1986, Interferometry and Synthesis in Radio Astronomy, (New York: John Wiley and Sons)

Torii, K., Gotthelf, E. V., Vasisht, G., Dotani, T., & Kinugasa, K. 2000, ApJ, 534,

L71

Trimble, V. 1968, AJ, 73, 535

Turatto, M. 2000, in The Chemical Evolution of The Milky Way: Stars versus Clusters, ed. F. Matteucci & F. Giovannelli, (astro-ph/0001457)

van Buren, D. & Greenhouse, M. A. 1994, ApJ, 431, 640

Vangioni-Flam, E., Lequeux, J., Maucherat-Joubert, M., & Rocca-Volmerange, B. 1980, A&A, 90, 73

von Hoensbroech, A., Kijak, J., & Krawczyk, A. 1998, A&A, 334, 571

Wang, N., Manchester, R. N., Pace, R., Bailes, M., Kaspi, V. M., Stappers, B. W., & Lyne, A. G. 2000, MNRAS. accepted (astro-ph/0005561)

Wang, Q. & Wu, X. 1992, ApJS, 78, 391

Weiler, K. W. & Panagia, N. 1980, A&A, 90, 269

White, R. L., Becker, R. H., Helfand, D. J., & Gregg, M. D. 1997, ApJ, 475, 479

Wu, X., Manchester, R. N., Lyne, A. G., & Qiao, G. 1993, MNRAS, 261, 630

Ye, T. & Turtle, A. J. 1993, in New Aspects of Magellanic Cloud Research, 167

Young, M. D., Manchester, R. N., & Johnston, S. 1999, Nature, 400, 848

Zaritsky, D., Harris, J., Grebel, E. K., & Thompson, I. B. 2000, ApJ, 534, L53